# The Engine Reformer: Syngas Production in Engines Using Spark-Ignition and Metallic Foam Catalysts

by

Emmanuel G. Lim

B.S., Mechanical Engineering
Duke University, 2013

Submitted to the Department of Mechanical Engineering in Partial Fulfillment of the Requirements for the Degree of

Master of Science in Mechanical Engineering

at the

Massachusetts Institute of Technology

June 2015

Signature of Author: Signature redacted
Department of Mechanical Engineering
May 8, 2015

Certified by: Signature redacted
Wai K. Cheng
Professor of Mechanical Engineering
Thesis Supervisor

Accepted by: Signature redacted
David E. Hardt
Professor of Mechanical Engineering
Graduate Officer

# The Engine Reformer: Syngas Production in Engines Using Spark-Ignition and Metallic Foam Catalysts

by

Emmanuel G. Lim

Submitted to the Department of Mechanical Engineering
on May 8, 2015 in partial fulfillment of the
Requirements for the Degree of Master of Science in
Mechanical Engineering

## Abstract

An experimental study was performed to assess the feasibility of performing methane ($CH_4$) partial oxidation (POX) in two internal combustion engines: one equipped to perform spark-ignition (the "spark-ignited engine"), and the other containing a catalyst in the engine cylinder (the "catalytic engine"). The exhaust gases were rich in hydrogen- ($H_2$) and carbon monoxide- (CO), and could be used as synthesis gas ("syngas") for the synthesis of liquid fuels such as methanol. Conventional syngas production techniques are only economical on a large scale and cannot be transported to hard-to-reach gas sources, where gas-to-liquids (GTL) would have the biggest impact on the transportability of that gas. Engines could be deployed at these locations to produce syngas on a small scale and at low cost, as they benefit from the economies of mass production that have been achieved through advanced manufacturing techniques. We call this type of engine an "engine reformer".

This thesis contrasts the results of performing methane POX in two different engine reformers, using atmospheric air as the oxidizer. One of four cylinders in a Yanmar 4TNV84T marine diesel generator was converted to ignite methane POX mixtures using a spark plug. Intake temperatures > 350 °C were required to minimize misfire. Exhaust $H_2$ to CO ratios of 1.4 were achieved with methane-air equivalence ratios ($\phi_M$) up to 2.0, while ratios of > 2.0 were achieved with hydrocarbon-air equivalence ratios ($\phi_{HC}$) up to 2.8 with the assistance of hydrogen ($H_2$) and ethane ($C_2H_6$). High equivalence ratios $\phi_{HC} > 2.2$ showed reduced $CH_4$ conversion efficiency, therefore $\phi_{HC} = 2.2$ (with $H_2$) produced a good tradeoff between syngas quality and $CH_4$ conversion. A single-cylinder Lister-Petter TR1 diesel generator was used to perform methane POX using a palladium (Pd) washcoat catalyst deposited on a Fecralloy® disk. With > 150 °C intake temperatures, exhaust $H_2$ to CO ratios of 1.0 were achieved with methane-air equivalence ratios $\phi_M = 4.0$ with varying amounts of $CO_2$ to simultaneously perform methane dry reforming. Spark-ignition appeared to provide higher reliability, though tests will continue to be performed on the catalytic engine to optimize performance. A larger engine of a similar design to the spark-ignited Yanmar will be deployed at a demonstration plant in North Carolina to produce syngas at higher flow rates, and will be integrated with a liquids synthesis reactor to produce methanol.

Thesis Supervisor: Wai K. Cheng
Title: Professor of Mechanical Engineering; Director, Sloan Automotive Laboratory

## Acknowledgements

I would like to recognize the following individuals who were critical to this process. I feel privileged to have had the opportunity to work with you:

- Dr. Leslie Bromberg, Professor Wai K. Cheng, Professor William H. Green, Dr. Daniel Cohn, and Dr. Kevin D. Cedrone, who provided invaluable guidance and moral support, and led the effort in converting our ideas to reality.
- Dr. Alex Sappok and Filter Sensing Technologies Inc. for helping us design assemble the catalytic engine. This would have been impossible without your help.
- Angi Acocella, Andrea Aarce, Enoch Dames, Thomas Needham, Raul Barraza, and Luis Mora, who were the most supportive collaborators.
- Thane DeWitt and Raymond Phan, who made building things possible.
- Kyle Merical and Dr. Paul Yelvington from Mainstream Engineering, whose automotive expertise were invaluable to my education.
- Dr. John Carpenter at the Research Triangle Institute, who led the fight in making this demonstration project a reality.
- Josh Browne at Columbia University and Professor Klaus Lackner at Arizona State University, who provided thoughtful guidance.

I would especially like to thank my parents and family for their support during this time.

I would also like to thank ARPA-e, the MIT Energy Initiative, and the Tata Center for Technology and Design at MIT for their generous financial support.

## Table of Contents

## List of Figures

## List of Tables

## Nomenclature

| | |
|---|---|
| A | Amps |
| BCF | Billion cubic feet |
| BDC | Bottom-dead-center |
| boe/d | Barrels of oil equivalent per day |
| CAD | Crank angle degree (°), also Computer-aided design |
| CAM | Computer-aided manufacturing |
| $C_{Bal}$ | Carbon balance; ratio of moles of $C$ in dry exhaust to moles of $C$ in intake |
| $CH_4$ | Methane |
| CI | Compression-ignition |
| CNC | Computer numerical control |
| CNG | Compressed natural gas |
| CO | Carbon monoxide |
| $CO_2$ | Carbon dioxide |
| $COV_{NIMEP}$ | Coefficient of variation of net indicated mean effective pressure (%) |
| $c_s$ | Soot concentration in exhaust gas (mg/L) |
| DC | Direct current |
| EOR | Enhanced oil recovery |
| GTL | Gas-to-liquids |
| GTS | Gas-to-solids |
| $\Delta H_{298}^{\circ}$ | Reaction enthalpy at 298 K |
| $H_2$ | Hydrogen |
| Hz | Hertz |
| Ir | Iridium |
| $\lambda$ | Air-fuel equivalence ratio |
| LNG | Liquefied natural gas |
| MAP | Manifold absolute pressure |
| $\dot{m}_{engine}$ | Mass flow rate at engine intake (g/min) |
| MFC | Mass flow controller |
| $M_{mix}$ | Molar mass of intake mixture (g/mol) |
| $m_{s,f}$ | Mass of soot filter paper after soot loading |
| $m_{s,i}$ | Mass of soot filter paper before soot loading |
| MSCF | Thousand standard cubic feet |
| MSCFD | Thousand standard cubic feet per day |
| MMSCF | Million standard cubic feet |
| MMSCFD | Million standard cubic feed per day |
| MMSCMD | Million standard cubic meters per day |
| MS5A | CP-Molsieve 5A |
| MT | Metric ton |
| $N$ | Engine speed (rev/min) |
| $N_2$ | Nitrogen |
| NGL | Natural gas liquid |
| Ni | Nickel |
| $NIMEP_{mean}$ | Average net indicated mean effective pressure (kPa) |

| | |
|---|---|
| $NO_x$ | Nitrogen oxides |
| NURBS | Non-uniform rational B-spline |
| $O_2$ | Oxygen |
| $p$ | Pressure |
| $p_{cyl,pk}$ | Average peak cylinder pressure (bar) |
| Pd | Palladium |
| $p_{exh}$ | Exhaust manifold pressure |
| $\phi$ | Fuel-air equivalence ratio |
| $\phi_{HC}$ | Total hydrocarbon-air equivalence ratio |
| $\phi_M$ | Total hydrocarbon-air equivalence ratio, where the total number of moles of fuel is the same as if only $CH_4$ were present in the fuel |
| $p_i$ | Intake manifold pressure |
| POX | Partial oxidation |
| PPU | PoraPLOT U |
| PSA | Pressure swing adsorption |
| PSIA | Pounds per square inch, absolute |
| PSIG | Pounds per square inch, gauge |
| Pt | Platinum |
| $R$ | Universal gas constant $\left(\frac{L\ kPa}{K\ mol}\right)$ |
| $r_c$ | Compression ratio |
| Rh | Rhodium |
| Ru | Ruthenium |
| SCFD | Standard cubic feet per day |
| SCFH | Standard cubic feet per hour |
| SCMD | Standard cubic meters per day |
| SI | Spark-ignition |
| SPDT | Single-pole double-throw |
| $T$ | Temperature |
| TCF | Trillion cubic feet |
| $T_i$ | Intake mixture temperature (°C); when used in $\dot{m}_{engine}$ this is in (K) |
| tpd | Tons per day |
| VAC | Volts, alternating current |
| $\dot{V}^{\circ}_{CH_4}$ | Intake volumetric flow rate of $CH_4$ at 25 °C, 1 atm (standard) conditions |
| $V_d$ | Engine displacement volume (L) |
| VDC | Volts, direct current |
| VFD | Variable frequency drive |
| $\dot{V}_{sample}$ | Volumetric flow rate of exhaust gas through filter paper (using viscosity of air) |
| $\Delta t_{sample}$ | Total soot sampling time |
| $x_{C_2H_6}$ | Mole fraction of $C_2H_6$ in hydrocarbon ($C_2H_6$ and $CH_4$) fuel |
| $X_{C_2H_6}$ | Conversion efficiency of $C_2H_6$ |
| $X_{CH_4}$ | Conversion efficiency of $CH_4$ |
| $x_{H_2}$ | Mole fraction of $H_2$ in intake mixture |
| $x_{i,exh}$ | Mole fraction of compound $i$ in dry exhaust |
| $x_{i,in}$ | Mole fraction of compound $i$ in intake mixture |

# 1. Introduction & Background

The internal combustion engine was originally designed and built to convert chemical energy in a fuel to mechanical work. As such, its conventional purpose is to serve as a portable power plant to generate shaft work to move objects, or generate electricity. However, this thesis aims to demonstrate that the engine can also be operated as a chemical reactor, in order to produce synthesis gas ("syngas") at remote locations for use in liquid fuels synthesis.

## 1.1. Combustion Chemistry in Internal Combustion Engines

The internal combustion engine operates on the principal of extracting work from the complete oxidation of a fuel such as gasoline, diesel, or natural gas. Complete oxidation leads to the breaking of the C-C (for fuel molecules with multiple carbons atoms) and C-H bonds in the fuel molecules, and the production of $CO_2$ and $H_2O$. For example, the complete ("stoichiometric") combustion of methane ($CH_4$) with pure oxygen (the oxidant) follows the relationship shown in Eq. 1.

$$CH_4 + 2O_2 \rightarrow CO_2 + 2H_2O \qquad (1)$$

The heating value of a fuel refers to the energy released during this chemical reaction. The lower heating value (LHV) does not include the additional energy extracted from the condensation of exhaust water vapor, while the higher heating value (HHV) does. For $CH_4$, the LHV and HHV are 50.0 MJ/kg of $CH_4$ and 55.5 MJ/kg of $CH_4$ respectively [1].

The relative quantity of fuel to oxidant can affect the exhaust products of combustion significantly. When the mass ratio of fuel to oxidant is less than that required for stoichiometric combustion, the mixture is said to be "lean" in fuel. On the other hand, when this ratio is greater than that required for stoichiometric combustion, the mixture is said to be "rich" in fuel. The oxidant may have any concentration of oxygen, as nitrogen does not participate as shown in the chemical equation. In reality, oxides of nitrogen

($NO_x$) may be produced due to the high temperatures achieved in the cylinder, though they are not considered in this work as no $NO_x$ products were found in the exhaust gas measurements. Furthermore, in theoretical calculations, air will be assumed to contain 20.95% $O_2$ and 79.05% "apparent" $N_2$ (which includes Argon and Carbon Dioxide), and therefore has a molar mass of 28.96 g/mol [1]. In calculations using air, for every 1 mole of $O_2$, there will be 79.05 / 21.95 = 3.773 moles of $N_2$.

The fuel-air ratio by mass ($F/A$) is the ratio of the mass of fuel to the mass of air in a given mixture of combustible gas. For example, the stoichiometric combustion of $CH_4$ in atmospheric air has the fuel-air ratio shown in Eq. 2., where $M_{CH_4} = 16.04$ g/mol and $M_{air} = 28.96$ g/mol. The fuel-air equivalence ratio ($\phi$), shown in Eq. 3, is a convenient way to quantify fuel leanness and richness, and is the ratio of the fuel-air ratio in a given mixture $(F/A)_{mix}$, to the fuel-air ratio in stoichiometric mixtures $(F/A)_{stoich}$ [1].

$$(F/A)_{CH_4,stoich} = \frac{(1\,mol)M_{CH_4}}{(2 \cdot 4.773\,mol)M_{air}} = 17.2 \qquad (2)$$

$$\phi = \frac{(F/A)_{mix}}{(F/A)_{stoich}} \qquad (3)$$

In stoichiometric mixtures, $\phi = 1$. In lean mixtures, $\phi < 1$, while in rich mixtures, $\phi < 1$. Lean mixtures contain excess $O_2$ for the complete combustion of $CH_4$. Therefore, the analytical products of combustion will contain $CO_2$, $H_2O$, $O_2$ and $N_2$ only. The degree of leanness will dictate the amount of $O_2$ leftover in the products. So long as combustion proceeds to completion, the analytical product composition is straightforward to calculate. In Eq. 4, the fuel-lean combustion of $CH_4$ is expressed with respect to the air-fuel equivalence ratio $\lambda = \frac{1}{\phi}$.

$$CH_4 + 2\lambda(O_2 + 3.773N_2) \rightarrow CO_2 + 2H_2O + 2(\lambda - 1)O_2 + 7.546\lambda\, N_2 \qquad (4)$$

On the other hand, rich mixtures are $O_2$-starved. Therefore, the analytical products of combustion will contain a spectrum of the following species: CO, $CO_2$, $H_2$, $H_2O$, and $N_2$. The concentration of the product gas must be calculated using equilibrium chemistry to determine the relative distribution of the variables $a$, $b$, $c$ and $d$ based on the temperature at which the reaction stops, or "freezes". The fuel-rich combustion stoichiometry of $CH_4$ is shown in Eq. 5.

$$CH_4 + \frac{2}{\phi}(O_2 + 3.773N_2) \rightarrow aCO_2 + bCO + cH_2O + dH_2 + \frac{7.546}{\phi}N_2 \qquad (5)$$

## 1.2. Methane Reforming

Synthesis gas (syngas) is a mixture of hydrogen and carbon monoxide, and may also contain carbon dioxide, and water vapor[1]. It is produced from the oxidation of a carbon source such as methane, by reacting with steam, oxygen or carbon dioxide [2], and is a critical component in the synthesis of complex liquid products such as ammonia, methanol and the long-chain hydrocarbons found in synthetic crude oil. A simple way to conceptualize this process is to consider it in two steps:

1) *Reformation*: breakdown of a hydrocarbon into $H_2$ and CO through oxidation with steam, oxygen, or carbon dioxide. $H_2$ and CO are critical components for synthesis. In practice, however, the products of complete oxidation (namely $H_2O$ and $CO_2$) may also be produced, though in small quantities if reactant compositions are tuned properly.

2) *Synthesis*: stitching $H_2$ and CO into long chain products, typically performed with the help of a catalyst. Depending on the syngas composition, catalyst type/morphology, and thermodynamic conditions, the resulting product may be ammonia, methanol, dimethyl ether (DME), or Fischer-Tropsch liquids (synthetic crude oil), among other things [2].

---

[1] Syngas may contain Nitrogen when used for the synthesis of Ammonia

In practice, syngas may be produced from hydrocarbons other than methane, such as crude oil products. However, the ultimate goal is to perform chemical conversion from the gaseous state (which tends to be more expensive to handle for transportation) to the liquid state, as liquid fuels are easier to transport and can be consumed in distributed infrastructure such as engines. Since methane is readily available from natural gas, the reformation process is a key step in unlocking hard-to-reach natural gas sources by converting them to liquid fuels.

There are three fundamental methods to produce syngas from methane:

1) *Steam Reforming*: Methane and steam are reacted in equal parts by mole to form a product gas with a stoichiometric $H_2$ to CO ratio of 3 (Eq. 6). The reaction is strongly endothermic, with a standard reaction enthalpy $\Delta H^0_{298} = 206$ kJ/mol.

$$CH_4 + H_2O \leftrightarrow CO + 3H_2 \qquad \Delta H^0_{298} = 206 \text{ kJ/mol} \tag{6}$$

2) *Partial Oxidation*: Methane and oxygen are reacted using two moles of methane for every mole of oxygen to form a product gas with a stoichiometric $H_2$ to CO ratio of 2 (Eq. 7). This is akin to operating a conventional methane-burning engine with a fuel-air equivalence ratio $\phi = 4$. The reaction is slightly exothermic, with a standard reaction enthalpy of $\Delta H^0_{298} = -36$ kJ/mol.

$$CH_4 + 0.5O_2 \leftrightarrow CO + 2H_2 \qquad \Delta H^0_{298} = -36 \text{ kJ/mol} \tag{7}$$

3) *$CO_2$ Reforming*: Also called “dry reforming”, methane and carbon dioxide are reacted in equal parts to form a product gas with equal parts $H_2$ and CO (Eq. 8). The reaction is also strongly endothermic, with a standard reaction enthalpy of $\Delta H^0_{298} = 247$ kJ/mol.

$$CH_4 + CO_2 \leftrightarrow 2CO + 2H_2 \qquad \Delta H^0_{298} = 247 \text{ kJ/mol} \tag{8}$$

Reaction equilibria are also controlled by the water-gas shift (WGS) reaction shown in Eq. 9.

$$CO + H_2O \leftrightarrow CO_2 + H_2 \qquad \Delta H^0_{298} = -41 \text{ kJ/mol} \tag{9}$$

In the production of $H_2$, steam is added to reforming products to promote the production of $H_2$ by driving the water-gas shift reaction in favor of the right-hand side in Eq. 9. Furthermore, carbon-formation can occur during reformation and can lead to soot buildup on catalyst active sites and affect other process equipment downstream. In steam reforming, higher $H_2O/C$ (S/C) ratios can promote the conversion efficiency of methane, and therefore reduce the tendency for carbon formation. The carbon forming reactions can take the three general forms shown in Eqs. 10-12 [2]:

$$CH_4 \leftrightarrow C + 2H_2 \qquad \Delta H^0_{298} = 75 \text{ kJ/mol} \tag{10}$$

$$2CO \leftrightarrow C + CO_2 \qquad \Delta H^0_{298} = -172 \text{ kJ/mol} \tag{11}$$

$$CO + H_2 \leftrightarrow C + H_2O \qquad \Delta H^0_{298} = -131 \text{ kJ/mol} \tag{12}$$

Steam and dry reforming are highly endothermic, and therefore require significant heating to achieve reasonable conversion. Steam reforming achieves higher conversion rates at higher temperatures and lower pressures [3], though higher pressures tend to be favored for financial reasons in order to achieve a reasonable throughput. In practice, the stoichiometric reactant compositions shown above are insufficient to achieve practical conversion efficiencies in industry. Therefore, higher $H_2O/CH_4$ ratios > 1 are used to compensate when steam and dry reforming are used together. These higher $H_2O/CH_4$ ratios must be balanced by cost restrictions, since equipment capital costs can become unreasonable above certain steam requirements [2].

All three reforming methods may be combined in a process called autothermal reforming. This allows a processing plant to adjust the $H_2$ to CO ratio to a desired value based on the synthesis process being used downstream of the syngas plant, since different synthesis processes require different ratios [3]. Autothermal reforming allows a unit to be flexible. However, in the remote locations where stranded gas sites are typically located, the availability of reformation feedstocks such as water for steam reforming, $CO_2$ for dry reforming, and fuel to generate heat to drive endothermic reactions may be hard to come by. Therefore, partial oxidation tends to be favored in these extreme applications due to its exothermicity, which would avoid heat input to drive the reaction, and the relative ease of drawing air from the atmosphere. Generally speaking, when considering the various chemistries discussed so far, it is important to balance the thermodynamic and chemical effects of each of the reformation methods in order to reach a reasonable total reaction enthalpy (and therefore energy input and cooling requirements), product $H_2$ to CO ratio, and methane conversion efficiency.

In synthesizing liquid fuels from gaseous fuels, methane reforming can be bypassed entirely by using catalysts that can perform the conversion directly. This will be discussed in a later section. However, the focus of this work is on using the syngas route, as it has been shown to achieve higher carbon efficiencies by dividing the synthesis process into two separate steps [2]. A disadvantage of generating syngas to produce liquid fuels is the loss of energy through the exchange of heat, e.g. through an engine, which contributes to some amount of chemical conversion inefficiency.

### 1.2.1. Partial Oxidation (POX)

The focus of this work was to produce syngas by partially oxidizing methane in an engine. This takes advantage of the low capital cost of internal combustion engines, as well as the low heating requirements of partial oxidation due to its mild exothermicity. The two routes to partial oxidation that are studied here are with and without catalysis.

#### *1.2.1.1. Catalytic Methods*

Catalytic routes for the partial oxidation of methane involve transition metal or noble metal catalysts. Experiments have been performed at 1 atm and 673-1273 K with $CH_4$

and pure $O_2$ or air using Ni and/or Co transition metals, and Ir, Pt, Pd, Ru, Rh noble metal catalysts [4]. Production of syngas over platinum and rhodium surfaces [5] was achieved with greater than 90% selectivity for both $H_2$ and CO within millisecond residence times. Rhodium was found to be superior to platinum in its selectivity to $H_2$ over $H_2O$. The partial oxidation of methane over palladium catalysts was found to proceed in a sequential combustion-then-reforming mechanism [6]. $CO_2$ partial pressures peaked in the temperature range between 575 and 875 K, and high CO selectivity was only possible above this range. Due to combustion occurring in this reaction mechanism, a high adiabatic temperature rise must be taken into account for Pd catalysts performing methane POX.

In the catalytic engine tested in this work, a crankshaft speed of 563 rpm was held constant. This corresponds to 4.7 Hz. Therefore, the combustion gases were drawn into the engine every 210 ms, and spent half of the cycle (105 ms) inside the cylinder, as the test engine for catalytic POX was four-stroke. The duration of combustion is on the order of 10 CAD in typical spark-ignited (~ 45 CAD) and compression-ignition (~ 30 CAD) engines, which corresponds to 3 ms at this engine speed. This is a reasonable value to compare with as this is when the cylinder temperatures and pressures will be the highest during the engine cycle, and therefore is when the chemistry will proceed most quickly. Therefore, the millisecond residence time requirement described above for catalytic POX was fulfilled.

Lower temperatures and pressures necessary to achieve high conversion rates are a major draw for the catalytic route, though questions still remain about catalyst stability and lifetime. The economics of catalytic technologies are also bound by the high capital investment required by conventional chemical reactor technologies to operate on a small scale, as well as the operating costs associated with regenerating or replenishing catalyst supplies. An engine performing partial oxidation may not be constrained in the same way [7].

#### *1.2.1.2. Non-Catalytic Partial Oxidation*

Non-catalytic partial oxidation of natural gas is a well-studied technology for the large-scale production of syngas, typically for the ammonia industry. Technologies based on the Shell and Texaco Gasification processes operate in excess of 1000 °C and 35 bar [8]. The Shell Gasification Process is a continuous fuel-rich flame process that was developed in the 1950s as a way to increase flexibility in the chemicals industry, as it allowed syngas production from any hydrocarbon source [9]. This, in turn, led to a significant increase in ammonia production. High temperatures were required to achieve high conversion efficiencies of methane and reduce the formation of soot [2]. Lower temperatures would have provided sub-optimal conditions for the oxidation of carbon and therefore would have led to higher soot production, even though the threshold for the POX reaction may have been satisfied. In the Shell process, any residual carbon was removed by water wash in order to prevent clogging of active sites on downstream water-gas shift catalysts used to boost the fraction of $H_2$ in the product gas.

Chemical plants based on these technologies require high throughputs to be economical and may only be applied where gas is available in large quantities. However, since the same conditions are possible in the engine cylinder, the same chemistry may be performed on a much smaller scale. Furthermore, depending on the size of the engine cylinder and the total number of cylinders, the total gas processing flow rate can be tailored to match the gas source.

### 1.2.2. Dry Reforming

As was described previously, dry reforming is the endothermic reaction of $CH_4$ and $CO_2$ to produce equal parts $H_2$ and CO. Replacing steam with $CO_2$ in the autothermal reforming reaction results in lower reaction rates due to reaction kinetics, but this was shown to not have any practical impact on reactor operation [10]. Dry reforming was performed in the catalytic engine in order to take advantage of this reaction's endothermicity. This was done out of caution of producing excessive temperatures in the cylinder that would damage the catalytic active sites. The intended purpose of the catalyst was to perform POX, however Pd was found to be an acceptable dry reforming catalyst as well. Rh was shown to be the best overall catalyst for dry reforming [11], while Ru showed high selectivity for carbon-free operation due to low carbon growth rates, and high activity for reforming [10]. Ni-, Ru-, Pd-, Ir- and Pt-based catalysts were also shown to perform well [10].

## 1.3. Stranded Gas

Many sources of natural gas at discovered conventional oil or gas fields are not being produced for either economic or technical reasons. These sources of natural gas are called "stranded gas" [12,13]. A viable solution to unlock these gas sources must address the economic as well as technical challenges of this problem. While the focus in this work was to demonstrate a technical solution to this problem, the economics will be addressed in future work during scale-up of the technology in a demonstration plant in the United States.

The estimated volume of recoverable stranded gas outside of North America according to the USGS was > 2600 TCF in 2008 [12], including both onshore and offshore resources. This is a significant quantity of gas. In many cases, the gas is left undisturbed as the economic investment required to extract it is simply too high. When natural gas occurs with oil, it is called "associated gas". This gas can benefit from the infrastructure that may be constructed to transport this oil, although a problem arises when the gas that is produced is too small in volume, making it too expensive to transport in its original state. Constructing gas pipelines is only economical at large scale. Therefore, this gas is stranded, associated gas. Oftentimes, this gas is burned on site for convenience, as that is the cheapest method of handling it. This process is called "flaring". The alternatives to flaring include injecting the gas back into the ground for enhanced oil recovery (EOR), but the compression requirements for this also require high capital investment. Also, the gas could be used on-site for electricity generation, but typically the amount that is produced is significantly larger than what could be used to power auxiliary equipment. Regardless of the type of stranded gas being considered, whether associated or not, the key issue here is the cost of transporting the gas to market. If some form of conversion were possible with favorable economics, this vast untapped resource could be extracted and utilized.

There are several options for transporting stranded gas sources to the marketplace. This includes building a pipeline, liquefaction (LNG), compression (CNG), conversion to solid ("gas-to-solids", GTS), conversion to electricity ("gas-to-work", GTW), and conversion to liquid fuels ("gas-to-liquids", GTL) [13]. The GTL process has been a popular topic in both academia and industry, and is the method being considered in this work. Performing an intermediate step by producing synthesis gas (or "syngas", which is ideally comprised of $H_2$ and CO only, although there are invariably other compounds such as $CO_2$) from natural gas, before catalytically converting that syngas to the desired liquid fuel, is an attractive route due to this method's high carbon efficiencies. The type of liquid fuel that can be synthesized from natural gas depends on the ratio of $H_2$ to CO in the syngas being used. The resulting product can range from ammonia and synthetic crude oil, to methanol. These liquid fuels benefit from low transportation costs compared to their gaseous counterparts as they have very low compressibility, and require mild to no compression to maintain their liquid state. Furthermore, they have a wide application throughout the chemicals, energy, and transportation sectors. Hence, there is a wide economic opportunity for the liquid products that can be produced from the GTL process.

According to the U.S. Energy Information Administration, the proved reserves of natural gas in the world in 2008 was 6,214 TCF. This number was almost 7,000 TCF by 2014 due to aggressive exploration in the United States, Middle East and Africa [14]. The most recent and comprehensive stranded gas field data were collected and complied by IHS International [15]. This data was up to the end of 2008. The size of the stranded gas reserves estimated outside of North America was found to be 2,612 TCF of gas in gas fields, and 966 TCF of gas in oil fields. In contrast to the proved reserve estimate in that year, this quantity is significant. Russia was the single largest holder of stranded gas in gas fields outside of North America, while the Middle East region contained the largest amount of stranded gas in oil fields outside of North America. Within North America, a significant quantity of stranded gas exists as associated gas in the Bakken Oil Field in North Dakota. Furthermore, in India, the Assam region in the northeast part of the country contains a sizable amount of stranded gas. These two gas sources will serve as case studies for the application of this technology in the field in order to convert stranded natural gas into liquid methanol fuel.

### 1.3.1. North Dakota

The quantity of associated gas produced in the United States in 2013 was documented as 22,218 BCF [16]. Of this total in that year, the largest single source was the state of Texas with 8,199 BCF, and following that was North Dakota with 3,617 BCF. Due to Texas' extensive oil pipeline infrastructure and its close proximity to refinery capacity both within the state as well as in Louisiana, the quantity of this associated gas that was vented and flared was less than in North Dakota. In Texas in 2013, the amount of vented and flared natural gas was 76,113 MMSCF, while in North Dakota in the same year that quantity was 102,855 MMSCF [17]. Furthermore, from January 2012 to February 2015, the fraction of the total associated gas produced in North Dakota that was flared fluctuated between 20% to 37% [18,19]. This was a significant quantity of wasted resource, which, if an inexpensive technology existed to convert that gas to a transportable form such as a liquid fuel, could be avoided.

### 1.3.2. India

The present interest in stranded gas in India is in the geographically remote northeastern provinces of Assam and Tripura. These are the main tea growing regions in India, and happen to contain a sizeable amount of natural gas and oil. This area is blocked off from the main population centers in India by Bangladesh, to its west. The only route without crossing through Bangladesh is through the Siliguri Corridor, which increases travel distance (Fig. 1-1). This geographic isolation makes the gas in this region expensive to transport due to the long distance pipelines required, which only become economical with larger flow rates than are available from these gas fields. Many flares in this region are operated to combust gas that would otherwise be vented.

The stranded gas in this region typically commences flow at a rate of 1 - 3 MMSCFD (Fig. 1-2), with gas pressures in the tens of bar [20]. This tends to increase substantially in the initial time of production. According to Cairn India, this gas contains condensates, water vapor, and other impurities. Oil and Natural Gas Corporation Limited (ONGC) India claims to operate wells as large as 50-70,000 SCMD, or 1.8 - 2.5 MMSCFD. Several other players are proposing solutions to monetize this gas, such as General Electric, which has attempted to use small-scale liquefied natural gas (LNG) units to transport this gas to central processing facilities. Also, ONGC explored electricity generation from the gas, but concluded that the market for electricity was too far away to make transmission lines economical. Unfortunately, due to the stranded nature of the gas and the lack of demand in this region, the market for gas in this corner of India is still not mature. Since the export of gas is not allowed in India as a result of low domestic production, a potential solution to this problem should make domestic use possible, or convert the gas to a form that may be exported. An additional challenge to monetizing the Assam and Tripura stranded gas sources is local political and social resistance, which would make marketing the gas (or the liquid products synthesized from it) difficult. Local industries and government officials would prefer to use the gas to support the local economy.

According to Gas Authority of India Limited (GAIL), in Tripura, the company is capable of producing 3-12 MMSCFD of gas, which can be ramped to 25 MMSCFD if required. This gas contains around 20% by volume of natural gas liquids (NGL) and propane. $H_2S$ appears to not be an issue with gas in this region [21]. Unfortunately, despite these rosy gas production statistics, the main gas pipeline network is still ~ 2,000 km away, beyond the Siliguri Corridor. Simply to get the gas out of the ground will cost the company \$4/MSCF. The volumetric flow rate required for the construction of a dedicated pipeline to be economical is around 20 MMSCMD, which is significantly larger than what is being produced at the moment [22]. In addition, flares are quite far apart, with as much as 200-300 km separation between each one, so the geography of each gas well is itself remote. ONGC claims to have attempted a gas pipeline network via the Assam Gas Company Limited, but this was unsuccessful.

Assam Petrochemicals Ltd. operates a 100 tpd methanol plant in Assam that uses the associated gas from the Upper Assam oil field, using technology from Imperial Chemical Industries in the United Kingdom [23]. The methanol must be marketed to industries around Calcutta, which is ~ 1,700 km away. Currently, there is no restriction on the export of methanol, and is therefore a viable export product if synthesized from a GTL process remotely.

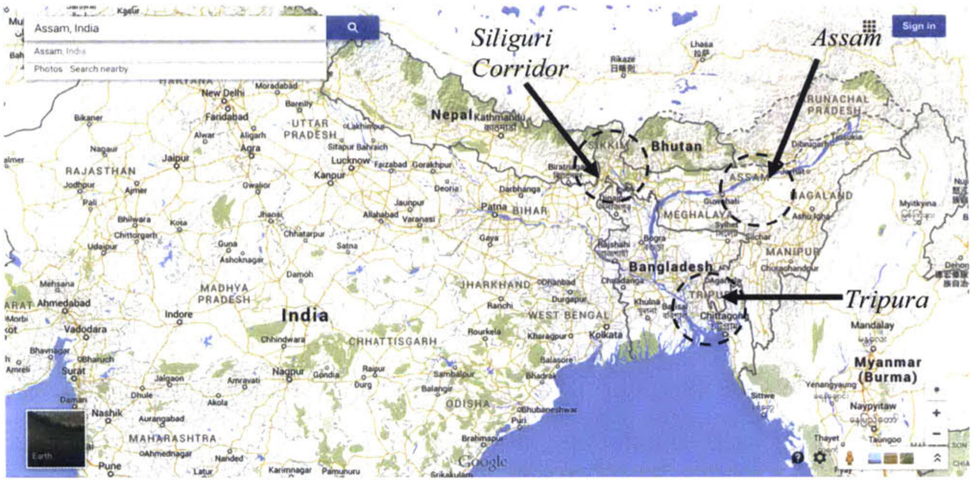

**Figure 1-1.** A map of India showing the locations of Assam and Tripura provinces in the northeast that are blocked from direct access to the main population centers by Bangladesh. The only passageway around Bangladesh is through the Siliguri Corridor [24].

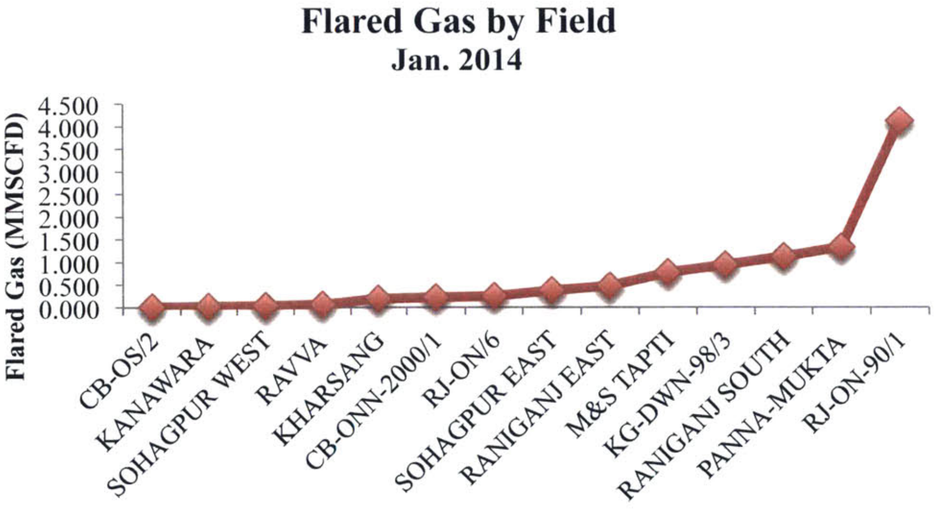

**Figure 1-2.** Flared gas (in MMSCFD) at different gas fields in India [25].

## 1.4. Small-Scale Syngas Production

There is a strong interest in developing compact GTL technologies that can integrate a syngas production unit, liquid fuel synthesis reactor, and compressors in a small footprint, in order to synthesize liquid fuels such as methanol that are significantly cheaper to transport than natural gas. The present challenge is in making the syngas production unit economical on a small scale, as it comprises the majority of the capital cost of large-scale GTL plants. For example, to produce dimethyl ether (DME) from syngas-derived methanol on a large scale, syngas production accounts for 60% of capital costs, while the remaining 40% can be attributed to liquids synthesis [26]. On a small scale, this cost distribution may in fact be even less favorable for the syngas production step is using conventional technologies. Producing syngas in an engine can circumvent this problem due to the engine's low price at a small scale.

It is also possible to bypass syngas production entirely and make liquid products directly from methane, with the help of catalysts, at small scale. This has been researched due to the high capital cost of the syngas step in conventional gas-to-liquids synthesis. Direct catalytic methane-to-methanol synthesis routes can typically only achieve low yields due to the high reactivity of the desired products compared to methane. Therefore, high methane conversion efficiencies come at the expense of low selectivity to methanol [27,28]. A dominant challenge is the stability of the methane molecule and its strong C-H bond (425 kJ/mol), which requires either high temperatures or oxidants to break it up. The syngas step benefits from being able to use oxygen in steam, carbon dioxide and air to break up the methane molecule. Given the low yields achieved by direct catalytic routes, the syngas step is a practical method to follow for a technology that will be implemented in the near term.

## 1.5. Existing Technologies

Conventional GTL technologies are only economical on a large scale. Large GTL plants, such as the Shell Pearl GTL plant in Qatar produces 140,000 barrels of oil equivalent per day (boe/d) of GTL products [29]. Capital costs of large methanol plants are estimated to be \$700 / MT/yr [30], while a 30 ton per day methanol plant using an engine reformer to produce syngas is projected to cost \$360 / MT/yr. [7] Large plants, especially on the scale of Shell Pearl, are associated with long construction times and cost escalation over time. Market conditions can change substantially during the construction period, increasing the economic risks. Furthermore, these technologies do not scale favorably to small scale, and novel approaches are being investigated in this work to address natural gas sources such as associated gas that are either small or have short production periods.

There are several small-scale GTL approaches that are being attempted today. They are described in Table 1-2, contrasting the difference in gas processing capacity between small and large scale. An important factor to the success of small-scale plants is how close the plant capacity can be to production rates at stranded gas sites. The typical associated gas well in the United States produced 400,000–1,500,000 SCFD of natural gas in 2009. [31]

**Table 1-1.** Natural gas processing capacities of existing GTL projects.

| **Company** | **Scale** | **Natural Gas Processing Capacity (MMSCFD)** | **Source** |
|---|---|---|---|
| Oberon | Small | 1.240 | [32] |
| Hydrochem | Small | 1.968 | [33] |
| Gas Technologies | Small | 30.000 | [34] |
| Shell (Pearl) | Large | 1,600.000 | [29] |

## 1.6. The Engine Reformer

The main role of the internal combustion engine in today's society is for the production of power by converting chemical energy in fuel, to useful work. In a conventional engine, complete combustion of a fuel such as $CH_4$ is desired to maximize combustion efficiency and minimize hydrocarbon emissions. The products of complete combustion are carbon dioxide ($CO_2$) and water ($H_2O$) as illustrated in Eq. 1. In this work, the engine was treated as a chemical reactor for the production of syngas, a necessary precursor in the synthesis of longer chain hydrocarbons such as fuels produced by the Fischer-Tropsch method, or methanol [2]. In order to produce syngas, the internal combustion engine was operated in an $O_2$-starved environment (fuel-rich) in order to partially oxidize $CH_4$, thereby generating $H_2$ and CO via Eq. 5. This type of engine is called an "engine reformer". When coupled with a liquids synthesis reactor (Fig. 1-3), the engine reformer may be deployed to convert stranded gas into liquid fuels such as methanol.

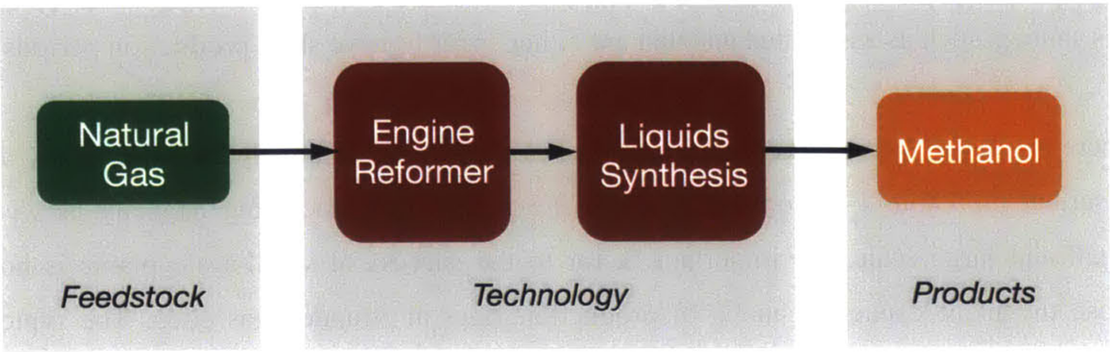

**Figure 1-3.** The engine reformer may be coupled with a liquids synthesis reactor to produce methanol from natural gas.

Because of the industrial application of the engine reformer, a good fraction of the literature occurs in patents. Four relevant patents have been filed for the partial oxidation of methane in an engine. Three of those four are expired. They are US 2543791 A [35] by Texas Co (filed August 25, 1949), US 2846297 A [36] by Maschinenfabrik Augsburg (filed October 8, 1954), US 2922809 A [37] by Sun Oil Co (filed December 13, 1957) and US 20140144397 [38] by MIT (filed March 14, 2013). Texas Co claims to prevent irregular engine operation and misfire by separately introducing fuel (or steam) first, then oxidant, into the cylinder. Residual gases are prevented from combusting by scavenging the residuals with fuel or steam before oxygen is introduced. Maschinenfabrik Augsburg describes an operating procedure for synthesis gas production in an engine, where stoichiometric mixtures are fed to the engine during start-up until an appropriate engine temperature is reached before richer fuel-air mixtures are allowed into the cylinder. Sun Oil Co describes a method to operate a motored engine with 20:1 to 60:1 compression ratio, with methane-oxygen equivalence ratios as high as 18 and pre-heated to 600-800 °F, resulting in peak cylinder temperatures of 1200-1400 °F. The product is an aqueous solution of heavier hydrocarbons such as acetaldehyde, acetone, dimethyl acetal, methanol, ethanol, isopropanol and formaldehyde.

The technology described in this work is protected by the fourth patent [38]. It describes a way to integrate an engine reformer into a small-scale liquids synthesis plant. It describes reusing shaft power and exhaust gas heat to heat the reactants, produce oxygen, provide electricity, or operate a compressor. Requirements for liquids synthesis are well-integrated into the design of the engine's operating regime, such as a ratio of $H_2$ to CO close to 2 in the exhaust. Integration with a specific synthesis technology is a unique feature of this patent, as others are vague or agnostic.

Karim et al [39–41] demonstrated partial oxidation of methane in a dual fuel engine. Experiments were carried out in a 115 mm bore, 152 mm stroke, 14.2:1 compression ratio diesel engine at 1000 rpm and ambient intake temperature. Methane and oxygen-enriched air were fed to the engine and a small quantity of diesel was injected to trigger combustion. Fuel-air equivalence ratios up to 2.5 were tested. The higher equivalence ratios were achieved by oxygen-enrichment of air (up to 80% $O_2$). $H_2$ to CO ratios up to 1.4 were produced with these inputs. Reliable combustion at higher equivalence ratios, where combustion is less likely to occur without significant preheating, can be achieved by reducing the quantity of inert $N_2$ in the oxidizer. In practice, a high $O_2$ oxidizer concentration > 80% requires expensive air separation technology such as vacuum pressure swing adsorption (VPSA) or cryogenic air separation and should be avoided if possible to reduce capital cost, which is especially important for smaller plants.

Yamamoto et al [42] tested partial oxidation of natural gas with in an 8 cylinder diesel engine with 175 mm bore, 220 mm stroke and compression ratio of 7:1 that was modified to perform spark ignition. Natural gas with 94.8% $CH_4$ (2.3% $CO_2$, 2.7% $N_2$, 0.2% $O_2$) was used, and oxygen-enriched air with 97.2% $O_2$ and 2.8% $N_2$ was used for combustion. The elimination of $N_2$ allowed higher flame speeds to be achieved in the cylinder. The maximum fuel-air equivalence ratio that was achieved was $\phi_{HC} = 2.5$ ($O_2/CH_4$ ratio of 0.8), which produced a $H_2/CO$ ratio of 1.65, and carbon in the exhaust gas with a concentration of 0.5 $g/m^3$, or 0.5 mg/L. Combustion stability in these regimes was never quantified. Furthermore, Yamamoto et al used oxygen-enriched air while in this work, only room air was used. In practice, increasing $O_2$ concentration in the oxidizer would require an air separation unit, and future work will investigate economical ways to include such a unit in the field. At the moment, this remains an open question.

Other relevant results in the literature include Ghaffarpour et al, [43] who provide simulation results that show that a methane-air equivalence ratio greater than 1.4 is required to achieve an $H_2/CO$ ratio greater than 1.0. This justifies the decision to target equivalence ratios at or above 2.0, where the production of $H_2$ is preferred. Also, McMillian et al [44] tested spark ignition of natural gas mixtures from fuel-to-air equivalence ratios of 0.6 to 1.6. Their testing was performed in a Ricardo Proteus single cylinder 4-stroke diesel engine with a 130 mm bore and 150 mm stroke, 1.997 L displacement volume, and compression ratio of 13.3:1. Their fuel contained 2.7% $C_2H_6$, 95% $CH_4$, with the balance in $N_2$ and heavier hydrocarbons. With a fuel-to-air equivalence ratio of 1.6, the $H_2$:CO ratio was 1.1. They performed soot detection with a 12:1 dilution ratio, with a constant flow rate of 35-40 cm/s across a 90 mm diameter soot filter. Based on the brake thermal efficiency of the engine of 19% at this equivalence ratio, where fuel flow rate was 2.63 g/s, the calculated soot concentration in their exhaust was 0.7 $g/m^3$, or 0.7 mg/L.

It is important to note that the relevant work in the past surrounding the engine reformer has been non-catalytic. The application of a catalyst in the engine cylinder to aid in the production of syngas has never been attempted in existing work. Therefore, the results described subsequently on catalytic partial oxidation in the engine are preliminary, and will form a foundation for future work on this topic.

The main objective in this work is to empirically demonstrate reliable engine operation and to investigate exhaust gas composition with the following guidelines, using both spark-ignited and catalytic routes. The remainder of this thesis reports on the experiments that were performed to demonstrate these goals, which illustrate the internal combustion engine's compatibility for syngas production, and its potential for use in a small-scale GTL plant for the synthesis of methanol.

- $H_2$ to CO ratio as close as possible to 2:1 in exhaust gas to reduce the demand on water-gas shift in post-processing.
- High $CH_4$ conversion efficiency.
- High $CH_4$ throughput.
- Elevated intake temperatures to increase flame speed of intake mixture and hence allow reliable combustion at higher equivalence ratios.
- Investigation of the effect of spark timing on combustion, and determine optimal spark timing.
- Determination of maximum equivalence ratio with robust combustion with or without addition of $H_2$ or $C_2H_6$.
- Simulation of recycle of $H_2$ from downstream liquids synthesis unit by adding 5% $H_2$ by volume at the intake.
- Simulation of real natural gas compositions with up to 20% $C_2H_6$ by volume in $CH_4$.
- Measurement of soot concentrations in engine exhaust to evaluate performance at different equivalence ratios.
- Maintenance of reasonable peak cylinder temperatures when performing catalytic partial oxidation by simultaneously performing $CH_4$ dry reforming with $CO_2$.

# 2. Experimental Methods

The experimental setup consisted of two engine systems on separate drivetrains (Appendix A). The first was a Yanmar four-cylinder marine diesel engine (the "spark-ignited engine"), and the second was a Lister-Petter single-cylinder diesel generator (the "catalytic engine"). Due to limited floor space, the same controls and measurement systems were shared so that the catalytic engine, which was installed at a later time, could utilize the same systems already in place for the spark-ignited engine. The two engines shared a control system to regulate intake composition, a common power supply for heating elements, as well as data acquisition hardware and data processing software. Separate pressure and temperature probes were used for each engine. In-cylinder pressure was only measured in the spark-ignited engine, so engine cycle phasing was measured and controlled only in that system. Finally, exhaust gases were measured and processed with the same GC system and syngas burner.

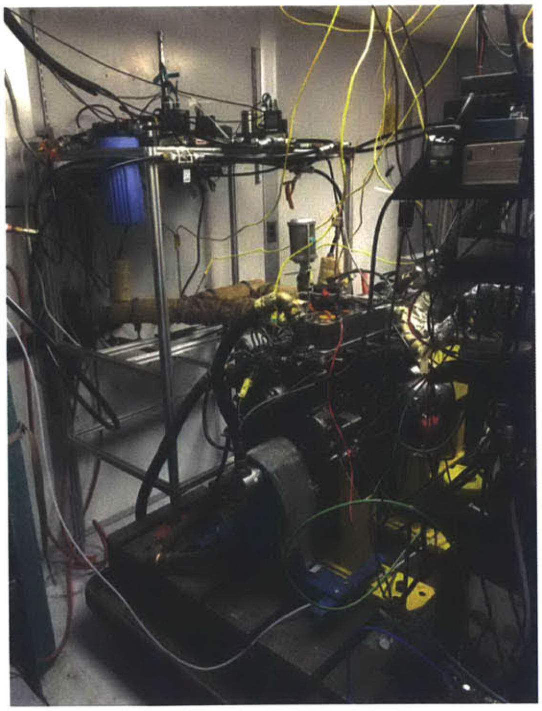

**Figure 2-1.** The Yanmar 4TNV84T marine diesel engine (on yellow stand) was fixed to a cast iron T-slotted test bed. The intake composition and temperature control system is to the left of the engine. The data acquisition hardware and power supplies are on an instrument tower to the right of the engine.

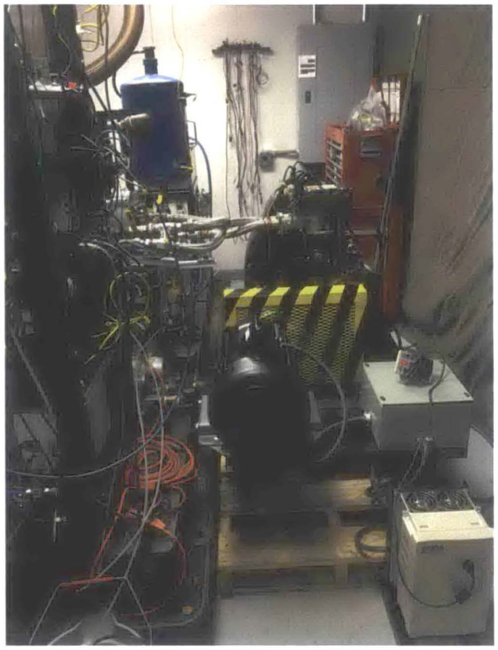

**Figure 2-2.** The Lister-Petter TR1 single-cylinder diesel engine was fixed to a separate pallet to the right of the cast iron T-slotted test bed. The intake composition and temperature control system is to the left of the engine. The data acquisition hardware and power supplies are on an instrument tower also to the left of the engine.

## 2.1. Calculations

This section describes the calculations used for the two engines tested in this. The first section reviews the variables used to analyze the results from a spark-ignited cylinder in a Yanmar diesel engine. The subsequent section reviews the variables used to analyze the results from a single-cylinder Lister-Petter engine performing partial oxidation with a catalyst-coated metallic foam contained in the piston bowl.

In both engines, the total mass flow rate drawn ($\dot{m}_{engine}$) was a function of the engine speed ($N$), the displacement volume, the intake pressure ($p_i$), the molar mass of the intake charge ($M_{mix}$), the number of revolutions per cycle ($n_R$; since both engines used were four-stroke, this value is 2), the Ideal Gas constant ($R$), and the intake temperature ($T_i$). This value is approximate, as the volumetric efficiency of the intake system ($\eta_V$) is not included. Since $\eta_V$ is ~ 0.8 - 0.9, it was sufficient to correct for the discrepancy by manipulating $p_i$ until the desired intake pressure according to the intake pressure transducer was reached.

$$\dot{m}_{engine} \sim \frac{N\, V_d\, p_i\, M_{mix}}{n_R\, R\, T_i} \qquad (13)$$

While the intake compositions that were tested were different in each engine, the same process was used to perform calculations. First, the desired charge composition was used to calculate $M_{mix}$, and combined with the other engine operating parameters, $\dot{m}_{engine}$ was calculated. Then, the charge composition was used to determine the mass fraction of each constituent gas, and the mass flow rate of each gas was calculated as the product of its mass fraction and $\dot{m}_{engine}$. Finally, the standard volumetric flow rate of the gas was calculated by dividing individual gas mass flow rates by their standard densities, and converting to liters per minute, which were the units used by the mass flow controllers.

### 2.1.1. Spark-Ignited Engine Calculations

In the spark-ignited engine, the methane-air equivalence ratio ($\phi_M$) was used where the fuel was composed only of methane. When used in cases with varying $C_2H_6$ concentrations in the fuel, $\phi_M$ was the value used in Eq. 15. This will be noted in cases where this occurs. At the same time, the hydrocarbon-air equivalence ratio ($\phi_{HC}$) was used to indicate the total equivalence ratio considering both methane and ethane as fuels, and was calculated using Eq. 17. These ratios were modified in real-time by the mass flow controllers. Hydrogen was not considered as a fuel in either of these calculations, when it was present. This is to highlight its role as a precursor to liquids synthesis, as well as a component from downstream recycling. For ideal partial oxidation, $\phi_M = 4$ (Eq. 14).

The combustion process does change when hydrogen is introduced to the intake. However, because hydrogen is a major product of the combustion process, the fuel equivalence ratio ($\phi_{HC}$) based only on the hydrocarbons is considered to be the relevant parameter.

The intake composition was first defined with respect to $CH_4$ (Eq. 14). Being able to operate without either $C_2H_6$ or $H_2$ is critical so that the effect of adding those gases could be detected, but also for a smooth start-up procedure while the engine intake was heating up. For example, to ramp up to the higher equivalence ratios made possible by higher intake temperatures, the engine was first operated at close to $\phi_M = 1.0$ to provide steady combustion at lower intake temperatures.

$$CH_4 + \frac{2}{\phi_M}\left(O_2 + 3.773\, N_2\right) \tag{14}$$

Natural gas can contain a significant quantity of $C_2H_6$ and other higher hydrocarbons. $C_2H_6$ was added to $CH_4$ to investigate the impact of substantial fractions of these hydrocarbons on the reformer. $x_{C_2H_6}$ was defined as the ratio between the number of moles of $C_2H_6$ to the total number of moles of $CH_4$ and $C_2H_6$. Based on the composition set by $\phi_M$, the new composition simply replaced $x_{C_2H_6}$ moles of $CH_4$ with $C_2H_6$, for every mole of $CH_4$, without modifying the quantity of air. Hence, the total equivalence ratio ($\phi_{HC}$) was higher for any given $\phi_M$ when $C_2H_6$ was present, as more $O_2$ is required to completely combust $C_2H_6$.

$H_2$ was added in some engine experiments to simulate the recycle of unused $H_2$, after separation from the tail gas of a methanol synthesis reactor. Steady-state flow models of the entire gas-to-liquids process for methanol synthesis indicate that the engine put can be 5 mol% $H_2$. This model assumed 60% conversion of the syngas to methanol in a two-stage synthesis step. Note that recycling of the tail gas into the methanol synthesis reactor may not be feasible because of the nitrogen content so an $H_2/N_2$ separator would be needed to accomplish the $H_2$ recycle. The intake composition including both $C_2H_6$ and $H_2$ is shown in Eq. 15. The intake composition required for complete combustion of $CH_4$ and $C_2H_6$ is shown in Eq. 16. Therefore, $\phi_{HC}$ can be computed using Eq. 17, where $H_2$ was not considered to be a fuel. It is simply the ratio of air required in Eq. 16 to that required in Eq. 15. Note that $\phi_{HC} = \phi_M$ when $x_{C_2H_6} = 0$, as expected.

$$\begin{aligned}(1 - x_{C_2H_6})\, CH_4 + x_{C_2H_6}\, C_2H_6 + \frac{2}{\phi_M}\,(O_2 + 3.773\, N_2) \\ + \frac{x_{H_2}}{1 - x_{H_2}}\left[1 + \frac{2}{\phi_M} 4.773\right] H_2\end{aligned} \tag{15}$$

$$\begin{aligned}(1 - x_{C_2H_6})\, CH_4 + x_{C_2H_6}\, C_2H_6 + [2(1 - x_{C_2H_6}) + \tfrac{7}{2} x_{C_2H_6}\,](O_2 + 3.773\, N_2) \\ + \frac{x_{H_2}}{1 - x_{H_2}}\left[1 + \frac{2}{\phi_M} 4.773\right] H_2\end{aligned} \tag{16}$$

$$\phi_{HC} = \frac{\phi_M}{2}\left[2(1 - x_{C_2H_6}) + \frac{7}{2} x_{C_2H_6}\right] \tag{17}$$

The mole fraction of each component in the intake charge ($\bar{x}_i$) was calculated by taking the ratio of the number of moles of that gas shown in Eq. 15 ($n_i$), to the total number of moles in the same equation ($n_{CH_4} + n_{C_2H_6} + n_{air} + n_{H_2}$). Since $n_{air}$ was a function of $\phi_M$ in its denominator, we divide both numerator and denominator in $\bar{x}_i$ by $n_{air}$ in order to avoid dividing by zero when the intake charge only consists of air. This expression for $\bar{x}_i$ is shown in Eq. 18.

$$\bar{x}_i = \frac{n_i}{n_{CH_4} + n_{C_2H_6} + n_{air} + n_{H_2}} = \frac{\frac{n_i}{n_{air}}}{\frac{n_{CH4}}{n_{air}} + \frac{n_{C2H6}}{n_{air}} + 1 + \frac{n_{H2}}{n_{air}}} \tag{18}$$

For example, to calculate the mole fraction of methane in the intake charge, $\bar{x}_i = \bar{x}_{CH_4}$, and $\frac{n_i}{n_{air}} = \frac{n_{CH4}}{n_{air}}$. The values of each molar ratio in the equation for $\bar{x}_i$ are shown in Eqs. 19-21, demonstrating that none of the terms in $\bar{x}_i$ are infinite when $\phi_M = 0$.

$$\frac{n_{CH_4}}{n_{air}} = \frac{\phi_M(1 - x_{C_2H_6})}{2(4.773)} \tag{19}$$

$$\frac{n_{C_2H_6}}{n_{air}} = \frac{\phi_M(x_{C_2H_6})}{2(4.773)} \tag{20}$$

$$\frac{n_{H_2}}{n_{air}} = \frac{\phi_M}{2(4.773)}\frac{x_{H_2}}{1 - x_{H_2}}\left[1 + \frac{2}{\phi_M}4.773\right] = \left[\frac{\phi_M}{2(4.773)} + 1\right]\frac{x_{H_2}}{1 - x_{H_2}} \tag{21}$$

A weighted average by mole of the molar masses of each constituent ($M_i$) was calculated to determine the molar mass of the mixture ($M_{mix}$) using Eq. 22.

$$M_{mix} = \sum_i \bar{x}_i\, M_i \tag{22}$$

With $M_{mix}$ and the other known engine operating parameters, the mass flow rate drawn by the engine could be calculated. The mass fraction of each component ($x_i$) was calculated using Eq. 23.

$$x_i = \frac{M_i \frac{n_i}{n_{air}}}{M_{CH_4}\frac{n_{CH_4}}{n_{air}} + M_{C_2H_6}\frac{n_{C_2H_6}}{n_{air}} + M_{air} + M_{H_2}\frac{n_{H_2}}{n_{air}}} \tag{23}$$

The mass flow rate of each component (Eq. 24, in g/min), and volumetric flow rate at standard conditions of each component (Eq. 25, in L/min) were, respectively,

$$\dot{m}_i = x_i\, \dot{m}_{engine} \tag{24}$$

and

$$\dot{V}_i = \frac{\dot{m}_i}{\rho_{std,i}} \tag{25}$$

The densities at standard conditions of each gas ($\rho_{std,i}$) that were used in calculations are shown in Table 2-1. Standard conditions were defined to be 25 °C and 14.696 PSIA. The volumetric flow rate for each gas type was separately communicated to each mass flow controller.

**Table 2-1.** Standard gas densities used for mass flow controller standard volumetric flow rate calculations.

| **Gas *i*** | **$\rho_{std,i}$ (g/L)** |
|---|---|
| Air | 1.1840 |
| $CH_4$ | 0.6569 |
| $C_2H_6$ | 1.2385 |
| $H_2$ | 0.08235 |

The conversion efficiency of $CH_4$ and $C_2H_6$, and carbon balance were calculated by normalizing to the $N_2$ (which is inert in the process, to very high accuracy) throughput. No $NO_x$ gases were detected from gas chromatography (GC). These conversions were calculated by comparing mole throughput in exhaust mixtures to those in the intake, and are expressed as $CH_4$ conversion efficiency $X_{CH_4}$(Eq. 26), $C_2H_6$ conversion efficiency $X_{C_2H_6}$ (Eq. 27), and the moles of carbon in the exhaust relative to moles of carbon in the intake $C_{Bal}$ (Eq. 28). The intake mole fractions of $CH_4$ ($\bar{x}_{CH_4,in}$) and $C_2H_6$ ($\bar{x}_{C_2H_6,in}$) were determined analytically using the methods shown above, and the exhaust mole fractions of $CH_4$ ($\bar{x}_{CH_4,exh}$), $C_2H_6$ ($\bar{x}_{C_2H_6,exh}$) and $N_2$ ($\bar{x}_{N_2,exh}$) were measured using GC readings. $X_{CH_4}$ and $X_{C_2H_6}$ represent the percentage of $CH_4$ and $C_2H_6$ that were used up in the engine, respectively. $C_{Bal}$ compares the amount of carbon at the intake to that in the exhaust. A major deviation from 1.0 may suggest excessive soot production.

$$X_{CH_4} = \left[1 - \frac{\bar{x}_{CH_4,exh}}{\bar{x}_{CH_4,in}} \cdot \frac{\bar{x}_{N_2,in}}{\bar{x}_{N_2,exh}}\right] \times 100\% \tag{26}$$

$$X_{C_2H_6} = \left[1 - \frac{\bar{x}_{C_2H_6,exh}}{\bar{x}_{C_2H_6,in}} \cdot \frac{\bar{x}_{N_2,in}}{\bar{x}_{N_2,exh}}\right] \times 100\% \tag{27}$$

$$C_{Bal} = \frac{2\bar{x}_{C_2H_6,exh} + \bar{x}_{CO,exh} + \bar{x}_{CO_2,exh} + \bar{x}_{CH_4,exh}}{\bar{x}_{CH_4,in} + 2\bar{x}_{C_2H_6,in}} \cdot \frac{\bar{x}_{N_2,in}}{\bar{x}_{N_2,exh}} \tag{28}$$

The intake mole fractions of $N_2$ ($\bar{x}_{N_2,in}$) were calculated using Eq. 29.

$$\bar{x}_{N_2,in} = \frac{\frac{n_{N_2}}{n_{air}}}{\frac{n_{CH_4}}{n_{air}} + \frac{n_{C_2H_6}}{n_{air}} + 1 + \frac{n_{H_2}}{n_{air}}} = \frac{\frac{3.773}{4.773}}{\frac{n_{CH_4}}{n_{air}} + \frac{n_{C_2H_6}}{n_{air}} + 1 + \frac{n_{H_2}}{n_{air}}} \tag{29}$$

### 2.1.2. Catalytic Engine Calculations

In the catalytic engine, the fuel-air equivalence ratio ($\phi_M$) was held constant at 4 for ideal stoichiometric conditions for partial oxidation. Methane was the only fuel used in these experiments. In order to limit the amount of heat released in the cylinder during these tests, partial oxidation was combined with dry reforming. That way, the exothermicity of partial oxidation could be balanced by the endothermicity of dry reforming. By tuning the relative quantity of each reaction, the steady state temperature of the catalyst could be controlled, thereby preventing temperatures from rising above the melting point of the catalytic washcoat.

The chemical equation of the general reaction is shown in Eq. 30. The factor $\frac{|\Delta H^0_{298,POX}|}{\Delta H^0_{298,DR}}$ is the ratio of the absolute value of the reaction enthalpy of methane partial oxidation ($|\Delta H^0_{298,POX}|$) to the reaction enthalpy of methane dry reforming ($\Delta H^0_{298,DR}$). It is the number of moles of $CH_4$ and $CO_2$, in equal parts, to produce a net zero reaction enthalpy for the partial oxidation of 1 mole of $CH_4$.

$$CH_4 + \frac{2}{\phi_M}(O_2 + 3.773\,N_2)$$

$$+y_{DR}\frac{|\Delta H^0_{298,POX}|}{\Delta H^0_{298,DR}}\left[(CH_4 + CO_2) + \left(a_{CO_2} - 1\right)CO_2\right] \tag{30}$$

The net reaction enthalpy of this equation is $\Delta H^0_{298,POX} + y_{DR}|\Delta H^0_{298,POX}|$, assuming complete conversion of methane to CO and $H_2$ via partial oxidation and dry reforming, and $y_{DR}\frac{|\Delta H^0_{298,POX}|}{\Delta H^0_{298,DR}}\left(a_{CO_2} - 1\right)$ moles of $CO_2$ are inert in the reaction. $y_{DR}$ is a tuning factor that allows the net reaction enthalpy to be modulated, while $a_{CO_2}$ provides excess $CO_2$, both to increase methane conversion in dry reforming as well as to serve as a diluent to reduce maximum cylinder temperatures. $a_{CO_2}$ represents the number of times more $CO_2$ that is added to the mixture than is required for stoichiometric dry reforming. For example, $a_{CO_2} = 2$ means that twice as much $CO_2$ than is required for stoichiometric dry reforming was added. Eq. 30 is not simplified in the dry reforming term in order to differentiate between dry reforming gas ( $y_{DR}\frac{|\Delta H^0_{298,POX}|}{\Delta H^0_{298,DR}}(CH_4 + CO_2)$ ) and excess $CO_2$ ( $y_{DR}\frac{|\Delta H^0_{298,POX}|}{\Delta H^0_{298,DR}}\left(a_{CO_2} - 1\right)CO_2$ ).

The same method was used here to calculate mole and mass fractions of each constituent gas as in the previous section. The mole fraction of each component in the intake charge ($\bar{x}_i$) was be calculated by taking the ratio of the number of moles of that gas ($n_i$) in Eq. 30, to the total number of moles in that equation ($n_{CH_4} + n_{air} + n_{CO_2}$), and is shown in Eq. 31. Again, both numerator and denominator in $\bar{x}_i$ were divided by $n_{air}$ in order to avoid dividing by zero when the intake charge only consisted of air (when no $CH_4$ was present). Therefore,

$$\bar{x}_i = \frac{n_i}{n_{CH_4} + n_{air} + n_{CO_2}} = \frac{\frac{n_i}{n_{air}}}{\frac{n_{CH4}}{n_{air}} + 1 + \frac{n_{CO2}}{n_{air}}} \tag{31}$$

The values of each molar ratio in the equation for $\bar{x}_i$ are shown in Eqs. 32-33. Again, none of the terms in $\bar{x}_i$ are infinite when $\phi_M = 0$.

$$\frac{n_{CH_4}}{n_{air}} = \frac{\phi_M \left(1 + y_{DR}\frac{|\Delta H^0_{298,POX}|}{\Delta H^0_{298,DR}}\right)}{2(4.773)} \qquad (32)$$

$$\frac{n_{CO_2}}{n_{air}} = \frac{\phi_M y_{DR}\frac{|\Delta H^0_{298,POX}|}{\Delta H^0_{298,DR}} a_{CO_2}}{2(4.773)} \qquad (33)$$

A weighted average by mole of the molar masses of each constituent ($M_i$) was calculated to determine the molar mass of the mixture ($M_{mix}$), also using Eq. 22. With $M_{mix}$ and the other known engine operating parameters, the mass flow rate drawn by the engine could be calculated. The mass fraction of each component ($x_i$) was found using Eq. 34.

$$x_i = \frac{M_i \frac{n_i}{n_{air}}}{M_{CH_4}\frac{n_{CH_4}}{n_{air}} + M_{air} + M_{CO_2}\frac{n_{CO_2}}{n_{air}}} \qquad (34)$$

The mass flow rate of each component (in g/min), and volumetric flow rate at standard conditions of each component (in L/min) were calculated using the same equations used in the previous section (Eq. 24 and 25 respectively). That is, the mass flow rate was determined by multiplying the mass fraction of each component by the total mass flow rate drawn by the engine, and the standard volumetric flow rate was calculated by dividing the individual mass flow rates by the corresponding gas' density at standard conditions shown in Table 2-1.

The conversion efficiency of $CH_4$ ($X_{CH_4}$, Eq. 35), conversion efficiency of $O_2$ ($X_{O_2}$, Eq. 36), production efficiency of $CO_2$ ($CO_{2,Bal}$, Eq. 37), and carbon balance ($C_{Bal}$, Eq. 38) were calculated by normalizing to the $N_2$ throughput following the same methods used in the previous section. The intake mole fractions of $CH_4$ ($\bar{x}_{CH_4,in}$) and $CO_2$ ($\bar{x}_{CO_2,in}$) were determined analytically using Eq. 31, and the exhaust mole fractions of $CH_4$ ($\bar{x}_{CH_4,exh}$), $CO_2$ ($\bar{x}_{CO_2,exh}$) and $N_2$ ($\bar{x}_{N_2,exh}$) were measured using gas chromatography. $X_{CH_4}$ and $X_{O_2}$ represent the percentage of $CH_4$ and $O_2$ that were used up in the engine, respectively.

$CO_{2,Bal}$ compares the amount of CO$_2$ in the exhaust relative to that in the intake, expressed as a percentage. $C_{Bal}$ compares the amount of carbon at the intake to that in the exhaust.

$$X_{CH_4} = \left[1 - \frac{\bar{x}_{CH_4,exh}}{\bar{x}_{CH_4,in}} \cdot \frac{\bar{x}_{N_2,in}}{\bar{x}_{N_2,exh}}\right] \times 100\% \tag{35}$$

$$X_{O_2} = \left[1 - \frac{\bar{x}_{O_2,exh}}{\bar{x}_{O_2,in}} \cdot \frac{\bar{x}_{N_2,in}}{\bar{x}_{N_2,exh}}\right] \times 100\% \tag{36}$$

$$CO_{2,Bal} = \left[\frac{\bar{x}_{CO_2,exh}}{\bar{x}_{CO_2,in}} \cdot \frac{\bar{x}_{N_2,in}}{\bar{x}_{N_2,exh}}\right] \times 100\% \tag{37}$$

$$C_{Bal} = \frac{\bar{x}_{CO,exh} + \bar{x}_{CO_2,exh} + \bar{x}_{CH_4,exh}}{\bar{x}_{CH_4,in} + \bar{x}_{CO_2,exh}} \cdot \frac{\bar{x}_{N_2,in}}{\bar{x}_{N_2,exh}} \tag{38}$$

The intake mole fractions of N$_2$ ($\bar{x}_{N_2,in}$) were calculated using Eq. 39.

$$\bar{x}_{N_2,in} = \frac{\frac{n_i}{n_{air}}}{\frac{n_{CH4}}{n_{air}} + 1 + \frac{n_{CO2}}{n_{air}}} = \frac{\frac{3.773}{4.773}}{\frac{n_{CH4}}{n_{air}} + 1 + \frac{n_{CO2}}{n_{air}}} \tag{39}$$

## 2.2. Spark-Ignited Engine Setup

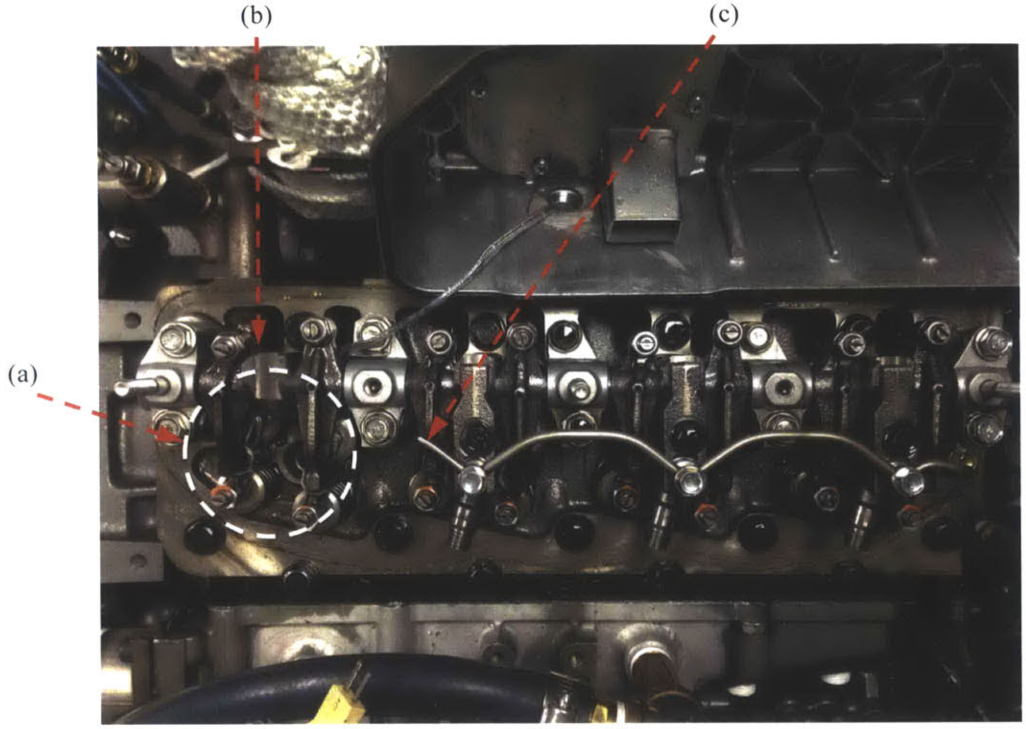

**Figure 2-3.** The spark-ignited test cylinder (a) is on the furthest left in this image. The cylinder pressure sensor is placed beneath the diesel injector pedestal (b). The fuel return line (c) was cut and welded for the test cylinder.

A modified Yanmar 4TNV84T diesel-injected engine with an 84 mm bore, 90 mm stroke and compression ratio of 18.9:1 was used to perform spark-ignited partial oxidation. This was a four-stroke engine with a total displacement of 1.995 L in four cylinders, and four valves per cylinder. One of the 4 cylinders was converted to perform spark-ignition (the "test cylinder"), while the remaining three cylinders (the "diesel cylinders") were not modified. In the test cylinder, the diesel injector was removed to make room for an NGK R847-11 surface discharge racing spark plug, and the section of the original diesel fuel return line for this cylinder was removed, and the remaining return line was welded and sealed. The diesel injector opening in the cylinder head was threaded to accommodate the M8.0 x 1.0 threads on the spark plug, and a washer and shoulder on the ground electrode of the spark plug formed a sealing surface for combustion gases. The spark plug was tightened to 10 N-m torque according to NGK specifications [45].

A second hole under the diesel injector pedestal was drilled to accommodate a Kistler 6052C high-temperature pressure sensor to measure in-cylinder pressure during combustion. The pressure sensor mounting bore was machined according to Kistler specifications [46]. The sensor's sensitivities at different calibrated ranges are shown in Table 2-2. A Kistler 5010 Dual Mode Amplifier converted the charge reading on the piezoelectric crystal from the pressure sensor to a readable voltage, and provided amplification of the voltage for reading by the data acquisition system. As an approximation for the sensitivities at the calibrated ranges shown in Table 2-2, the charge amplifier was tuned to -19.7 pC/bar, and a conversion factor of 20 bar/V. Due to thermal gradients in the cylinder, cylinder temperature was not measured. No modifications were made to the diesel injection systems of the diesel cylinders.

**Table 2-2.** The sensitivity of the cylinder pressure sensor at different calibrated pressure ranges.

| Calibrated Range (bar) | Sensitivity (pC/bar) |
|---|---|
| 0 ... 250 (200 °C) | -19.68 |
| 0 ... 150 (200 °C) | -19.74 |
| 0 ... 100 (200 °C) | -19.76 |

The intake and exhaust manifolds of the test cylinder were separated from those of the remaining three cylinders. A separation plate was welded inside the intake manifold to separate the intake charge for the test cylinder from room air that was drawn in for the three diesel cylinders. An Aquatrol, Inc. 88C 1"x1.25" remote-discharge pop-safety valve with 184 SCFM capacity and 60 psi relief pressure provided safety relief if intake pressures rose to unsafe values (> 4 bar gauge). Since there were two intake valves, two tubes were installed to direct gas from the upstream mixing system to each of the two valves of the test cylinder. Two Omega ungrounded low noise HG K-type thermocouples with stainless steel sheaths, 1/16" outer diameter, and 12" lengths were used to measure intake temperature, one in each of the two intake tubes, with the probe point at the opening of each of the two intake runners.

The exhaust manifold for the test cylinder was physically separated from that of the diesel cylinders. A custom-built fitting was made to adapt from a flanged interface on the exhaust manifold of the diesel cylinders, to 1.5" NPT braided metal hose, which directed the diesel exhaust stream to an exhaust stack. The test cylinder exhaust was guided through a separate system of metal piping to a natural gas burner to complete oxidation of the syngas components. A small fraction of this exhaust stream was directed towards the GC sampling system. A Data Instruments Model SA pressure transducer with 1-6 VDC output voltage corresponding to 0-25 PSIA pressure was installed in each of the test manifolds. A third thermocouple of the same type mentioned above was installed in the exhaust manifold of the test cylinder.

A Digalog 107 hp dynamometer (with DyneSystems DYN-LOC IV digital dynamometer controller) was coupled to the engine flywheel, however, this was not used to control the engine as the three diesel cylinders were sufficient to drive the engine and maintain a constant speed ~ 1100 rpm. The speed output from the dynamometer was read during data acquisition to ensure constant speed control.

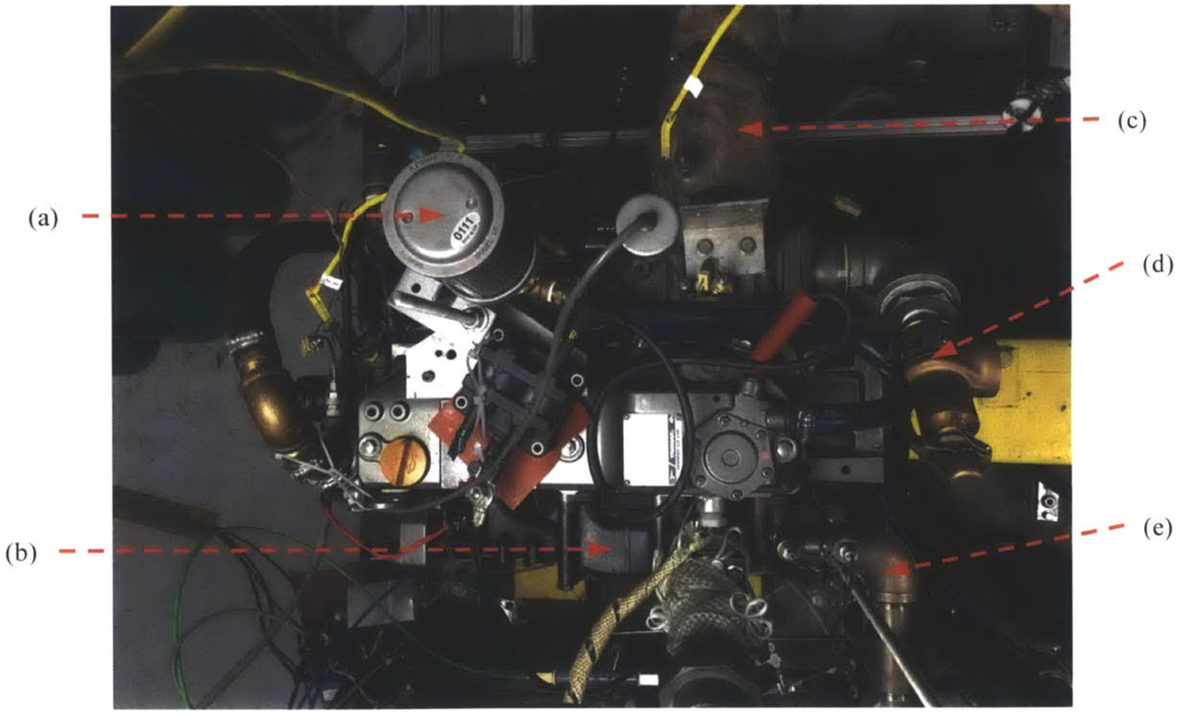

**Figure 2-4**. Top view of the Yanmar engine. (a) air intake filter for diesel cylinders; (b) exhaust manifold for diesel cylinders; (c) heated intake for spark-ignited cylinder; (d) intake manifold pressure relief valve for spark-ignited cylinder; (e) exhaust manifold for spark-ignited cylinder.

### 2.2.1. Engine Coolant and Fuel Systems

Permanent Anti-Freeze consisting of 50% ethylene glycol and 50% water was used as engine coolant. This was pumped through the engine coolant jacket with a Franklin Electric ¾ hp 115/230 V 50 Hz water pump. An AccuTherm Inc. 1.5 kW 120 V single-phase immersion heater and Omega CN7800 heater controller were used to maintain the coolant temperature at 95 °C. Ultra low sulfur diesel fuel (NA1993, PGIII) was burned in the diesel cylinders to provide power to drive the test piston.

### 2.2.2. Modifying Compression Ratio

The compression ratio of the test cylinder was reduced to simulate combustion in a conventional natural gas engine. This was performed to demonstrate that reliable combustion was possible despite a decrease in compression ratio. A natural gas engine with much larger displacement was being selected for use in a demonstration plant, where all cylinders would perform partial oxidation and syngas from the engine exhaust would be used to synthesize liquid methanol. Due to the complexity and unreliability that arose from modifying a diesel cylinder to perform spark-ignition in this work, the demonstration engine would be a spark-ignited natural gas engine with a compression ratio of approximately 14:1 requiring no major modifications. To prove that these parameters were possible in the demonstration engine, the original compression ratio of 18.9:1 in the test cylinder was reduced to 13.8:1.

A Yanmar 4TNV84T Turbo Major Overhaul Kit with standard bore, rod, and bearing sizes from MaxiForce was used to rebuild the engine with a new piston geometry in the test cylinder. A Y129508-22080 piston, contained in this rebuild kit, was used as a reference in the design of the new geometry. The original piston geometry contained a re-entrant bowl in the piston crown, which consisted of a flat lip, rounded sidewalls, and a cylindrical protrusion at the base. The intended purpose of the bowl geometry was to enhance swirl that was induced by the intake port, and improve mixing and turbulence of air and fuel during the compression stroke [47,48] as a way to reduce particulate emissions. However, a significant quantity of the piston crown was flat (the "squish area"), which suggests the volume of charge that was subject to squish was not insignificant. Squish occurs close to the end of the compression stroke when the portion of the charge that is closest to the cylinder head moves radially inward or outward [1]. Therefore, in addition to reducing compression ratio, a second goal in this modification was to reduce the amount of squish area in the cylinder.

The original piston diameter and internal bowl dimensions were measured using calipers to provide an estimate for the piston geometry. This geometry was then translated to a 3D model using SolidWorks. For the modification, the protruding cylinder was first removed (this cylinder can be seen at the base of the piston bowl in Figure 2-5a). Then, the squish area was iteratively removed beginning in the center of the piston crown, and moving radially outward. Through each iteration of material removal performed in SolidWorks, the current volume was compared to the volume of the original piston model using the "Mass Properties" function in the software. This volume reduction ($V_{reduced}$) was subtracted from the original clearance volume ($V_c$) in the engine to determine the new compression ratio according to Eq. 40. This was performed iteratively until a compression ratio of ~14:1 was achieved.

$$r_{c,new} = \frac{V_d + [V_c - V_{reduced}]}{[V_c - V_{reduced}]} \qquad (40)$$

The SolidWorks models were designed in the positive x-y quadrant, and any drive and check surfaces were below the x-y plane. They were exported as solid .igs files using NURBS representation, and imported in MasterCAM to create toolpaths for CNC milling. The original piston geometry was used for the geometry of the stock material. Then, the modified piston geometry was used to select the drive and check surfaces, as well as containment boundaries. A 3/8" flat endmill was used for a single-tool job using the toolpaths shown in Table 2-4. Surface rough and finish parallel toolpaths (#1 and #2) were used to remove the protrusion at the bottom of the bowl. Then, a surface rough pocket toothpath (#3) was used to remove the bulk of the material along the side walls of the piston bowl. Finally, a surface finish radial toolpath was used to produce the surface finish on the modified piston crown. The four toolpaths were then exported to a .NC file, which was used to populate machine events on the ProtoTRAK SMX CNC software of a Southwestern Industries Trak DPM2 SX2P bed mill. The CAM simulation is shown in Figure 2-6a, and the modified piston in Figure 2-6b.

An unused Y129508-22080 piston was weighed before any modifications were made to it. It was then machined on the Trak DPM2 using a 3/8" coated carbide flat end mill. After machining, the new piston was weighed again. The difference in weights pre- $(m_{p,i})$ and post-machining $(m_{p,f})$ was used to approximate the volume of aluminum that was removed from the piston, which was simply the difference in piston weights divided by the density of aluminum $(\rho_p)$, $V_{reduced} = \frac{m_{p,i}-m_{p,f}}{\rho_p}$. The geometric and material properties of the modified piston are showing in Table 2-3. In order to install the new piston in the test cylinder, the engine was detached from the intake, exhaust, fuel, and electrical systems, from its stand, lifted by a crane, and then attached to a portable engine stand. This allowed easy access to the big end of the connecting rod from the crankcase. First, The fuel filter was replaced, then, the valve cover and cylinder head were removed and cleaned. The engine oil was allowed to drain from the oil pan overnight, and the oil pan was removed and cleaned as well. The engine was turned upside down to detach the test cylinder connecting rod from the crankshaft. The modified piston was installed (Figure 2-7), the oil pan was returned, and a new gasket was used to seal the surface between the cylinder head and engine block. The valve clearances were returned to Yanmar specifications, and the engine was returned to the test bed. The thickness of the new gasket $(t_{g,new})$ was larger than the original $(t_{g,old})$, so the additional volume that was added as a result $(V_{g,added})$ was used in the new calculation of compression ratio. This is shown in Eq. 41. The r

$$r_{c,new} = \frac{V_d+\left[V_c-V_{reduced}+V_{g,added}\right]}{\left[V_c-V_{reduced}+V_{g,added}\right]} = 13.8 \qquad (41)$$

**Table 2-3.** The piston geometric and material parameters that were used to calculate the modified compression ratio.

| | |
|---|---|
| $V_d$ | 0.499 L |
| $V_c$ | 0.028 L |
| $\rho_p$ | 2830 kg/m$^3$ |
| $m_{p,i}$ | 508.07 g |
| $m_{p,f}$ | 480.27 g |
| $V_{reduced}$ | 0.010 L |
| $t_{g,new} - t_{g,old}$ | 0.022 cm |
| $V_{g,added}$ | 0.039 L |
| $r_{c,new}$ (-) | 13.8 |

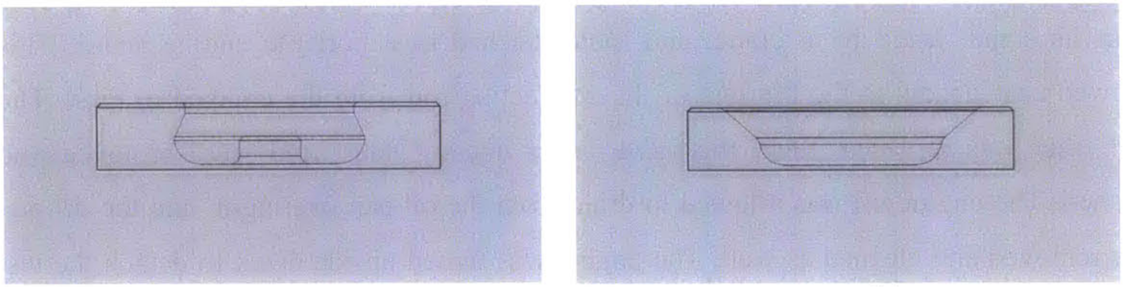
(a) (b)

**Figure 2-5.** (a) the original piston geometry as viewed from the side. (b) the modified piston geometry as viewed from the side.

**Table 2-4.** The machine settings that were programmed into MasterCAM to machine the part.

| Toolpath: | Rough/ Finish: | Type: | Spindle Speed (rpm): | Feed Rate (ipm): | Plunge Rate (ipm): | Stock to Leave on Drive (in): | Max. Stepdown (in): | Max. Stepover: | Cutting Method: |
|---|---|---|---|---|---|---|---|---|---|
| 1 | Rough | Parallel | 1700 | 7 | 7 | 0.05 | 0.1 | 0.2 in | Zigzag |
| 2 | Finish | Parallel | 2000 | 6.5 | 6.5 | 0 | - | 0.05 in | Zigzag |
| 3 | Rough | Pocket | 1700 | 7.5 | 7.5 | 0.05 | 0.1 | 0.2 in | Parallel Spiral |
| 4 | Finish | Radial | 2000 | 6.5 | 6.5 | 0 | - | 2° | Zigzag |

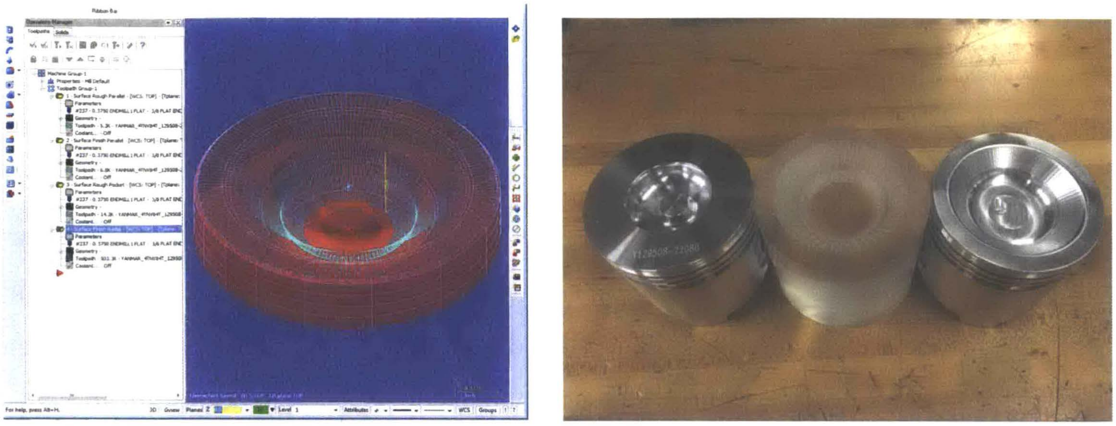

**(a)** **(b)**

**Figure 2-6.** Piston modification process. (a) Toolpaths generated in MasterCAM; (b) Original piston on the left, mock piston made from polycarbonate in the middle; final machined piston that was installed in the engine.

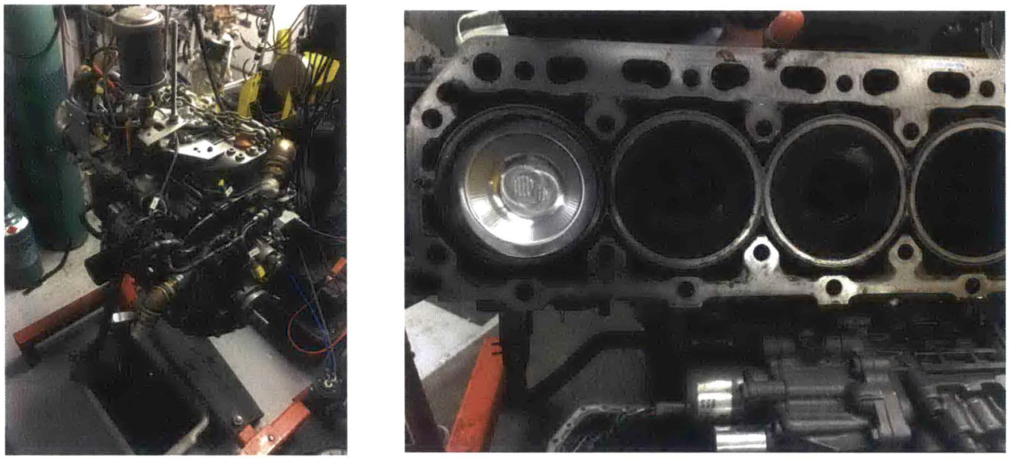

**(a)** **(b)**

**Figure 2-7.** Installation of modified piston in engine. (a) The engine was transferred to an engine stand to allow easy access to the big side of the connecting rod from the crankcase; (b) the modified piston (far left) after installation.

### 2.2.3. Spark-Ignition System

An off-the-shelf 1996 Dodge Caravan Mopar[2] ignition coil was used to generate spark-ignition in the test cylinder (Figure 2-8). An International Rectifier GB14C40L automotive ignition IGBT was used to provide the switching currents for the primary winding in the ignition coil (Figure 2-9). The switching square wave signal with appropriate phasing was generated by a dedicated computer which read engine speed and spark timing inputs from the controlling computer, and based on bottom-dead-center (BDC) timing and crank angle degree (CAD) timing signals from the phase alignment hardware described in Section 2.2.4, generated a square pulse in time with each spark with 1 CAD resolution. The IGBT was switched on for 4 ms in order to generate each spark, during which a Mean Well +12V 18A DC output power supply was shorted to the engine test bed. Upon opening the circuit at the end of each period, the magnetic field that was stored in the ignition coil secondary winding collapsed and generated the spark-ignition required to ignite the test cylinder mixtures.

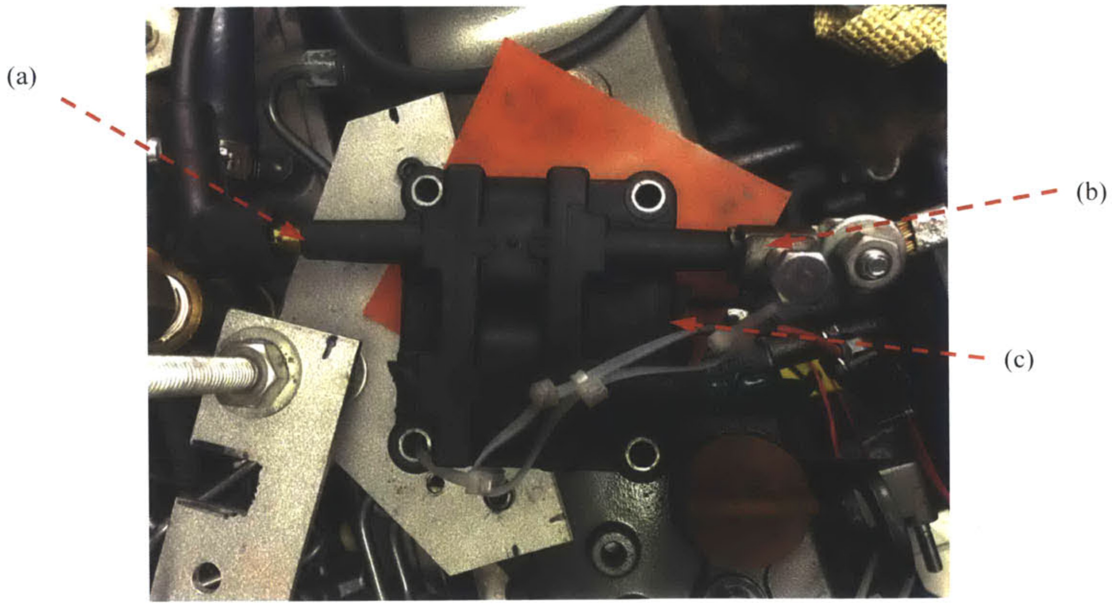

**Figure 2-8.** Four-cylinder ignition coil from Mopar. (a) Ignition source for test cylinder connected directly to spark plug; (b) ignition source for cylinder "4", which is on the opposite side as the test cylinder (it is grounded to maximize ignition power to the test cylinder); (c) high current switched supply to primary coil.

---

[2] OEM# 04609080

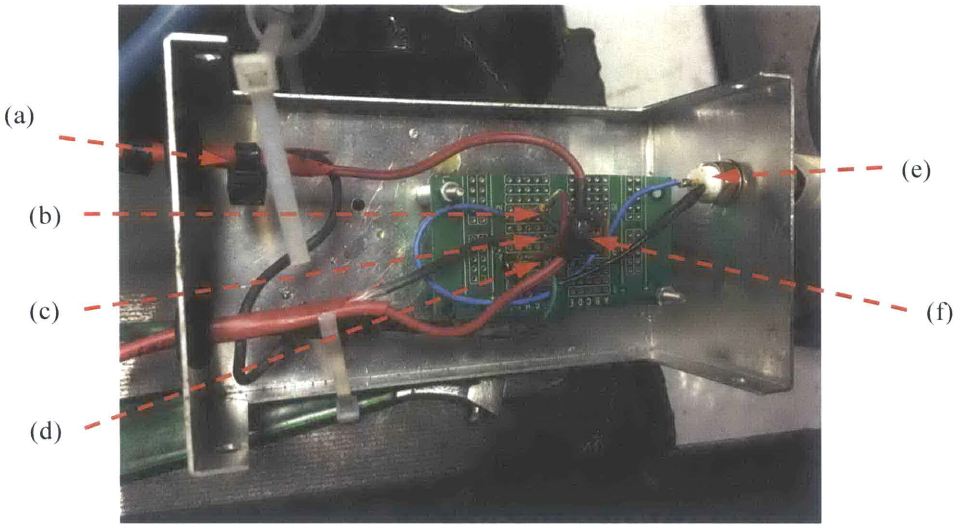

**Figure 2-9.** Ignition IGBT circuit. (a) 12V/18A DC power supply to input side of primary coil; (b) Gate, connected to triggering signal (e); (c) Collector, connected to output side of primary coil; (d) Emitter, connected to ground; (e) triggering signal; (f) IGBT chip.

### 2.2.4. Phase Alignment Hardware

Phase alignment between data acquisition equipment and the engine's position was necessary to time spark-ignition and collect data in phase with the compression stroke. This was only necessary on the spark-ignited engine as the catalytic engine did not have a spark plug or pressure sensor in the cylinder. An H25 incremental optical rotary encoder from BEI Sensors[3] was directly coupled to the engine crankshaft. This produced two out of phase square waves with 50% duty cycle and a cycle period of 1 CAD (the $A$ and $B$ signals), and one square wave with a peak width of 0.5 CAD and a cycle period of 360 CAD (the $Z$ signal) as shown in Figure 2-10. The $Z$ signal was timed to bottom-dead-center (BDC) piston position. Since there are two revolutions for every cycle in a four-stroke engine, and hence two times when the engine is at BDC in a cycle, only every other BDC is timed to the compression-stroke. A logic circuit was used to perform this phase selection. The rotary encoder was supplied with 12V power using a Mean Well 12V/0.84A DC power supply, and outputted single-ended 12V logic on its $A$, $\bar{A}$, $B$, $\bar{B}$, $Z$, $\bar{Z}$ signals. The $A$, $B$ and $Z$ signals were filtered by a BEI Sensors optical-isolator

---

[3] BEI Sensors H25 Incremental Optical Express Encoder: XH25E-F1-SS-360-ABZC-28V/V-SM18

electronic module[4] wired as a single ended line driver. The isolator can reduce some noise in the single-ended configuration, and it did not appear to be necessary to wire it as a differential line driver. Power to the isolator module was supplied by the same power source as the rotary encoder's. The optical-isolator received 12V logic from the encoder and outputted 5V logic. The isolated $B$ signal was transmitted directly to the data acquisition hardware downstream. The isolated $Z$ signal was first filtered by a Fairchild Semiconductor DM7474 positive-edge-triggered D-type flip-flop (truth table shown in Figure 2-5). Using the $Z$ signal as the clock signal (CLK) and the inverse output logic level ($\bar{Q}$) as the D input (D), the flip-flop switches the logic level ($Q$ and $\bar{Q}$) whenever a rising edge on the clock signal occurs. That way, a high signal is observed every revolution, and therefore every other BDC position. The phase selection can be made between $Q$ and $\bar{Q}$ as one will necessarily be timed to the compression stroke, while the other will occur at the exhaust stroke. Therefore, a single-pole double-throw (SPDT) switch was installed to select which signal to pass to an AND gate (described below). Since the correspondence between $Q$ or $\bar{Q}$ and the compression stroke depended on where in its cycle the engine and phase selection hardware were turned on, either of the signals could correspond to compression-stroke BDC. This correspondence could be confirmed by observing the pressure sensor signal on the main computer.

**Table 2-5.** The logic table for the DM7474 flip-flop.

| **Inputs** | | **Outputs** | |
|---|---|---|---|
| **CLK** | **D (= $\bar{Q}$)** | **$Q$** | **$\bar{Q}$** |
| Rising Edge | H | H | L |
| Rising Edge | L | L | H |
| L | Either H, L | $Q_0$ | $\bar{Q}_0$ |

H: HIGH logic level; L: LOW logic level;
$Q_0$, $\bar{Q}_0$: original output logic levels before input conditions were changed.

Both flip-flop and AND gate were powered by the same Globtek 5VDC 1A power supply. The $Q$ or $\bar{Q}$ signal, whichever one was selected, was filtered by a Texas

---

[4] BEI Sensors Optical-Isolator Electronic Module EM-DR1-IC-5-TB-24V/5

Instruments SN74LS08N quadruple positive-AND gate. First, the isolated $Z$ signal was compared with 5V $V_{cc}$ as provided by the power supply. This regulated the $Z$ signal logic level to 5V. Then, the $Q$ or $\bar{Q}$ signal was compared with the filtered $Z$ signal to deselect every other $Z$ pulse. This produced the compression-stroke BDC signal. Finally, this signal was compared with 5V $V_{cc}$ to regulate its voltage level, and the output signal $(BDC_{compr})$ was transmitted to the data acquisition system.

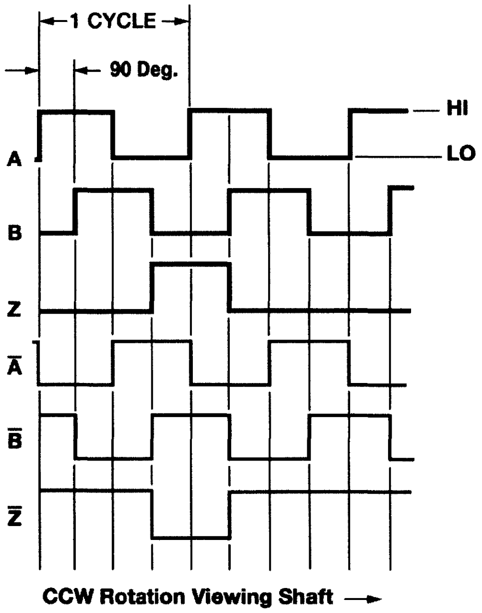

**Figure 2-10.** Phasing of H25 incremental optical rotary encoder $A$, $\bar{A}$, $B$, $\bar{B}$, $Z$, $\bar{Z}$ signals [49].

### 2.2.5. Exhaust Soot Concentration Measurement System

Engine exhaust soot concentrations from the spark-ignited engine were measured using a gravimetric soot detection apparatus (Figure 2-11). Engine exhaust was drawn through a heated stainless steel tube by a Gast 1423 rotary vane vacuum pump. The exhaust gas samples were passed through dried Pall LifeSciences PALLFLEX 47 mm Tissuquartz™ (2500 QAT-UP) membrane filters, which were held in place by a Gelman Sciences 2220 filter holder. Water vapor was condensed from the gas by cooling it to room temperature through a counter flow heat exchanger using city water. A constant volumetric flow rate was maintained during sampling $(\dot{V}_{sample})$, as measured by an Omega FVL-1611A volumetric flow meter calibrated to room air, and the time of sampling was measured

($\Delta t_{sample}$) in order to calculate the total sample volume, which was the product of the two. A small error will exist in the volume flow rate measurement due to the discrepancy between true and actual viscosity of the exhaust gas going through the meter at different operating points, since the measurement device expected atmospheric air. However, since the majority of the gas is $N_2$ (~ 70% in the exhaust mixtures), its viscosity should not have deviated significantly from that of air. Each filter paper was processed in a dehumidifier for at least 24 hours prior to testing. After soot samples were collected, the specimens were dried again in the same dehumidifier for at least 24 hours before being weighed again. The difference between initial ($m_{s,i}$) and final ($m_{s,f}$) mass of each filter paper specimen was taken to determine the soot collected in that test. The collected soot mass divided by the total volume flow provided the soot concentration $c_s = \frac{m_{s,f}-m_{s,i}}{\dot{V}_{sample}\Delta t_{sample}}$.

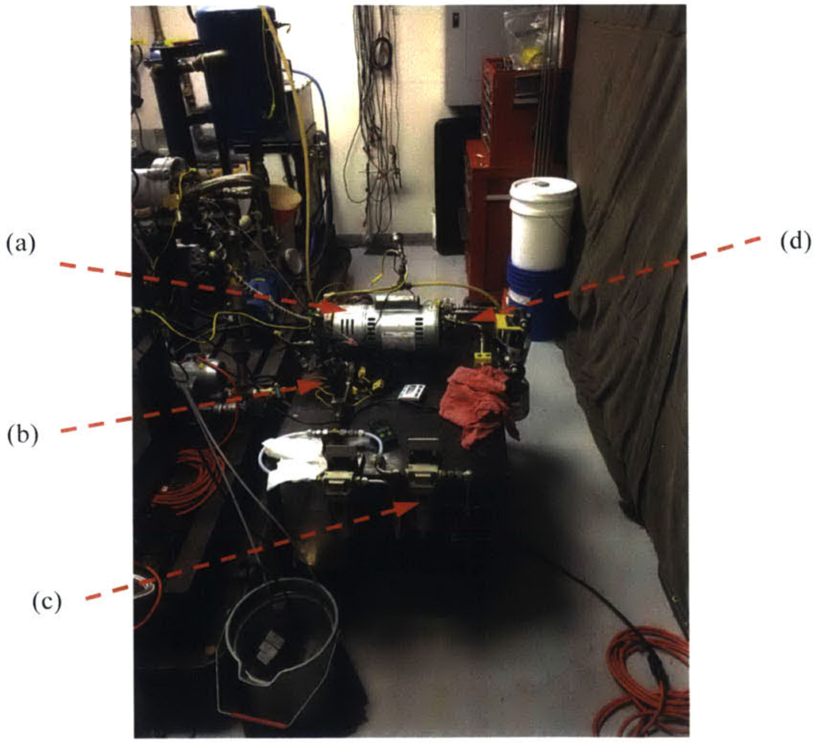

**Figure 2-11.** Soot detection apparatus [50]. (a) Gast vacuum pump; (b) Volumetric flow meter; (c) Condensate collection chamber; (d) Pall filter holder.

## 2.3. Catalytic Engine Setup

Experiments for catalytic partial oxidation were performed in a Lister-Petter TR1 single-cylinder diesel engine generator. The starter and battery were not used in this configuration, as the engine was driven by a motor with a variable frequency drive (VFD). The intake and exhaust manifolds were both on the same side of the engine (Figure 2-12). This made it more convenient for plumbing. One Omega ungrounded low noise HG K-type thermocouple with a stainless steel sheath, 1/16" outer diameter, and 12" length was used to measure temperature in each of the two manifolds. An Omega 0-50 PSIA 0-5 VDC PX309 and 0-30 PSIA 0-5 VDC PX309 pressure transducer were used to measure pressure in the intake and exhaust manifolds respectively. In anticipation of performing tests with higher intake boost pressures in the future, the operating range of the transducer in the intake was chosen to be larger.

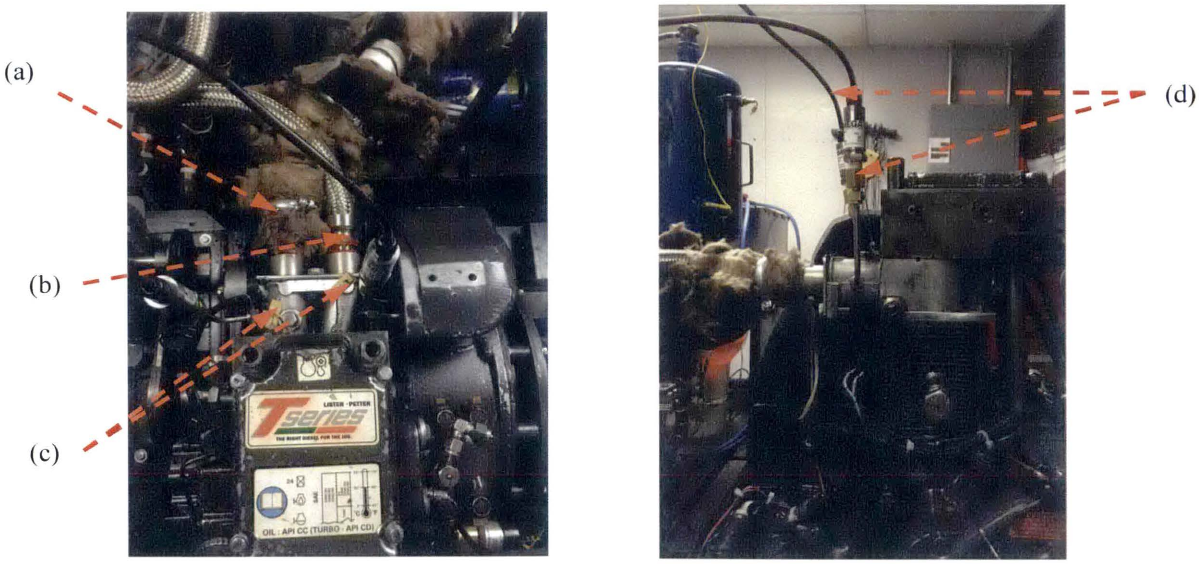

**Figure 2-12.** The intake and exhaust manifolds of the catalytic engine. (a) Intake manifold; (b) exhaust manifold; (c) thermocouples; (d) pressure transducers.

### 2.3.1. Foam-Containing Piston

A palladium catalyst on an alumina support was deposited by washcoating on Fecralloy foams in the Catalysis for Sustainable Environment Group led by Professor Robert Farrauto, at Columbia University. A retaining ring groove in the piston bowl of an original Lister-Petter TR1 piston was machined using a 1/16” wide face, ¼” cutter diameter American Standard #202 high-speed steel keyseat cutter as shown in Figure 2-13a. A black-finish steel internal retaining ring for 1-15/16” bore diameter was used to hold the catalytic foam inside the piston bowl as shown in Figure 2-13b. Retaining ring pliers were used to install the ring above the catalytic foam.


(a) (b)

**Figure 2-13.** The catalytic engine piston. (a) The original unfilled piston bowl; (b) The piston bowl with catalytic foam and retaining ring.

### 2.3.2. Catalytic Foam

The catalyst was composed of palladium (Pd) that was washcoat deposited on a Fecralloy metallic foam disk. Pd loading in the washcoat was 1% by mass, and the total weight of the washcoat was 0.3407 g. The original foam disk had a mass of 8.7114 g. The washcoat loading on the disk was 3.76 wt%, resulting in a final catalytic foam mass of 9.0521 g. The catalytic foam was prepared by the Catalysis for a Sustainable Environment group led by Professor Robert Farrauto at Columbia University in the City of New York. Other metals were attempted but did not result in good adherence to the metallic foam.

### 2.3.3. Engine Speed Control

The engine was driven by a VFD-regulated 7.5 hp three-phase AC induction motor running at 750 rpm. This speed was chosen as a mid point between lower speeds where the engine oil would not have been supplied at high enough rates, and higher speeds that would reduce the residence time of the charge in the cylinder, and hence reduce conversion efficiency. The VFD was a DURAPULSE 7.5 hp 230 V three-phase variable frequency AC drive from Automation Direct (Figure 2-14a) with the parameters shown in Table 2-6. The drive system was supplied with three-phase 208 VAC.

**Table 2-6.** AC induction motor rated parameters.

| Parameter: | Setpoint: |
|---|---|
| **Motor Nameplate Voltage** | 208 V |
| **Motor Nameplate Current** | 21.4 A |
| **Motor Base Frequency** | 60 Hz |
| **Motor Base RPM** | 1770 rpm |
| **Motor Maximum RPM** | 3565 rpm |

An LR-27P5 three-phase line reactor was installed on the output side of the VFD. This protected the VFD from short circuits at the load, and reduced motor overheating [51]. A Marathon Electric three-phase inverter duty 230/460 VAC 7.5 hp fan-cooled AC induction motor with 1770 nameplate RPM, was used to drive the crank shaft, which was coupled to the induction motor with a belt-and-pulley system (Figure 2-14b). A GoodYear Poly-V 360J six-band V belt was used to couple a 4.5” diameter quick-disconnect bushing-bore V-belt pulley that was keyed to the motor shaft, to a 6” pulley of the same type that was keyed to the engine crankshaft. From the ratio in pulley diameters, the speed of the engine crankshaft was $\frac{4.5}{6}$ times the speed set on the VFD, or 563 rpm.

(a) (b)

**Figure 2-14.** The drive mechanism for the Lister-Petter TR1 diesel engine. (a) DURAPULSE 7.5 hp 230 VAC three-phase variable frequency AC drive from Automation Direct; (b) Marathon Electric three-phase inverter duty 230 VAC 7.5 hp fan-cooled AC induction motor with belt and pulleys.

## 2.4. Shared Systems

Both engines shared the same data collection hardware and processing software, intake composition and heating systems, and exhaust sampling instruments.

### 2.4.1. Intake Composition Control System

**Table 2-7.** Airgas part numbers for the gases used in experimentation.

| Compound | Airgas Part Number |
|---|---|
| $CH_4$ | ME CP300 |
| $H_2$ | HY 300 |
| $C_2H_6$ | ET CP200 |
| $CO_2$ | CD R300 |
| $N_2$ | NI 300 |

The charge composition for each engine was calculated based on the formulas explained in Section 2.1. The flow rate required for each gas was communicated to dedicated, gas-specific mass flow controllers using LabVIEW. Table 2-7 shows the gases that were shared between the two engines. Note that the compositions tested in the two engines were not the same. For example, $CO_2$ was used in the catalytic engine, though not in the spark-ignited one. Compressed air was provided from an Atlas Copco GA30FF oil-injected rotary screw compressor set to 100 PSIG, and regulated to 40 PSIG. The air compressor provided oil particle filtering and drying, ensuring clean, moisture-free air was provided to the engine.

Test cylinder intake compositions and flow rates were controlled by four Omega FMA-2600A series mass flow controllers and one Cole-Parmer EW-32907-69, with one controller per gas type. $CH_4$, $C_2H_6$, $H_2$ and $CO_2$ were mixed separately from air, and passed through a buffering chamber downstream of their respective mass flow controllers in order to reduce the effect of pressure fluctuations in the intake manifold on the controller valves. Note that the spark-ignited test cylinder used $CH_4$, $H_2$, $C_2H_6$ and air, while the catalytic test cylinder used $CH_4$, $CO_2$ and air. The maximum flow rates (used to normalize each flow rate setpoint to the extent of valve open/close in the controller mechanism) are shown for each flow controller in Table 2-8. Since the intake mass flow controller system was shared between the two engines, two diverting 3-port bronze ball valves with 3/8" NPT female port fittings were used to divert intake gases to the engine being used as shown in the plumbing diagram in Figure 2-15.

A Granzow ½" NPT 8W 110-120 VAC 50-60 Hz solenoid valve was used to supply compressed $N_2$ gas from a bottle to provide positive pressure to the intake manifold during startup of either engine. The $N_2$ supply was plumbed into the same line as compressed air before entering the air intake heaters as shown in the schematic in Figure 2-15.

**Table 2-8.** Mass flow controller maximum flow rates were selected based on expected operating ranges for each gas.

| Gas | Flow Controller Maximum Flow Rate (SLPM) |
|---|---|
| Air | 250 |
| $CH_4$ | 100 |
| $H_2$ | 50 |
| $C_2H_6$ | 5 |
| $CO_2$ | 50 |

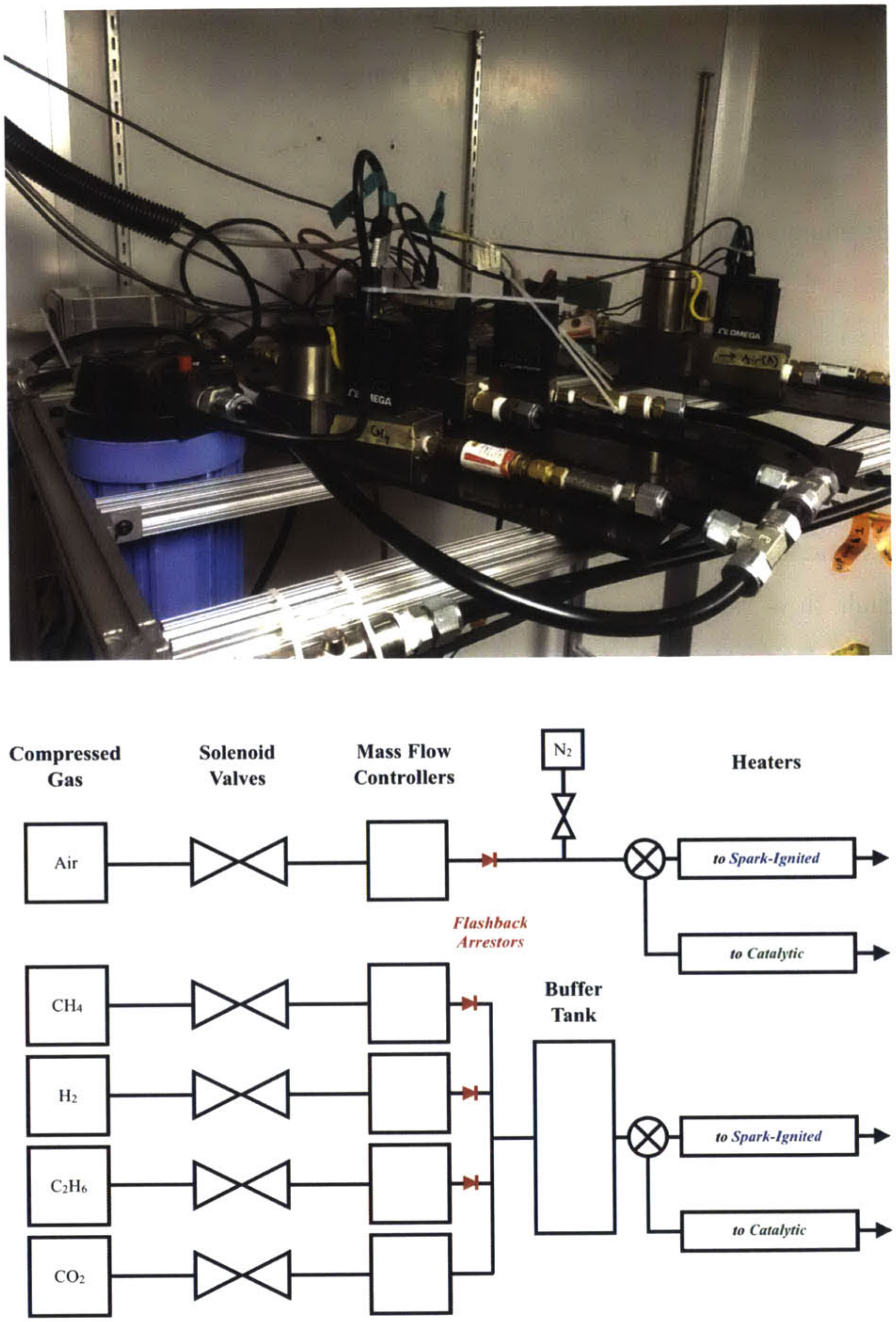

**Figure 2-15.** Mass flow controller intake mixture composition control system.

### 2.4.2. Intake Heating System

Two Omega AHPF-122 1200W air process heaters and an AHPF-082 600W air process heater were used to heat air and other gases ($CH_4$, $H_2$, $C_2H_6$) respectively for the spark-ignited test engine (Figure 2-16). Two air heaters were required since the power requirement for air was much larger than that of the other gases. Two 624W 240VAC 8’ extreme-temperature heat cables were used to keep the gases heated as they travelled through stainless steel tubing and braided metal hose to the intake manifold of the spark-ignited engine. An Omega AHPF-102 1000W and an AHPF-082 600W air process heater were used to heat air and other gases ($CH_4$ and $CO_2$) respectively for the catalytic test engine (Figure 2-17). One 468W 240VAC 6’ extreme-temperature heat cable was used to apply heat to the gases after the process heaters. All heaters were controlled by two Omega CN7800 heater controllers and two Omega SSRL240AC25 solid-state relays, one for the air heaters, and one for the heat cables and process heaters for the remaining gases. Two double-pole double-throw On-On 50A toggle switches, one corresponding to the output of each solid-state relay, were used to direct current to the heating system being used. The gas temperatures were constantly monitored by K-type air/immersion thermocouples with type 316 stainless steel probes with 1/8” diameter and 12” length, measured at the outlet of the process heaters. In both setups, the gases were mixed in a 1” NPT pipe wye containing porous copper foam, which served to induce turbulence and promote mixing. Rigid Very-High-Temperature Mineral Wool Pipe Insulation was used to insulate the (cylindrical) process heaters, while Very High-Temperature Fiberglass Insulation Sheeting was used to insulate the parts of the setup that did not have constant diameter. The insulation material was purchased from McMaster-Carr.

**Figure 2-16.** Gas process heaters and mineral wool insulation for spark-ignited engine cylinder. (a) air heater; (b) $CH_4 + H_2 + C_2H_6$ heater; (c) heat cable for mixed gas.

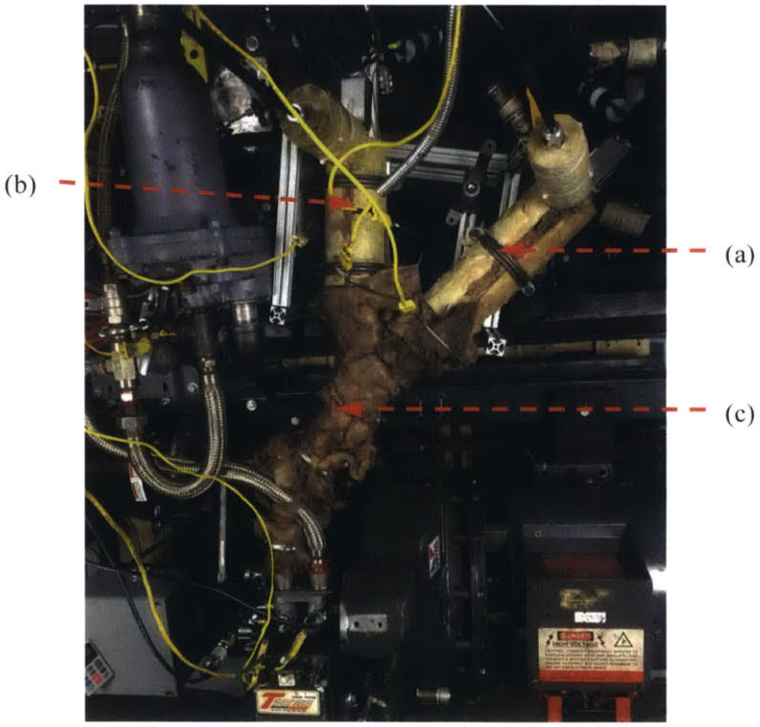

**Figure 2-17.** Gas process heaters and mineral wool insulation for catalytic engine cylinder. (a) air heater; (b) $CH_4 + CO_2$ heater; (c) heat cable for mixed gas.

### 2.4.3. Data-Acquisition System

A National Instruments NI 9205 Analog Input Module and NI 9213 Thermocouple Input Module were used to collect analog and thermocouple data respectively. The NI 9205 was used to read cylinder, intake and exhaust manifold pressures, as well as engine speed from the dynamometer. The NI 9213 was used to read intake and exhaust manifold temperatures, as well as heater outlet, syngas burner, engine coolant, and exhaust stack temperatures. A National Instruments NI cDAQ-9188 Ethernet chassis merged all measurement data from the modules and collected B and $BDC_{compr}$ signals from the phase alignment circuitry in order to synchronize data collection for the spark-ignited engine. These phasing signals were not used to collect data for the catalytic engine.

Data from the Ethernet chassis were collected, visualized and saved by custom-built LabVIEW VIs (Figure 2-18). Each engine had a separate main VI, as the spark-ignited engine had significantly more controls and outputs due to its use of a larger number of gases, and its need for phase alignment for in-cylinder pressure data. The basic structure of the main VI of each engine was similar. It used a while-loop-enclosed case structure to select between "Display" and "Save" data states (the "main while loop"). In the "Display" state, two while loops were used to perform DAQmx read on pressure and temperature data respectively. For the spark-ignited engine, pressure data were read and displayed at a rate of 1 data point per CAD, while temperature data were read and displayed at a rate of 10 Hz (averaged to 5 Hz). For the catalytic engine, pressure and temperature data were both read at 10 Hz (averaged to 5 Hz). In this case, there was no need to synchronize to CAD timing as the catalytic engine did not have cylinder pressure measurement. Intake temperature data read from these while loops were used for $T_i$ in calculating the mass flow controller flow rates. In the "Save" state of the spark-ignited engine, a sequence structure was used to perform read and save functions in three steps that were performed for 200 engine cycles in each step (each combined data set is a "datapoint"):

1) CAD Timing: Read and write analog data from the NI 9205 to a binary file every CAD pulse.

2) 80 kHz: Read and write analog data from the NI 9205 to the same binary file at 80 kHz. While these data were saved for each operating setpoint, variables that were calculated from them did not deviate much from those calculated from CAD-timed data. Since the sampling frequency was significantly higher in this case, processing times were longer. Therefore, this data was not used in calculations for this work.

3) Temperature: Read and write temperature data from the NI 9213 to the same binary file at 1 kHz.

In the "Save" state of the catalytic engine, a two-step sequence structure was used as the engine timing signals were not necessary. Each step was also performed for 200 engine cycles (each combined data set is a "datapoint"):

1) 1 kHz pressure: Read and write analog data from the NI 9205 to a binary file at 1 kHz.

2) 1 kHz temperature: Read and write temperature data from the NI 9213 to a binary file at 1 kHz.

**Table 2-9.** "Display" and "Save" frequencies for data from each of the two test engines.

| **Engine:** | **"Display" Frequency** | | **"Save" Frequency** | | |
|---|---|---|---|---|---|
| | **Pressure** | **Temperature** | **Pressure** | | **Temperature** |
| *Spark-Ignited* | per CAD | 10 Hz (averaged to 5 Hz) | per CAD | 80 kHz | 1 kHz |
| *Catalytic* | 10 Hz (averaged to 5 Hz) | 10 Hz (averaged to 5 Hz) | per CAD | - | 1 kHz |

The Display/Save while loop also contained the input control variables for intake composition and mass flow rate. In the VI controlling the spark-ignited engine, this included $p_i$, a tuning factor which was used to set the mass flow rate to achieve an actual intake pressure of ~1 bar as measured in the intake manifold, engine speed $N$, $\phi_M$, $x_{H_2}$

and $x_{C_2H_6}$. For the catalytic engine, this included $p_i$, $N$, $\phi_M$, $y_{DR}$, and $n_{CO_2}$. Property nodes for each variable were created to communicate with a separate while-loop-enclosed case structure (the "MFC Write while loop"), which housed a Sub-VI that performed the composition and flow rate calculations and communicated with all mass flow controllers. Since the calculations for each engine were slightly different, the algorithm in the Sub-VI depended on which engine was being run. A logic statement in the main while loop selected whether to update the values on the MFCs (an "Update MFCs" case) or to stop the MFCs (a "STOP MFCs" case). A separate while-loop-enclosed case structure (the "MFC Read while loop") was used to read the values of each MFC's operating parameters (gas pressure, temperature, volume flow rate, actual standard volume flow rate, and desired standard volume flow rate) and display them on the front panel, allowing the operator to confirm that setpoints were being reached on the mass flow controllers and therefore that composition setpoints were being met. The MFC Read while loop was triggered at 1 Hz frequency from the main while loop when the MFCs were not being updated.

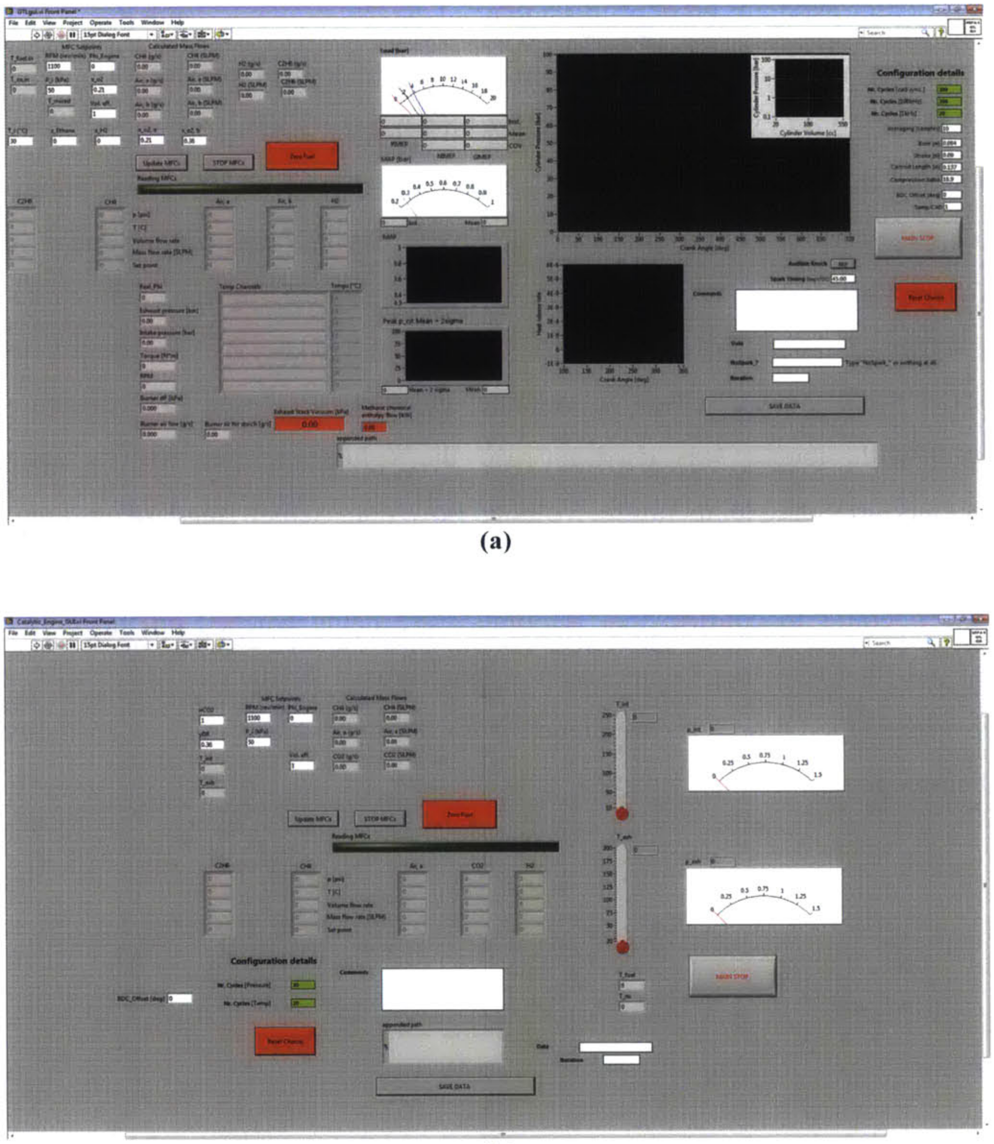

(a)

(b)

**Figure 2-18.** LabVIEW VI front panels for (a) spark-ignited test cylinder, and (b) catalytic engine.

### 2.4.4. Gas Chromatography (GC)

The GC sampling system was placed downstream of both engine exhaust manifolds to measure exhaust composition from one engine at a time. To share the sampling system, a diverting 3-port type 316 stainless steel ball valve with ¼" NPT female port fittings was used to select which engine exhaust to sample. A ¼" stainless steel sample tube connected the exhaust pipe of the spark-ignited engine to one of the input ports of the ball valve, and a ¼" NPT braided stainless steel hose was used to connect the exhaust manifold of the catalytic engine to the other input port of this ball valve. The exhaust gases being sampled were cooled by a water jacket at 0 °C to remove water vapor. The jacket temperature was maintained by pumping liquid water from an ice-water slurry through a counter-flow heat exchanger using a Model NK-1 115 VAC 60 Hz 1.1 A single-phase submersible water pump. Condensate was gravity-collected in a stainless steel chamber that had a one-way ball valve to allow drainage from its base. The chamber was occasionally drained to prevent liquid water from traveling further downstream. Following the chamber, a three-way ball valve was used to select between calibration gas or engine exhaust to be transmitted to the GC for sampling. The transmitted gas then passed through a Tee where most of the gas was allowed to flow to the exhaust stack, while a small quantity was drawn by a vacuum pump through a line towards the GC (the "GC sampling line"). The sampled gas was drawn at 0.2 SCFH by a KNF Neuberger UN726FTP diaphragm vacuum pump. It was filtered for particulate matter by a Parker 9900-05-BK Balston oil-removal miniature air filter with ¼" inlet/outlet OD and 3.5 maximum SCFM (at 100 psi), and subsequently dried further by Drierite 10-20 mesh anhydrous indicating desiccant. Due to heavy soot production in some tests, the air filters were occasionally changed to allow a consistent volume flow rate through the GC sample line. The gas was passed through a second Tee to allow excess gas to flow to the exhaust, and the GC sampled directly from this line.

The sample gas was analyzed in an Agilent 490 Micro GC using settings described in Table 2-10. These settings were specific to these experiments and are not necessarily applicable when sampling gases with other compositions. Most importantly, they provided the MS5A column enough run time to read CO, which appears late in a sample run, while flushing the column in time to avoid $CO_2$ adsorption. The gases used for calibration are described in Table 2-11. GC data were collected using Agilent OpenLAB software and processed in MATLAB. The voltage outputs of the TCD detector were integrated where each gas appeared. These positions in time were observed to be constant for each gas throughout all runs, and are shown in Table 2-12. Using MATLAB, trapezoidal numerical integration was performed for each gas peak with respect to a common baseline among all of the gases, which was found to be the average voltage from

140 to 145 seconds in the sample. These baseline values were approximately constant for all gases that were of interest. A example of the calibration constants used for spark-ignited engine results are shown in Table 2-13. These values changed slightly over time, though typically only over several percentage points.

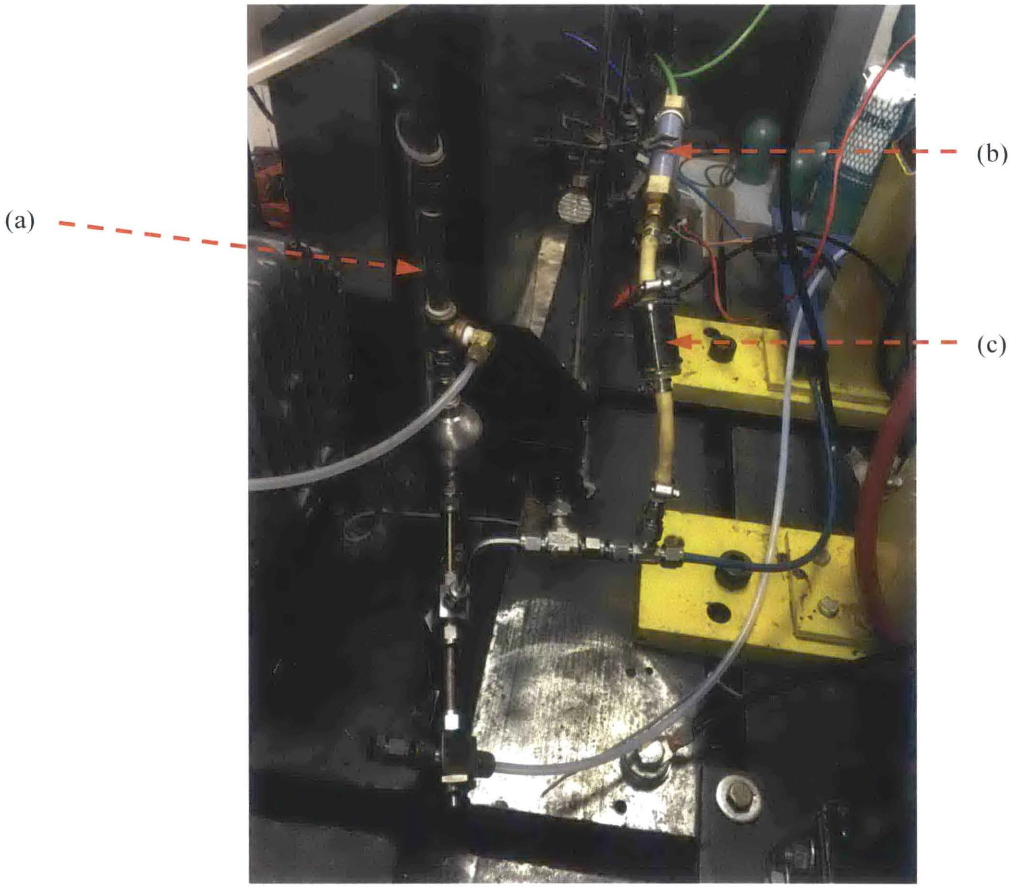

**Figure 2-19.** The GC sample line with (a) water vapor heat exchanger, (b) desiccant, and (c) particle and oil filter.

**Table 2-10.** Two columns were used in the Agilent 490 Micro GC with a thermal conductivity detector. The MS5A was used to detect $H_2$, $O_2$, $N_2$, $CH_4$, CO. The PPU was used to detect $CO_2$ and $C_2H_6$. Each column was operated under slightly different conditions to suit target gas detection and run times.

| | **Column Type** | |
|---|---|---|
| | *CP-Molsieve 5A (MS5A)* | *PoraPLOT U (PPU)* |
| **Carrier Gas** | Argon | Helium |
| **Injector Temperature (°C)** | 110 | |
| **Injection Time (ms)** | 40 | |
| **Backflush Time (s)** | 11 | n/a |
| **Column Temperature (°C)** | 80 | 50 |
| **Initial Pressure (kPa)** | 150 | |
| **Sampling Frequency (Hz)** | 100 | |
| **Run Time (s)** | 150 | |
| **Stabilizing Time (s)** | 5 | |
| **Sample Time (s)** | 90 | |
| **Sample Line Temperature (°C)** | 37 | |

**Table 2-11.** The composition of the calibration gases that were used. Bold indicates this composition was used for calibration.

| *Gas* | *Airgas Part Number* | *Composition* | |
|---|---|---|---|
| 1 | X02NI80C3003240 | **20% $CO_2$** | **80% $N_2$** |
| 2 | X02NI60A3003006 | **40% $H_2$** | 60% $N_2$ |
| 3 | AI D300 | **21% $O_2$** | 79% $N_2$ |
| 4 | X02AR95D3002178 | **5% $CH_4$** | 95% Ar |
| 5 | X02NI90P3004544 | **10% CO** | 90% $N_2$ |
| 6 | X02AR85C2002058 | **15% $C_2H_6$** | 85% Ar |

**Table 2-12.** The peak integration start and end times for each gas, and the corresponding GC column from which they were found.

| Gas | Column | Start Time (min) | End Time (min) |
|---|---|---|---|
| $H_2$ | MS5A | 24 | 30 |
| $O_2$ | MS5A | 34 | 40 |
| $N_2$ | MS5A | 50 | 60 |
| $CH_4$ | MS5A | 67 | 86 |
| CO | MS5A | 116 | 140 |
| $CO_2$ | PPU | 56 | 66 |
| $C_2H_6$ | PPU | 70 | 84 |

**Table 2-13.** The calibration mole fractions and approximate calibration constants for each gas used.

| **Gas** | **Mole Fraction** | **Calibration Constant ($\frac{\bar{x}_i}{Area}$)** |
|---|---|---|
| $H_2$ | 0.4 | 0.00048 |
| $O_2$ | 0.21 | 0.0038 |
| $N_2$ | 0.8 | 0.0051 |
| $CH_4$ | 0.05 | 0.0021 |
| CO | 0.1 | 0.0052 |
| $CO_2$ | 0.2 | 0.00054 |
| $C_2H_6$ | 0.15 | 0.00057 |

### 2.4.5. Data Processing Software

Both LabVIEW and GC data were processed in MATLAB subsequent to data collection. The code used for this is shown in Appendix C. Each LabVIEW datapoint consisted of 200 consecutive engine cycles of pressure and temperature data, as well as testing notes on the engine operating conditions. Data from the spark-ignited engine were synchronized to $BDC_{compr}$, while those from the catalytic engine were not as it did not require accurate timing to synchronize cylinder pressure data. For the spark-ignited engine, phasing alignment was performed during data collection, however, misalignment between the crankshaft position and the Z signal on the rotary encoder could lead to error in some cases, so this was confirmed using engine compression traces with the ignition off ("motoring traces"). Alignment was critical as a 1 CAD offset could lead to a significant difference in calculated engine performance due to out-of-phase spark timing. Close alignment was confirmed to ensure these errors were not present in the data shown here.

The LabVIEW binary data were first imported in MATLAB. Intake and exhaust manifold pressure and temperature data for both engines were averaged over the 200 engine cycles that were collected for each data point. The cylinder pressure data that were collected for the spark-ignited engine were referenced to the intake pressure as measured in the intake manifold. The average pressure during the last 10 CAD of the cycle (the last 10 CAD of the intake stroke prior to BDC) was subtracted from the pressure data in the pressure trace. Then, the average manifold absolute pressure (MAP) during the same 10 CAD was added to provide an absolute reference pressure. This process is called "pegging".

Referencing to the MAP at $BDC_{compr}$ was found to be the most accurate way to "peg" piezoelectric pressure sensors [52]. These sensors generate a charge that is proportional to changes in pressure to a high degree of accuracy. However, they must still be referenced to an accurately measured absolute pressure.

Work output values were calculated from the spark-ignited engine's cylinder pressure data using $p\,dV$ integration. The cylinder volume ($V$) with respect to CAD ($\theta$) was calculated using the engine's basic geometric properties (clearance volume $V_c$, the ratio between connecting rod length and crank radius $R = \frac{l}{a}$, and compression ratio $r_c$) and is shown in Eq. 42.

$$V = V_c\left\{1 + \tfrac{1}{2}(r_c - 1)\left[R + 1 - \cos\theta - \sqrt{R^2 - \sin^2\theta}\right]\right\} \tag{42}$$

The differential change in volume ($dV$) was calculated by taking the difference between the volume at each value of $\theta$, $dV_i = V_i - V_{i-1}$. Note that in cases where the cylinder volume is decreasing, the value of $dV$ is negative. The total indicated work output per cycle ($W_{c,i}$) was calculated discretely by taking the summation of the product of $p$ and $dV$, or $W_{c,i} = \sum_\theta p[\theta]dV[\theta]$. The indicated mean effective pressure ($imep$) was taken as $W_{c,i}$ divided by the engine displacement volume ($V_d$), which was constant. This is shown in Eq. 43. The net indicated mean effective pressure (NIMEP) was taken to be the value of $imep$ from $\theta = 0$ to 720° (the full engine cycle including compression, expansion, exhaust, intake strokes). The gross indicated mean effective pressure (GIMEP) was taken to be the value of $imep$ from $\theta = 0$ to 360° (the compression and expansion strokes only). $\theta = 0°$ corresponds to $BDC_{compr}$. Once again, these calculations were not possible for the catalytic engine as a cylinder pressure sensor was not installed.

$$imep = \frac{W_{c,i}}{V_d} = \frac{\sum_\theta p[\theta]dV[\theta]}{V_d} \tag{43}$$

The coefficient of variation ($COV$) of NIMEP was calculated to show the variability of engine work output across a certain number of engine cycles. Data were collected on

LabVIEW in 200 cycle increments, therefore each value of COV that was calculated and shown in later sections corresponds to 200 consecutive engine cycles. The $COV$ of NIMEP ($COV_{nimep}$) was calculated using Eq. 44, where $\sigma_{nimep}$ and $nimep_{mean}$ are the standard deviation and mean of NIMEP across 200 consecutive engine cycles, respectively.

$$COV_{nimep} = \left[\frac{\sigma_{nimep}}{nimep_{mean}}\right]_{200\ cycles} \tag{44}$$

The GC data from both engines were processed in the same way. Calibration constants were typically generated on the day of an engine test, but values did not change significantly over time. The voltage outputs of the TCD were integrated for each GC sample to determine the area generated by each gas at that time. Again, these integration bounds were constant for all GC data collected and are shown in Table 2-12. The mole fraction of each species was assumed to be linear with respect to its peak area with a factor equal to the calibration constant calculated from GC calibration. The constants used for calibration depended on the expected dry mole fraction of the gas in the exhaust, and whether the calibration constant varied significantly for different calibration mole fractions. The conversion efficiencies between intake and exhaust were calculated using the mole fractions determined from the GC data.

### 2.4.6. Exhaust Gas Plumbing

The same syngas after-treatment system was used for both engines. However, the exhaust gases were plumbed to only allow one of the two engines to transmit gases to the after-treatment system at a time, since both engines were never run simultaneously. Two ¾" NPT type 316 stainless steel ball valves with lever handles and restricted flow were used to perform this flow selection (Figure 2-20). In addition to selecting which engine to exhaust, these valves also prevented the exhaust gases of one engine to blow back into that of another. This was done out of caution.

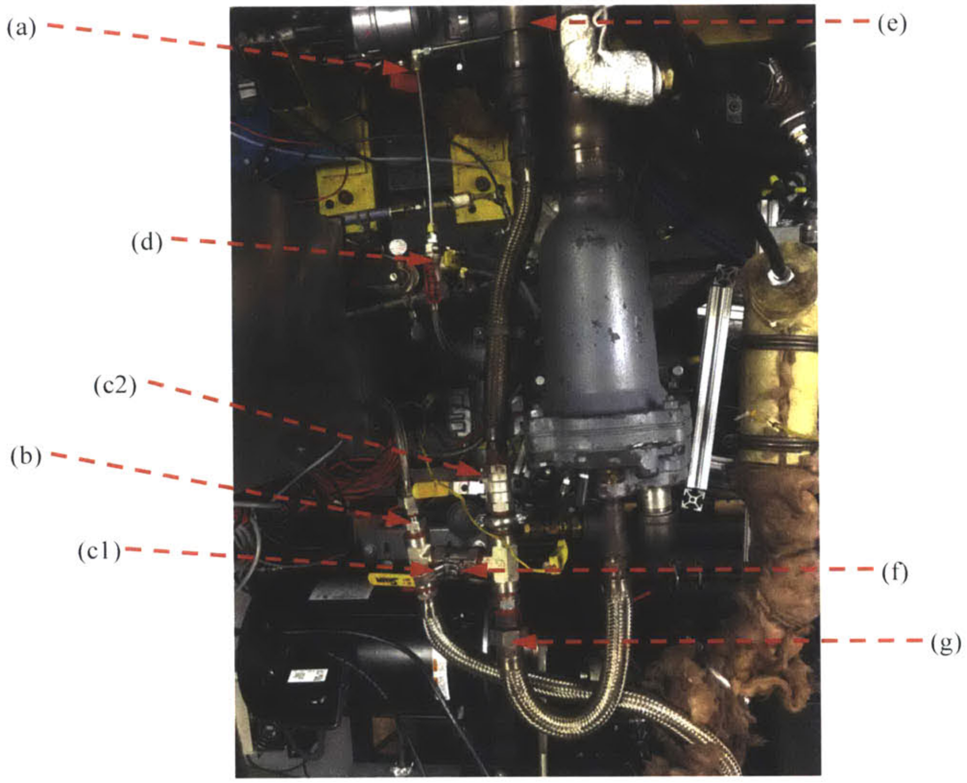

**Figure 2-20.** Shared exhaust gas plumbing. The system of valves allowed the exhaust manifolds of both engines to be segregated. This prevented hot gases from one engine from blowing back into the other. (a) GC sample gases from the spark-ignited test cylinder; (b) GC sample gases from the catalytic engine; (c1,c2) one-way ball valves to perform flow selection; (d) GC sample gas selection valve; (e) engine exhaust from the spark-ignited test cylinder; (f) engine exhaust from the catalytic engine; (g) common exhaust line. Ex. When using the catalytic engine, (c1) is open and (c2) is closed.

### 2.4.7. Syngas After-Treatment

As both engines were run in low-oxygen environments to perform partial oxidation, the exhaust gases contained large amounts of $H_2$ and CO. These gases are highly flammable and toxic. Therefore, combustion of these constituents was performed to completion in an exhaust gas burner to ensure the safety of the gases that were being transmitted to the atmosphere through the exhaust stack, and to comply with safety regulations on CO release. The exhaust gases were combusted in a Fives North American "Aardvark" high velocity burner. A Gast Regenair R2103 regenerative blower supplied air to the burner. An Autolite 3163 spark plug provided the ignition source.

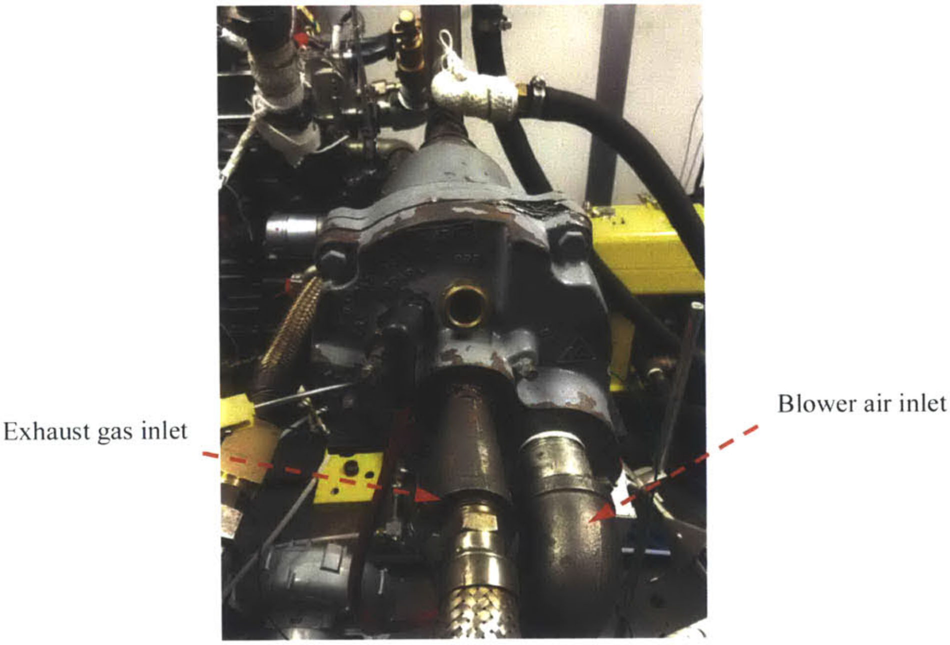

**Figure 2-21.** The Fives North American "Aardvark" high velocity burner.

## 2.5. Operating Procedures

Both engines were operated in a similar fashion. As higher intake temperatures were beneficial, both engines were run with room temperature intake charge at first to provide stable running conditions. Then, intake heating was used to raise temperatures to the desired range where a desired effect in engine operation was achieved. Here, both LabVIEW and GC data collection were performed, before moving the engine to the next operating point. This was repeated until all desired conditions were met and data were collected, before the engines were shut down.

### 2.5.1. Spark-Ignited Engine

When data was to be collected on a given day, the GC was first calibrated to the gases shown in Table 2-11. The engine coolant was always maintained at 95 °C to optimize clearances inside the engine. The coolant was heated to approximately 85 °C using the immersion heater described in Section 2.2.1. This often took two hours as 50% of the coolant was water, which has a high specific heat capacity. The remaining 10 °C were achieved during startup from diesel combustion.

To start the engine up, first, the Woodward diesel supply solenoid on the engine was switched on. The diesel cylinders were then started by a Denso starter. A 13.8 VDC enable signal was supplied from a Tripp-Lite PR-30 DC power supply to the starter solenoid, which allowed starting power to flow from a Duralast marine battery 29DP-DL, with 106 Amp Hours capacity, to the starter. The same DC power supply was used to actuate the diesel supply solenoid. Since the engine governor was mechanically controlled, no additional controls were required to regulate fuel supply to the engine. $N_2$ was supplied to the test cylinder during this time from the bypass line. A bypass gas was necessary as the test cylinder was being motored by the three diesel cylinders during startup, and providing a gas would prevent the engine from drawing a vacuum on the mass flow controllers. The ignition coil signals were supplied at this time, and spark-ignition was started without any combustible charge from the mass flow controllers yet.

Air was then supplied from the mass flow controllers, and the $N_2$ bypass was turned off. As the intake was still at room temperature, the engine was operated at close to stoichiometric equivalence ratios ($\phi_M \sim 1.3$) at this point. The intake heaters were turned on to the desired intake temperature setpoints. As the intake temperature rose, the mass flow controllers were frequently updated to reflect the mass flow required by the corresponding intake temperature. Intake pressures as measured by a pressure transducer in the intake manifold were maintained at approximately 1.1 bar absolute. When the engine setpoint was reached, data were collected on LabVIEW and simultaneously by the GC. Typically, $H_2$ and $C_2H_6$ addition were tested only after any $CH_4$-only setpoints were performed. In tests where exhaust soot concentrations were measured, this was performed in tandem with LabVIEW and GC data collection. After all data collection was performed, the intake heaters were shut off and any $CH_4$, $H_2$ and $C_2H_6$ flows were stopped. Then, the $N_2$ supply was turned on and the mass flow controllers were stopped. Finally, the diesel supply solenoid on the engine was switched off, and once the engine came to a stop, the $N_2$ supply was shut off as well.

### 2.5.2. Catalytic Engine

To operate the catalytic engine, the VFD was used to start the Lister-Petter engine at a motor speed of 300 rpm (engine speed of 225 rpm). The same $N_2$ supply as above was used to start-up the engine. A decompressor lever was used to keep the exhaust valve open in order to reduce the torque required to perform start-up. The motor speed was increased to 750 rpm (engine speed 563 rpm), at which point this lever was closed and true compression was performed on the gases in the cylinder. Once this was achieved, the $N_2$ supply was replaced with the combustion gases.

The intake heaters were then switched on. The heater outlet temperature setpoints were 150 °C, as this was determined to be a safe operating temperature range without destroying the catalytic foam. As the intake temperature rose, a "light-off" point was achieved when the catalytic foam reached a sufficient temperature to perform its intended chemistry efficiently. This resulted in a significant rise in exhaust temperature ("light-off") as the exothermicity of the chemistry led to significant heat release in a short period of time. This is shown in Figure 4-1 as the sudden, steep rise in temperature on the exhaust temperature curve starting at approximately 6 minutes. The exhaust temperature eventually reached steady state. All LabVIEW and GC data that were collected for this engine and shown in Sections 4.1 and 4.2 were collected at steady-state exhaust temperatures.

Upon completing data collection, the cylinder was flushed with hot air to perform regeneration by oxidizing soot on catalyst active sites Afterwards, the $N_2$ supply was switched on again and the mass flow controllers were stopped. Finally, the motor was turned off.

Occasionally, after certain tests, the catalyst was severely damaged due to excessive temperatures in the cylinder. Due to the simplicity of the engine design, the catalyst replacement procedure could be performed within ~ 30 minutes. This required removal of all auxiliary fuel systems that were connected to the cylinder head, the valve cover, intake and exhaust manifolds, the cylinder head itself, and the spent catalyst. Then, a new catalytic foam was placed in the piston bowl, the cylinder walls were cleaned and re-lubricated, and the other components were returned to their original torque specifications. The engine gaskets were not replaced each time this was performed as the engine was not run for a significant amount of time or at high load.

# 3. Results & Discussion: Spark-Ignited Partial Oxidation

## 3.1. Intake Temperature

Engine performance was compared for a range of elevated intake temperatures from 350 °C to 460 °C. Preheating was required to achieve robust combustion at high equivalence ratios ($\phi_M > 1.8$) as the premixed laminar flame speed of $CH_4$ is known to increase with temperature. Bromberg et al showed that for stoichiometric methane/air mixtures, flame speeds decrease with pressure and increase with temperature. The pressure ($p$) dependence of laminar flamed speed ($s_L$) was found to be of the of the form $s_L \sim 1/p^{1/\alpha}$, while the temperature ($T$) dependence was found to be of the form $s_L \sim T^{\beta}$ [53]. The tests described in this section were performed without any additional $H_2$ or $C_2H_6$. Premixed laminar flame speeds provide a way to compare the combustibility of different fuel/air mixtures. The laminar flame speed is also relevant for misfire, as the initial development of the combustion kernel during the sparking event is related to it. If the value of $s_L$ is too low, the likelihood of misfire greatly increases. Later in the combustion process when mixing is more advanced, turbulence in the cylinder speeds up the combustion process, but the turbulent flame speed scales with the laminar flame speed [1,54]. Karim et al reported an increase in the rich mixture operating limit when increasing intake charge temperature from 25 °C to 130 °C [41]. As the equivalence ratios that were tested in this work were higher without assistance from additional $O_2$ in the oxidizer, higher temperatures were required to assist with combustion.

At ambient initial temperature and pressure, the maximum laminar flame speed of $CH_4$ is 35 cm/s at $\phi_M \sim 1.1$. At equivalence ratios above 1.5, this value drops below 10 cm/s [55]. In order to improve combustion and overall engine performance at $\phi_M > 1.8$, higher flame speeds were possible at elevated temperatures by pre-heating intake mixtures. For example, at methane-air equivalence ratios of 1.4, the flame speed of a mixture with initial temperature of 34 °C was computed to be 22 cm/s, while that with a temperature of 342 °C had a flame speed of 88 cm/s [56]. It is important to bear in mind that the true flame speed of the mixture at the point of ignition in the cylinder will be different due to turbulence in the cylinder, cooling of the gas as it passes through the intake valves, and temperature and pressure rise due to (roughly) isentropic compression work being performed on the gas by the piston. Nevertheless, $s_L$ provides qualitative insight on the engine's behavior in extreme or unconventional cases.

Figure 3-1 shows the $H_2$ to CO ratio as a function of intake temperature, for equivalence ratios between 1.8 and 2.0. Intake mixtures were heated to between 350 °C and 460 °C to investigate the effect of higher temperatures on combustion performance in the engine cylinder. Baseline spark timing of 30° BTDC was used, and intake pressure was maintained at 1.1 bar. At $\phi_M$ of 1.8, 1.9 and 2.0, $X_{CH_4}$ was 90% across the test range (Figure 3-2). Though there appeared to be a small increase in conversion efficiency at higher temperatures, this amount is not significant. The $H_2$ to CO ratio in the exhaust gases increased with $\phi_M$. This is due to the larger amount of hydrogen available at higher equivalence ratios from $CH_4$.

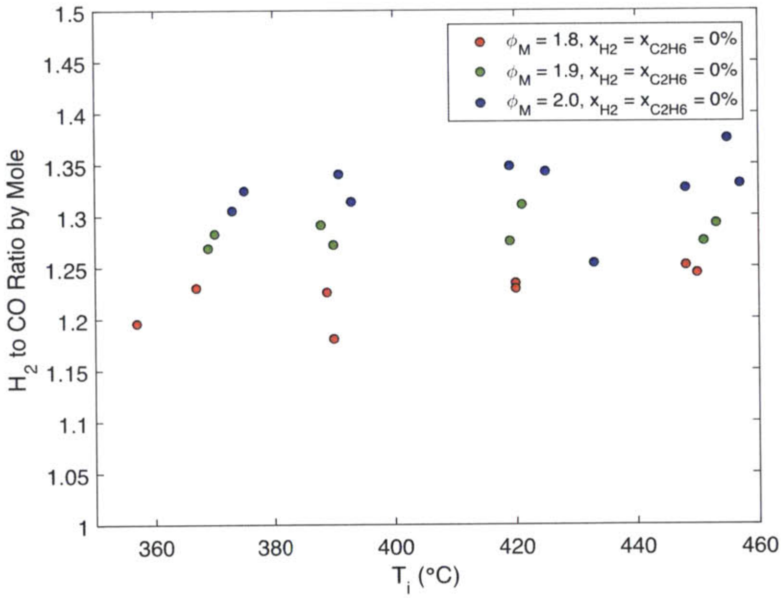

**Figure 3-1.** $H_2$ to CO ratio in engine exhaust across three methane-air equivalence ratios ($\phi_M$ = 1.8, 1.9, 2.0), from $T_i$ = 360 °C to 460 °C. No $H_2$ or $C_2H_6$ was added to the intake mixture, which was maintained at 1.1 bar. Spark ignition occurred at 30° BTDC. Each point corresponds to one sample collected on the gas chromatograph.

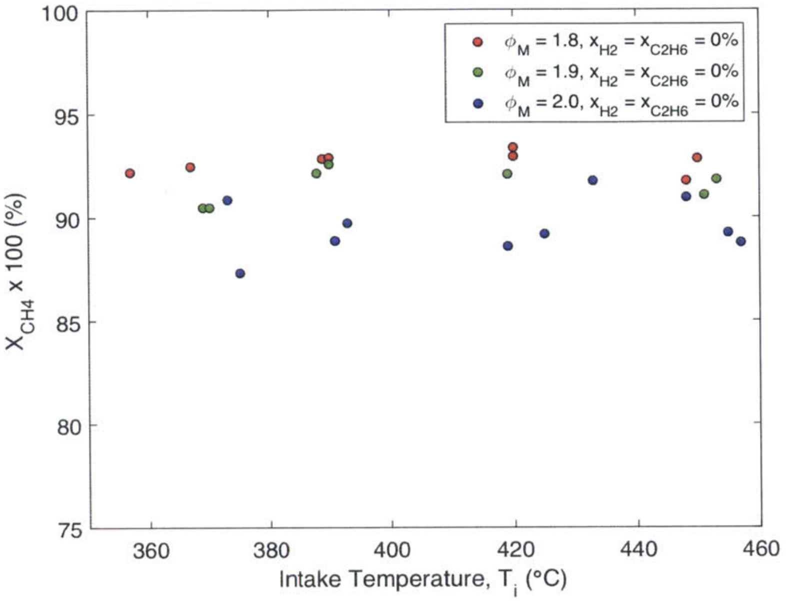

**Figure 3-2.** $CH_4$ conversion efficiency ($X_{CH_4}$), expressed as a percentage, in engine exhaust across three methane-air equivalence ratios ($\phi_M$ = 1.8, 1.9, 2.0), from $T_i$ = 360 °C to 460 °C. No $H_2$ or $C_2H_6$ was added to the intake mixture, which was maintained at 1.1 bar. Spark ignition occurred at 30° BTDC. Each point corresponds to one sample collected on the gas chromatograph.

Figure 3-3a shows the peak pressure as a function of intake temperature. Peak cylinder pressures were flat across the temperature range tested for a given equivalence ratio, but were higher for lower equivalence ratios, from 60 bar for $\phi_M$ = 2.0, to 75 bar for $\phi_M$ = 1.8. Peak pressure is a function of heat released before top-dead-center (TDC), and the trend shown here is consistent with decreasing equivalence ratio where the quantity of $O_2$ is higher relative to $CH_4$. Lower values of $\phi_M$ lead to a larger amount of heat release from complete combustion, which is significantly more exothermic than partial oxidation. At the same time, the average net indicated mean effective pressure ($nimep_{mean}$) decreased slightly with respect to temperature (Figure 3-3b), and was effectively independent of equivalence ratio for a given intake temperature. $nimep_{mean}$ is the net work performed by the engine per engine cycle after subtracting the net pumping energy performed on the gas during intake and exhaust strokes, from the net energy performed by the gas during the compression and expansion strokes, normalized by the volume of engine displacement. The total work is a function of the total chemical energy released during combustion, which should decrease with lower charge densities. With a 16%

increase in temperature (calculated in Kelvin) and therefore decrease in density by the same fraction, $nimep_{mean}$ dropped from 400 kPa to 350 kPa across the temperature range (13 % decrease). However, since the objective was not to maximize work output, this was not a concern. In other tests where intake temperature was held constant, > 450 °C was maintained as a precaution to ensure that the maximum flame speed was obtained given the limitations on the heating apparatus. In practice, this may not be necessary since the engine's performance with > 350 °C intake charge temperature appeared to be sufficient for robust spark-ignition and flame propagation across the cylinder.

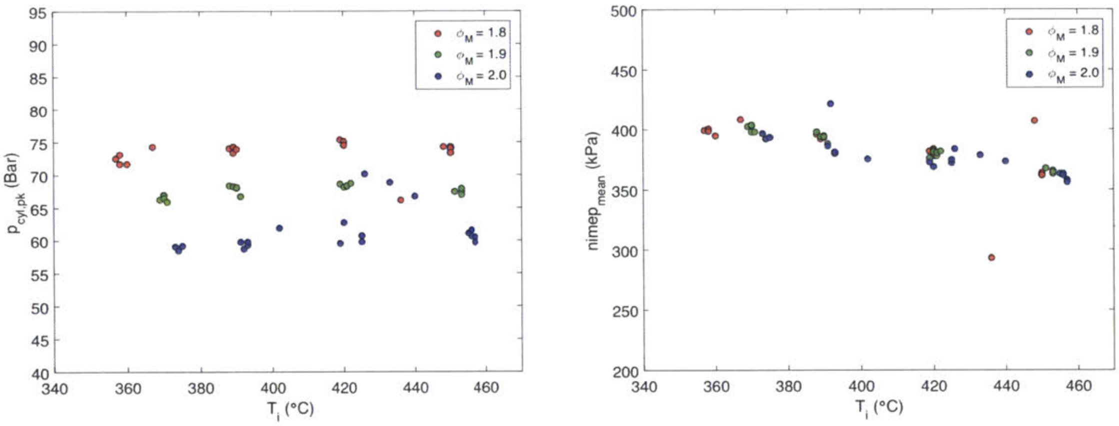

**(a)** **(b)**

**Figure 3-3.** (a) Average peak cylinder pressure ($p_{cyl,pk}$) and (b) average net indicated mean effective pressure ($nimep_{mean}$), from $T_i$ = 360 °C to 460 °C. No $H_2$ or $C_2H_6$ was added to the intake mixture, which was maintained at 1.1 bar. Spark ignition occurred at 30° BTDC. Each point corresponds to the average across 200 consecutive engine cycles.

To confirm that intake temperatures > 350 °C were sufficient to achieve reliable engine operation, tests were performed from 200 °C to 350 °C to compare performance. Below 350 °C, the engine produced significant misfire, leading to large values of $COV_{nimep}$ (Figure 3-4). This demonstrated that intake temperatures > 350 °C were high enough to trigger partial oxidation.

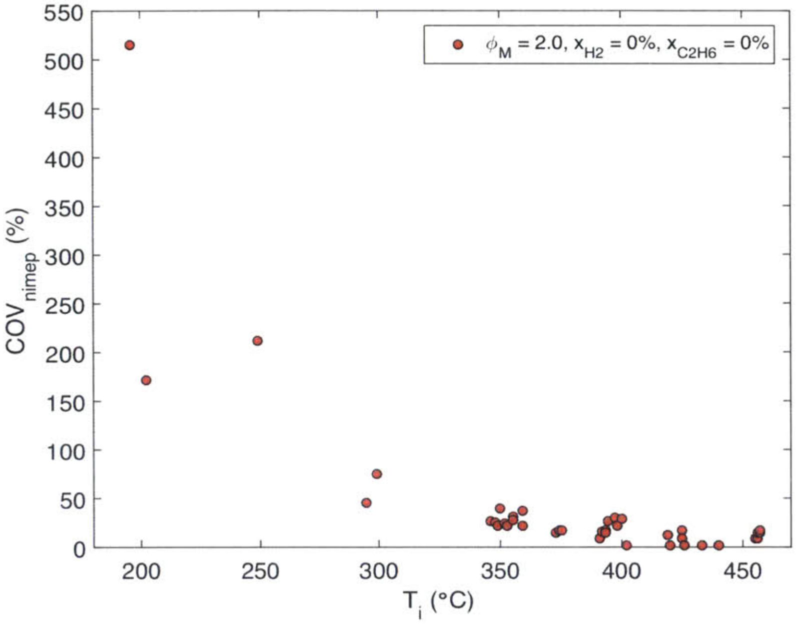

**Figure 3-4.** Coefficient of variation (COV) of NIMEP ($COV_{nimep}$) for 200 consecutive engine cycles per data point shown at a methane-air equivalence ratio ($\phi_M$) of 2.0 at intake temparatures ($T_i$) between 200 °C and 450 °C. No $H_2$ or $C_2H_6$ were added in these tests.

## 3.2. Spark Timing

Figure 3-5a shows $nimep_{mean}$ as a function of spark timing at $\phi_M = 2.0$, intake temperature of 450 °C, and intake pressure of 1.1 bar. Advancing spark timing, from 30° to 45° before top-dead-center (BTDC) piston position increased peak pressure, but produced significantly lower combustion stability (higher $COV_{nimep}$, also shown in Figure 3-5a), lower values of $nimep_{mean}$, and lower $CH_4$ conversion efficiency ($X_{CH_4}$, in Figure 3-6). The figures in 3-5b show the cylinder pressure as a function of crank angle, for 200 consecutive cycles and a corresponding histogram of the peak pressures for those 200 cycles. Combustion stability was quantified by $COV_{nimep}$. Therefore, in operating regimes where the engine alternates between periods of combustion and large periods of misfire (where combustion fails to occur entirely), the average net work output was small and the standard deviation large, resulting in very large values of $COV_{nimep}$. At spark timing of 45° BTDC a substantial number of engine cycles were misfires (large frequency of engine cycles with peak pressure of 30 bar in Figure 3-5b(1R), which corresponded to misfire). In contrast, with 30° BTDC spark timing, the histogram frequency of 30 bar peak pressure was small as shown in Figure 3-5b(4R).

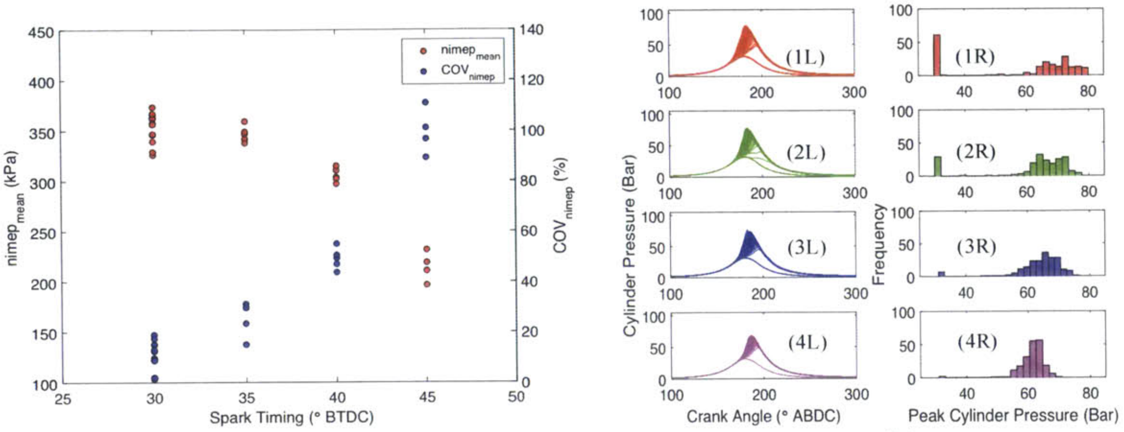

**(a)** **(b)**

**Figure 3-5.** (a) $nimep_{mean}$ and $COV_{nimep}$ with 30° to 45° BTDC spark timing. Each point corresponds to the average across 200 consecutive engine cycles. (b) The corresponding (L) cylinder pressure traces for a subsection of compression and expansion strokes, and (R) histograms of peak cylinder pressure for those traces at (1) 45° BTDC, (2) 40° BTDC, (3) 35° BTDC and (4) 30° BTDC. Each pressure trace plot and histogram displays 200 consecutive engine cycles.

Spark timing advancement led to ignition occurring increasingly before top-dead-center (TDC), when the in-cylinder pressure and temperature at the point of sparking were both lower. There are two competing mechanisms. First, lower cylinder pressures and temperatures at sparking led to lower flame speeds and combustibility of the gas. As a result, there was a higher incidence of misfire with increasingly advanced spark timing as shown in Figure 3-5b(1L, 1R). However, earlier spark events allow the gas more time to react, and therefore more heat to be released before TDC if combustion were to occur at all. This explains the higher peak pressures achieved during successful combustion cycles. For example, in Figure 3-5b(1R), maximum peak pressures were 80 bar, while in Figure 3-5b(4R), maximum peak pressures were 70 bar). These higher pressures led to a slight gain in $H_2$ to CO ratio > 1.4 by improving the conditions for partial oxidation (Figure 3-6). On the other hand, more delayed spark timing led to less heat being released before TDC and hence lower peak pressures. However, this also led to higher work output due to the alignment between heat release and piston position as it travelled downward during the expansion stroke. The negative effect of delayed timing on $H_2$ to CO ratio was modest. The net result was that the most advanced timing at 45° BTDC led to higher maximum peak pressures, but significant misfire at these conditions leads to lower $nimep_{mean}$ (~ 200 kPa), poor $CH_4$ conversion (~ 60 %), and high values of $COV_{nimep}$ (> 100 %). In comparison, more delayed spark timing at 30° BTDC led to higher $nimep_{mean}$ (~ 350 kPa), higher $CH_4$ conversion ~ 90 %, and low values $COV_{nimep}$< 20 %.

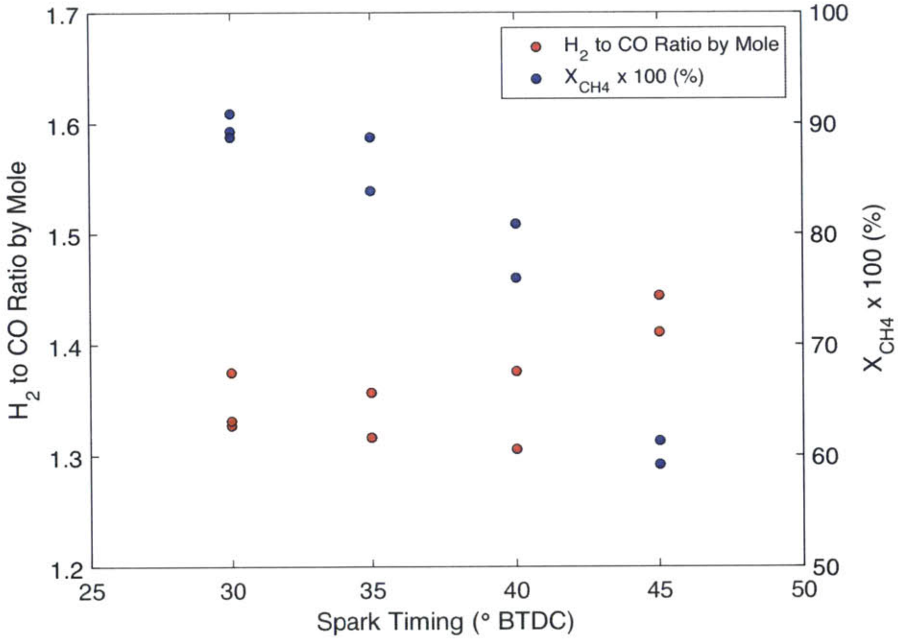

**Figure 3-6.** $H_2$ to CO ratio in exhaust gases, and $CH_4$ conversion efficiency ($X_{CH_4}$), expressed as a percentage, with 30° to 45° BTDC spark timing advancement. $\phi_M = 2.0$, $T_i = 450$ °C, and $p_i = 1.1$ bar. Each point corresponds to one sample collected on the gas chromatograph.

Overall, a delay in spark timing led to a slight decrease in syngas quality (lower $H_2$ to CO ratio) as it led to lower overall peak pressures, lower peak cylinder temperatures [1], and therefore an equilibrium in the water-gas shift reaction that favored CO production. However, this delay also led to a significant improvement in combustion stability, and therefore was pereferrable for syngas production due to smoother operation. For the tests performed in sections 3.3-3.6, 30° BTDC spark timing was used.

## 3.3. Hydrocarbon-Air Equivalence Ratio

The spark-ignited engine demonstrated robust combustion with $COV_{nimep}$ < 20% at $\phi_M$= 2.0, in the absence of hydrogen or ethane, at an inlet temperature and pressure of 450 °C and 1.1 bar, and spark timing of 30° BTDC. The value of $COV_{nimep}$ at this condition is shown in Figure 3-7. $\phi_M$= 2.0 defined the "borderline" condition (Figure 3-8b) without chemical assistance from $H_2$ or $C_2H_6$, both of which increase flame speed. At an equivalence ratio $\phi_M$ = 2.1 (Figure 3-8c), misfire occurred frequently enough to reduce combustion stability and increase $COV_{nimep}$ to 30 % (Figure 3-7), and reduce $X_{CH_4}$ below 90% (Figure 3-11). At the "borderline" condition of $\phi_M$ = 2.0, the engine could still operate reliably without $H_2$ recycle, though at the expense of relatively low $H_2$ to CO ratio of 1.3. Note that results showing $C_2H_6$ addition are also included in this section, where the presence of $C_2H_6$ is noted in the plot legends.

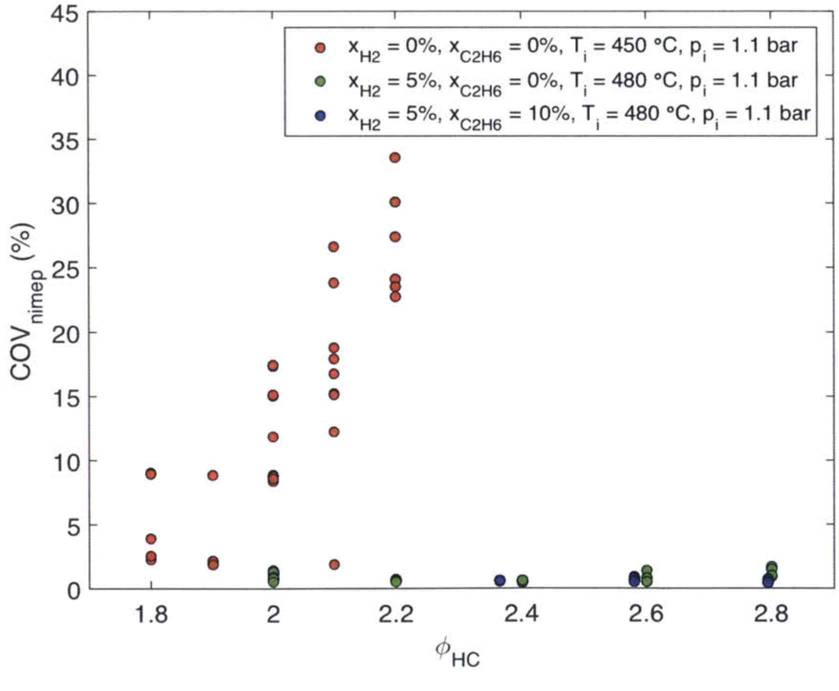

**Figure 3-7.** Coefficient of variation (COV) of NIMEP ($COV_{nimep}$) for hydrocarbon-air equivalence ratios $\phi_{HC}$ from 1.8 to 2.8, contrasting the effects of $H_2$ and $C_2H_6$. Each point corresponds to the average of 200 consecutive engine cycles.

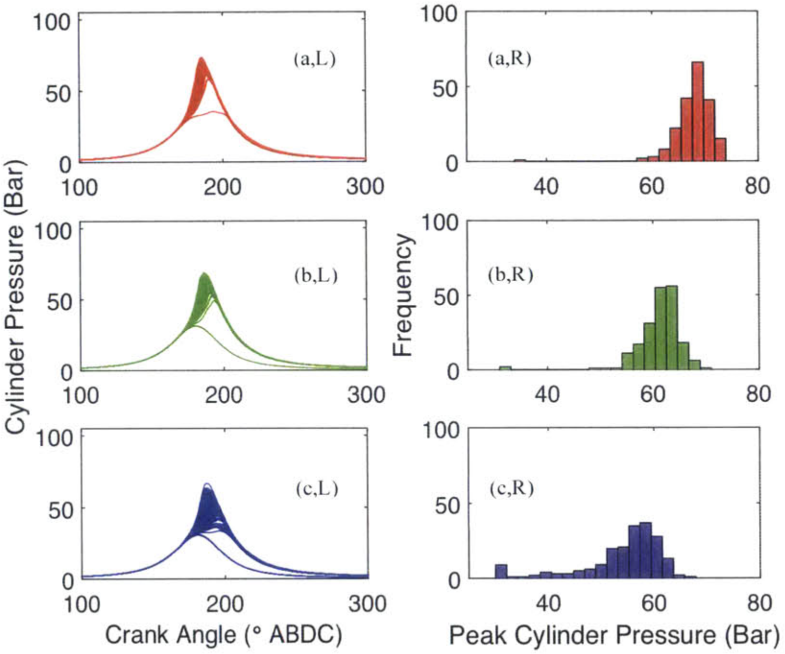

**Figure 3-8.** (L) Cylinder pressure traces for subsection of compression and expansion strokes, and (R) histograms of peak cylinder pressure for those cycles. (a) $\phi_M$ = 1.9, (b) $\phi_M$ = 2.0, (c) $\phi_M$ = 2.1. $T_i$ and $p_i$ were both held constant at 450 °C and 1.1 bar respectively. Each pressure trace plot and histogram corresponds to 200 consecutive engine cycles.

Figure 3-9 shows the peak pressure as a function of equivalence ratio, showing the results both with and without hydrogen and ethane addition. Peak pressure tended to fall with increasing equivalence ratios, from $\phi_{HC}$ = 1.8 to 2.8, at the same spark timing of 30° BTDC. The peak pressure was reduced somewhat by the strong presence of misfire, so only conditions with $COV_{nimep}$ < 35% are shown here. The peak pressure achieved in the cylinder depends on the cumulative heat released before TDC, which scales with the relative quantity of complete combustion relative to partial oxidation. Naturally, more of the latter occurs at higher values of $\phi_{HC}$, and hence smaller peak pressures are developed at richer conditions. The relative advantage in heat release is seen at $\phi_{HC} = 2.2$, where $H_2$ addition increased the average peak pressure from 47 bar to 55 bar. At $\phi_{HC} \geq 2.2$ without $H_2$ or $C_2H_6$, combustion was poor and results are not shown. However, the benefit of $C_2H_6$ is compared at these equivalence ratios, where heat release was higher due to the increase in heating value of the mixture when 10% by volume of $CH_4$ was effectively replaced with $C_2H_6$. The heating value per mole of fuel of $C_2H_6$ was double that of $CH_4$ (the lower heating values are 1,560 kJ/mol and 890 kJ/mol respectively). For example, at $\phi_{HC} = 2.8$, $H_2$ addition without $C_2H_6$ yielded a peak pressure of only 37 bar (the motoring trace peaked at 30 bar). The addition of $C_2H_6$ increased the peak pressure significantly to 47 bar, which corresponded to combustion at $\phi_{HC} = 2.2$ with neither $H_2$ nor $C_2H_6$. However, the benefit of $C_2H_6$ on heat release (and therefore peak pressure) at high equivalence ratios must be matched with the appropriate composition in exhaust gases, and this is where the chemical inefficiencies at the extreme operating regimes must be considered at the same time.

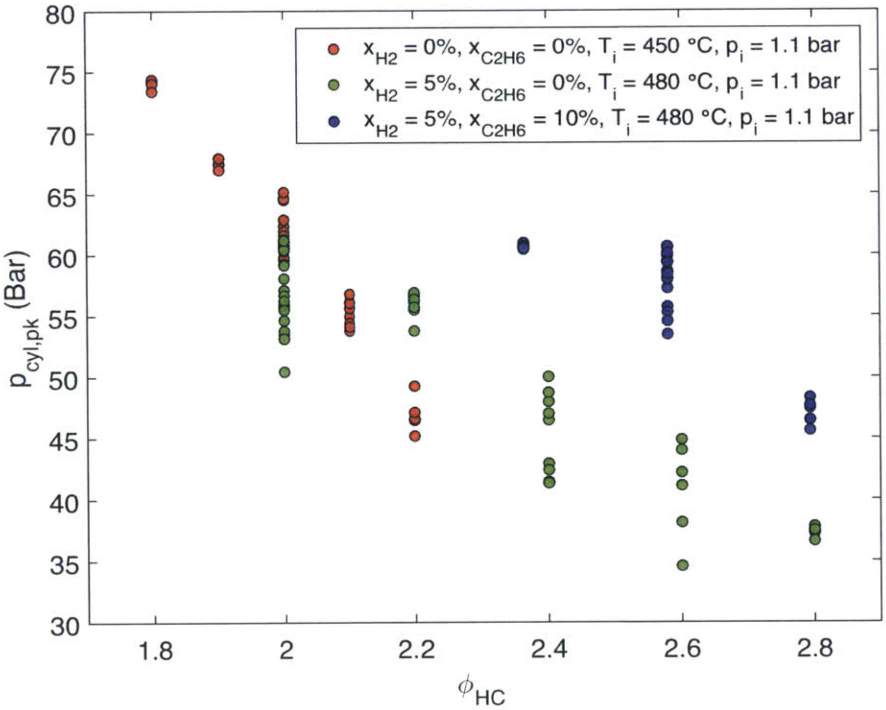

**Figure 3-9.** Average peak cylinder pressure for hydrocarbon-air equivalence ratios $\phi_{HC}$ from 1.8 to 2.8, contrasting the effects of $H_2$ and $C_2H_6$. Each point corresponds to the average of 200 consecutive engine cycles.

Figure 3-10 shows the $H_2$ to CO ratio for the same data as Figure 3-9. As expected, increasing the equivalence ratio, even in the absence of hydrogen, increased the $H_2$ to CO ratio. However, there was a much larger impact when $H_2$ or $C_2H_6$ were added. The presence of either increased the $H_2$ to CO ratio by about 0.3 (from 1.3 to 1.6), and extended the equivalence ratio further. It should be noted, however, that the addition of ethane did not measurably affect the $H_2$ to CO ratio, over that with just hydrogen addition.

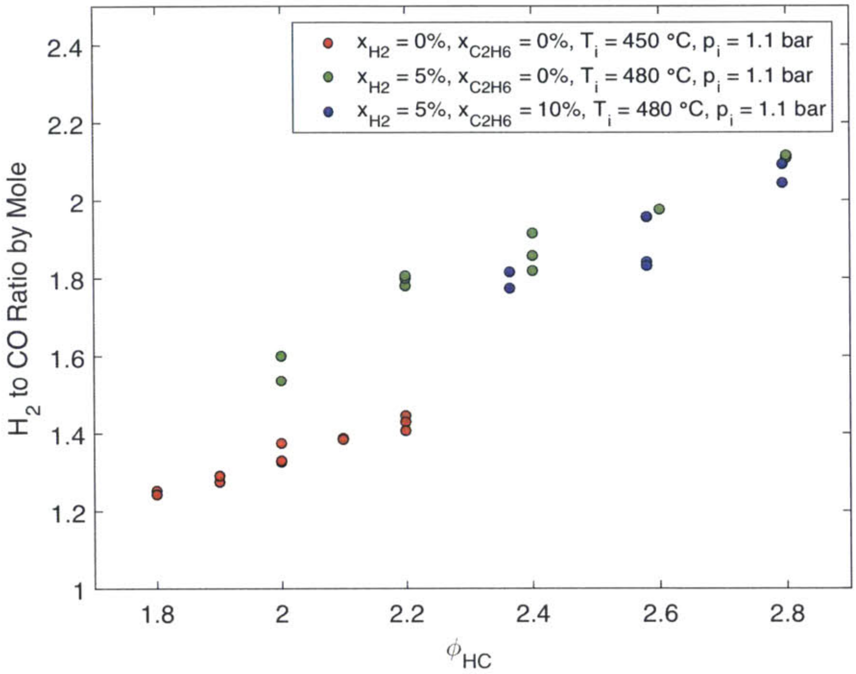

**Figure 3-10.** $H_2$ to CO ratios for hydrocarbon-air equivalence ratios $\phi_{HC}$ from 1.8 to 2.8, contrasting the effects of $H_2$ and $C_2H_6$. Each point corresponds to one sample collected on the gas chromatograph.

Figure 3-11 shows the conversion efficiency of the hydrocarbons for the same data as shown in Figures 3-9 and 3-10. The downside of operating at increased equivalence ratio $\phi_{HC} \geq 2.4$ was a reduction conversion. The conversion of $CH_4$ and $C_2H_6$ both fell below 90% at these equivalence ratios, and as low as 65% for $CH_4$ at $\phi_{HC} = 2.8$. These stunted conversion values were due to $CH_4$'s very low reaction rates (compared to that of hydrogen), leading to preferential combustion of $H_2$.

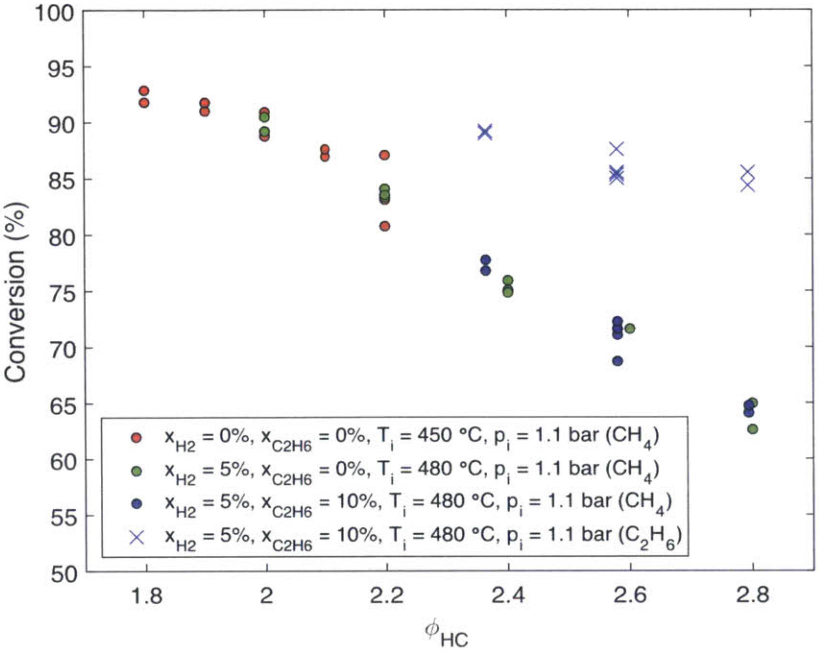

**Figure 3-11.** $CH_4$ and $C_2H_6$ conversion efficiencies ($X_{CH_4}$ and $X_{C_2H_6}$, expressed as percentages) for hydrocarbon-air equivalence ratios $\phi_{HC}$ from 1.8 to 2.8, contrasting the effects of $H_2$ and $C_2H_6$. Each point corresponds to one sample collected on the gas chromatograph.

Given these deficiencies, the upside of operating at these rich mixtures were twofold. First, the addition of $H_2$ and $C_2H_6$ led to low $COV_{nimep}$ < 5% as a result of stable combustion. Figure 3-7 shows $COV_{nimep}$ for the same data as Figures 3-9 to 3-11. The flame speed of the rich mixtures tested at $\phi_{HC} \geq 2.4$ were simulated in Cantera and found to be < 10 cm/s. While this is low, it did not lead to variability. That is to say, while not all of the $CH_4$ reacted due to lower methane conversion efficiencies as shown in Figure 3-11, this performance was stable from cycle-to-cycle. Figure 3-12 demonstrates the effect of $H_2$ and $C_2H_6$ on combustion variability, where the histogram of peak pressures fell within a band 5-8 bar wide when those gases were added. Second, high equivalence ratios $\phi_{HC} \geq 2.4$ were needed to produce exhaust mixtures with $H_2$ to CO ratios close to 2.0, which is desirable for liquids synthesis. There did not appear to be a benefit to the $H_2$ to CO ratio by replacing 10% of the $CH_4$ with $C_2H_6$, though the effect was not detrimental. In fact, the conversion of $C_2H_6$ did not fall below 80% even in the richest conditions (Figure 3-11), though there appeared to be a downward trend in conversion similar to that for $CH_4$.

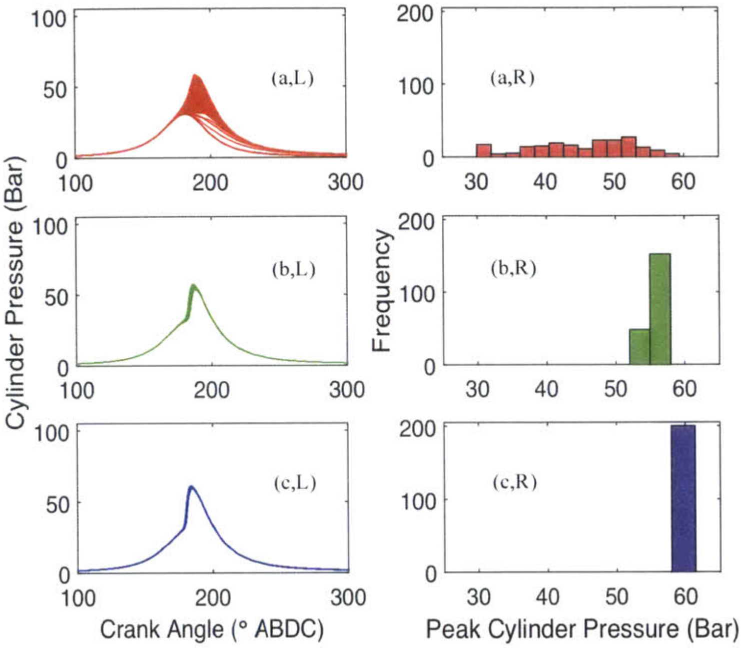

**Figure 3-12.** (L) Cylinder pressure traces for subsection of compression and expansion strokes, and (R) histograms of peak cylinder pressure for those cycles. (a) $\phi_{HC}$ = 2.2, $x_{H_2}$ = 0%, $x_{C_2H_6}$ = 0%, $T_i$ = 450 °C, $p_i$ = 1.1 bar, (b) $\phi_M$ = 2.2, $x_{H_2}$ = 5%, $x_{C_2H_6}$= 0%, $T_i$ = 480 °C, $p_i$ = 1.1 bar, (c) $\phi_{HC}$ = 2.4, $x_{H_2}$ = 5%, $x_{C_2H_6}$ = 10%, $T_i$ = 480 °C, $p_i$ = 1.1 bar. Each pressure trace plot and histogram corresponds to 200 consecutive engine cycles.

Ultimately, a compromise must be made between the absolute quantity of $CH_4$ converted, and the $H_2$ to CO ratio that can be achieved in the exhaust gas. The volumetric flow rate of $CH_4$ at standard conditions (25 °C, 1 atm) that was introduced to the engine, and that was converted ($\dot{V}^{\circ}_{CH_4} \cdot X_{CH_4}$), is shown in Figure 3-13, using the conversion efficiencies shown in Figure 3-11. This demonstrates that the highest flow rates of $CH_4$ occurred for cases without $H_2$ and $C_2H_6$, which of course were both added in place of $CH_4$. More importantly, $\phi_{HC} \geq 2.4$ showed a downward trend in $\dot{V}^{\circ}_{CH_4} \cdot X_{CH_4}$, due to the decrease in methane conversion efficiency due to extremely rich operation. It appeared that the optimum equivalence ratio was $\phi_{HC}$ = 2.2, including $H_2$ recycle. Here, the $H_2$ to CO ratio was ~ 1.8, and combustion did not suffer from significant conversion inefficiency.

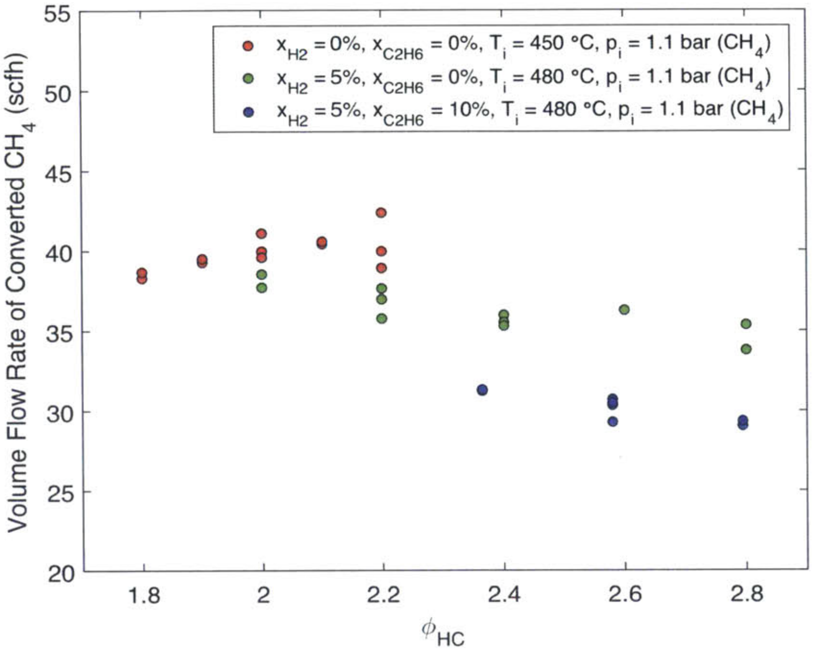

**Figure 3-13.** Standard volumetric flow rate of $CH_4$ from the intake that was converted in the engine ($\dot{V}^{\circ}_{CH_4} \cdot X_{CH_4}$), based on conversion efficiency data in Figure 3-11. Each point corresponds to one sample collected on the gas chromatograph.

## 3.4. Ethane Concentration

The effect of $C_2H_6$ on engine reforming capability was studied by varying its concentration relative to $CH_4$. In the experiment, methane was replaced by ethane on a 1-to-1 basis, by 5% increments up to 20%. That is to say, the total number of moles of fuel were held constant, and the fraction occupied by $C_2H_6$ was steadily increased. In the figures described in this section, $\phi_M$ is the value used in Eq. 15, where a fraction $x_{C_2H_6}$ of $CH_4$ is replaced with $C_2H_6$. Figure 3-14 shows that at constant values of $\phi_M$, the $H_2$ to CO ratio in the exhaust did not vary significantly, up to $x_{C_2H_6} = 20\%$. The ideal partial oxidation of $C_2H_6$ produced an $H_2$ to CO ratio of 1.5, which may explain this mild relationship. The large difference in $H_2$ to CO ratio between $\phi_M = 2.0$ and 2.4 is expected, and this was demonstrated earlier in Figure 3-10, which showed that leaner mixtures achieved lower $H_2$ to CO ratios than richer ones.

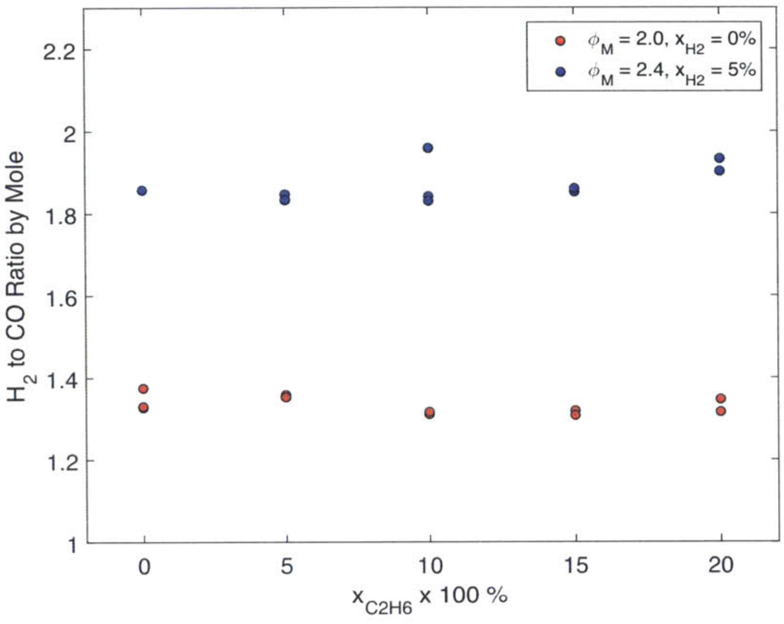

**Figure 3-14.** $H_2$ to CO ratio for different concentrations of $C_2H_6$ in $CH_4$ ($x_{C_2H_6}$, expressed as a percentage) from 0% to 20%. Comparison shown for $\phi_M = 2.0$ ($x_{H_2} = 0\%$) and 2.4 ($x_{H_2} = 5\%$) with different values of $x_{C_2H_6}$. Note: the value of $\phi_{HC}$ is not the same at different $x_{C_2H_6}$. Each point corresponds to an average of 200 consecutive engine cycles.

Figure 3-15 shows the $CH_4$ conversion as a function of $x_{C_2H_6}$, for the same conditions as Figure 3-14. The practical effect of increasing $x_{C_2H_6}$ while keeping the total number of moles of fuel constant was that the overall hydrocarbon-air equivalence ratio increased ($\phi_{HC} > \phi_M$), leading to decreased $CH_4$ conversion due to poorer combustion. For example, a conversion of only 65% was achieved with $x_{C_2H_6}$ = 20%, compared to 75% conversion with $x_{C_2H_6}$ = 0%. The decrease in $CH_4$ conversion was not seen when $\phi_M$ = 2.0, where $CH_4$ conversion values did not fall below 87% regardless of the value of $x_{C_2H_6}$ (up to 20%). At these lower equivalence ratios, the mixture was reactive enough to burn to close to completion in the given cycle time.

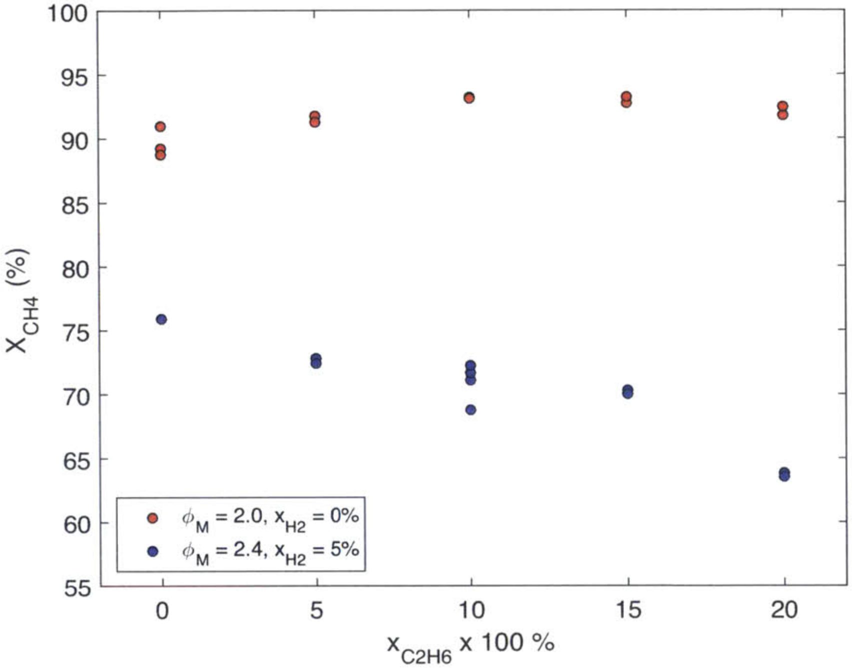

**Figure 3-15.** $CH_4$ conversion efficiency ($X_{CH_4}$), expressed as a percentage, for different concentrations of $C_2H_6$ in $CH_4$ ($x_{C_2H_6}$, expressed as a percentage) from 0% to 20%. Comparison shown for $\phi_M = 2.0$ ($x_{H_2} = 0\%$) and 2.4 ($x_{H_2} = 5\%$) with different values of $x_{C_2H_6}$. Note: the value of $\phi_{HC}$ is not the same at different $x_{C_2H_6}$. Each point corresponds to an average of 200 consecutive engine cycles.

Figures 3-16 and 3-17 show the peak pressure and the COV of NIMEP for the same conditions as Figures 3-14 and 3-15. Increasing the concentration of $C_2H_6$ resulted in higher peak pressures with consistently low values of $COV_{nimep}$. For $x_{C_2H_6} > 10\%$ however, the peak pressure was insensitive to $x_{C_2H_6}$. It is likely that low flame speeds coupled with decreasing $CH_4$ conversion led to this plateau in peak pressure.

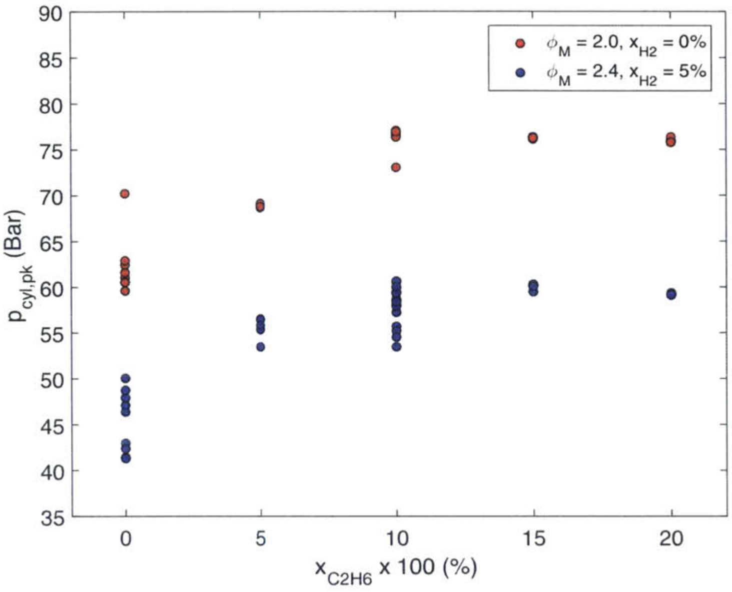

**Figure 3-16.** Average peak cylinder pressure ($p_{cyl,pk}$) for different concentrations of $C_2H_6$ in $CH_4$ ($x_{C_2H_6}$, expressed as a percentage) from 0% to 20%. Comparison shown for $\phi_M = 2.0$ ($x_{H_2} = 0\%$) and 2.4 ($x_{H_2} = 5\%$) with different values of $x_{C_2H_6}$. Note: the value of $\phi_{HC}$ is not the same at different $x_{C_2H_6}$. Each point corresponds to an average of 200 consecutive engine cycles.

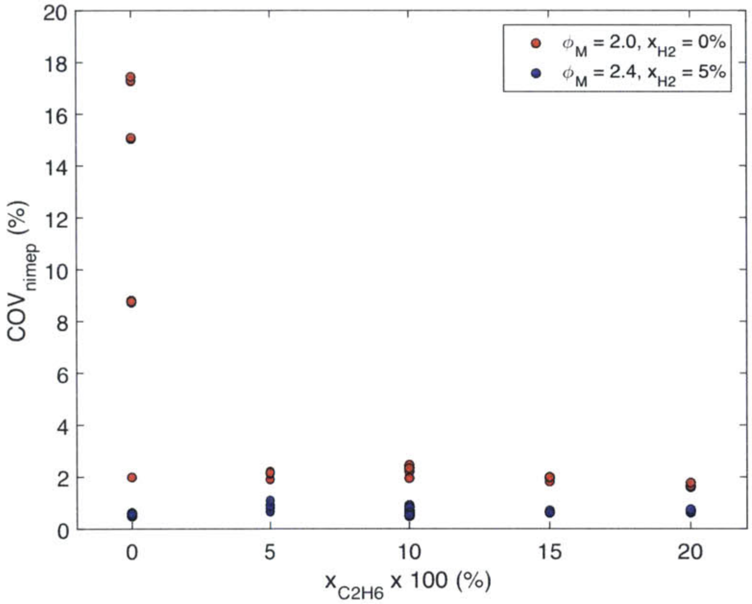

**Figure 3-17.** Coefficient of variation (COV) of NIMEP ($COV_{nimep}$) for different concentrations of $C_2H_6$ in $CH_4$ ($x_{C_2H_6}$, expressed as a percentage) from 0% to 20%. Comparison shown for $\phi_M = 2.0$ ($x_{H_2} = 0\%$) and 2.4 ($x_{H_2} = 5\%$) with different values of $x_{C_2H_6}$. Note: the value of $\phi_{HC}$ is not the same at different $x_{C_2H_6}$. Each point corresponds to an average of 200 consecutive engine cycles.

## 3.5. Engine Knock

With the original compression ratio of 18.9:1, the geometry of the piston (Figure 3-18) contained a large flat upper surface (the was situated in the "squish region"). Squish occurs in the engine cylinder at the end of the compression stroke when the piston upper surface and cylinder head approach each other closely. At this point, there tends to be radial inward and outward motion of the charge, but does not contribute to turbulent mixing. As this was a spark-ignited cylinder, with the spark plug situated along the axis of the cylinder, the flame that was generated at the time of spark tended to propagate into the piston bowl due to the turbulence that was generated by its geometry. However, the squish region likely contained stagnant charge in which flame propagation was slow. Therefore, these pockets could "autoignite" (spontaneously ignite) by the compression of the prevailing pressure before they were consumed by the flame. This is called engine "knock", and tends to occur in spark-ignited engines when mixtures are too hot. Autoignition of these pockets leads to a sudden rise in pressure and temperature in a local region. This leads to shock and expansion waves that travel across the cylinder and interact at a certain resonance frequency, thereby producing oscillations in cylinder pressure measurements [1,57].

Knock was mild at higher equivalence ratios when no $H_2$ or $C_2H_6$ were added, and higher at lower equivalence ratios. Figures 3-19a and b show the pressure traces of knock events at $\phi_M = 1.8$ and 2.2. The effect of adding $H_2$ and $C_2H_6$ are shown in Figure 3-20 and 3-21 respectively. Due to the higher per unit mass heat release achieved with the addition of these two compounds, the amplitude of oscillation in the cylinder pressure trace was higher than that without $H_2$ or $C_2H_6$. Due to the low molar mass of $H_2$, the chemical energy of $H_2$ that was added to the intake was not significant (5% by volume) in comparison to $C_2H_6$. Therefore, the amplitude of oscillation with $C_2H_6$ addition was larger than with $H_2$, where higher concentrations of $C_2H_6$ produced larger oscillations.

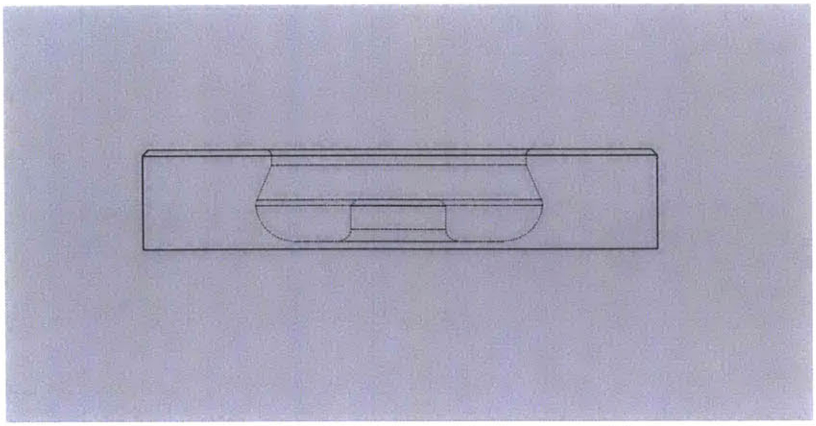

**Figure 3-18.** Original piston bowl geometry as viewed from the side.

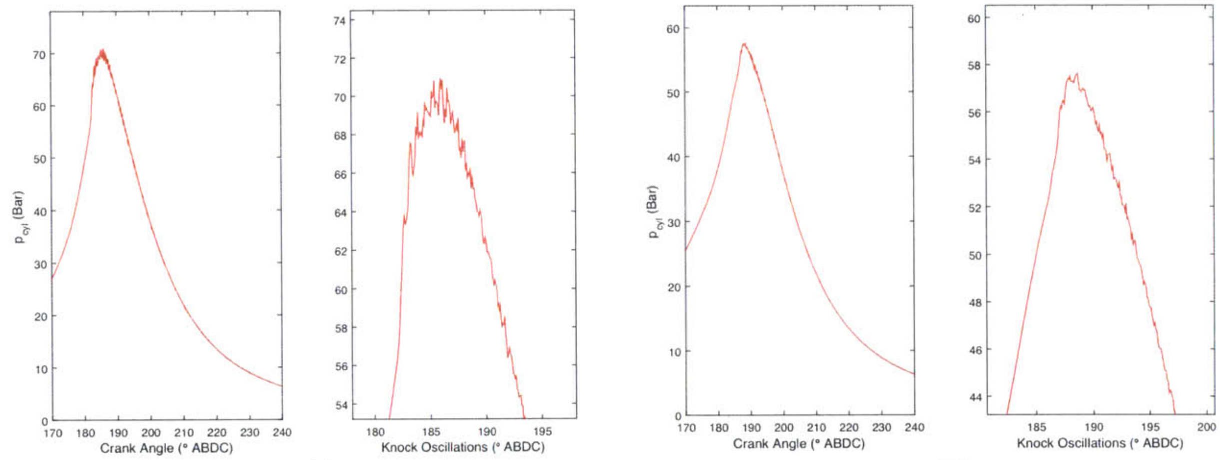

**(a)** **(b)**

**Figure 3-19.** Both (a) and (b) are at $T_i = 450$ °C, $p_i = 1.1$ bar, $x_{H_2} = 0\%$, $x_{C_2H_6} = 0\%$, spark timing 30° BTDC. (a) $\phi_M = 1.8$; (b) $\phi_M = 2.2$.

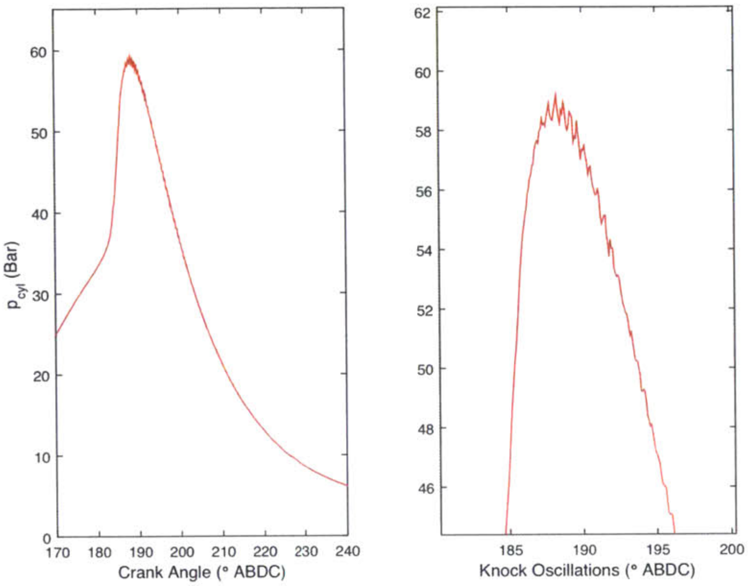

**Figure 3-20.** $T_i = 460$ °C, $p_i = 1.1$ bar, $x_{H_2} = 5\%$, $x_{C_2H_6} = 0\%$, spark timing 30° BTDC.

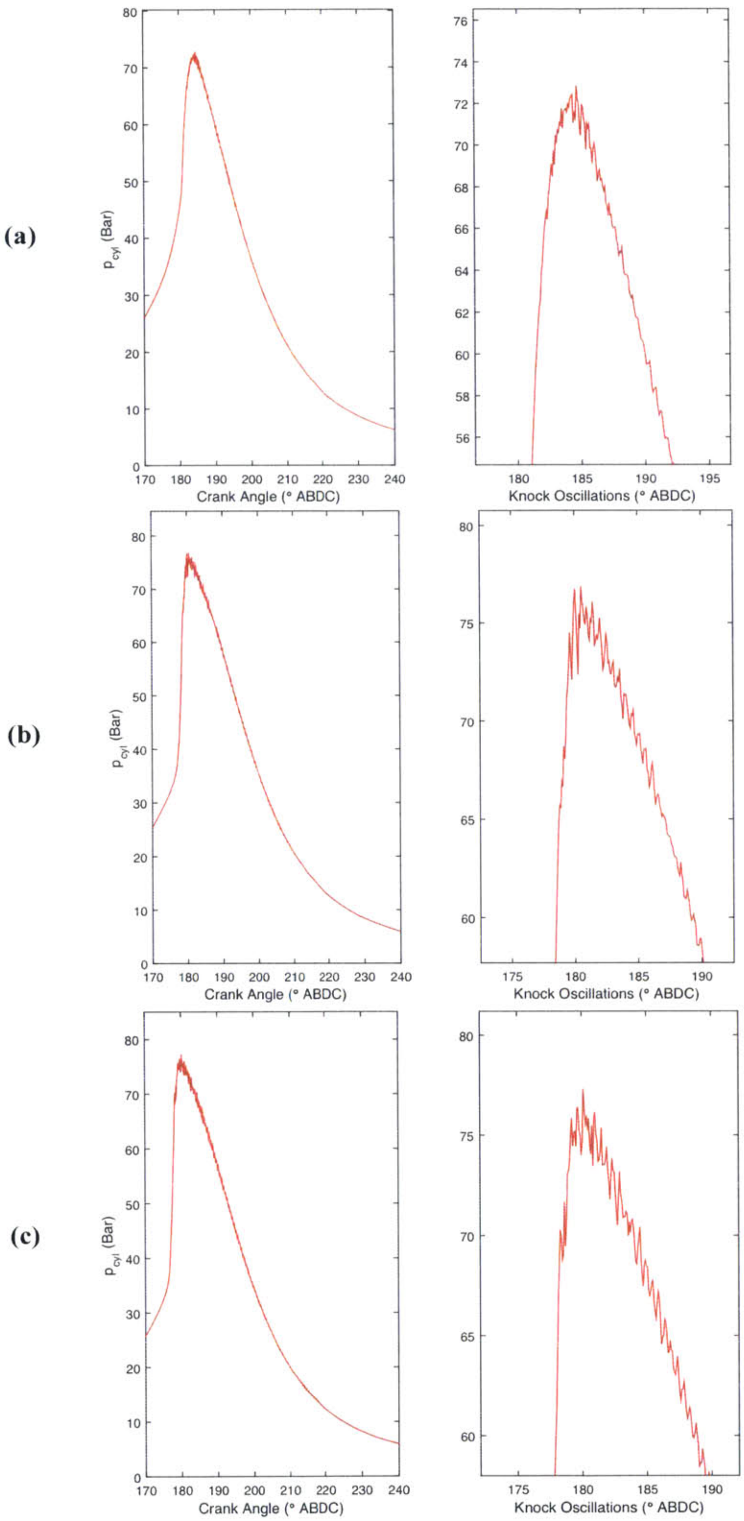

**Figure 3-21.** Both (a), (b) and (c) are at $\phi_M = 2.0$, $T_i = 460$ °C, $p_i = 1.1$ bar, $x_{H_2} = 0\%$, and spark timing 30° BTDC. (a) $x_{C_2H_6} = 5\%$; (b) $x_{C_2H_6} = 15\%$; (c) $x_{C_2H_6} = 20\%$.

## 3.6. Soot Concentration in Exhaust Gases

Figure 3-22 shows exhaust soot concentrations, measured gravimetrically across a range of hydrocarbon-air equivalence ratios, with and without $H_2$ and $C_2H_6$ addition. The soot concentrations at $\phi_{HC} \geq 2.4$ were found to be on the same order of magnitude as maximum concentrations found in a swirl-chamber IDI diesel engine [58], and ranged from 1-3 mg/L. The replacement of $CH_4$ with 10% by mole of $C_2H_6$ did not appear to increase soot production at the same value of $\phi_{HC}$. The increase in the value of $\phi_{HC}$ led to a steep rise in soot output, at approximately a rate of 22.5 mg/L for every unit increase in $\phi_{HC}$ above a value of $\phi_{HC} = 2.4$. This rise is expected to plateau as the flame speed of the mixture would be too low above a certain value of $\phi_{HC}$. These large concentrations of soot would be detrimental to catalytic systems downstream of the engine. Therefore, either a particulate filter would have to be installed and frequently regenerated, or the engine would have to be operated at a lower equivalence ratio to prevent high soot output from occurring.

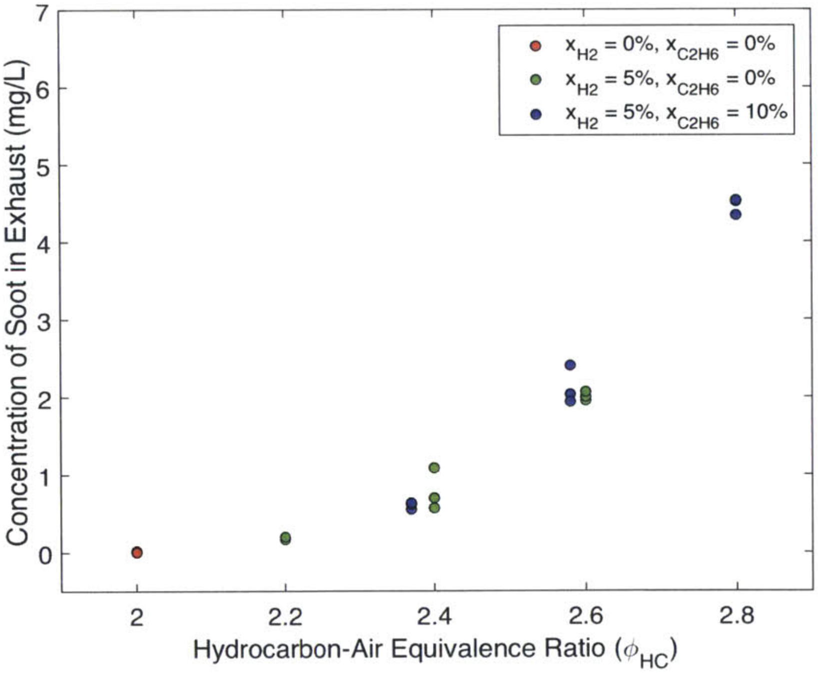

**Figure 3-22.** Soot concentration in exhaust gases, measured gravimetrically, at hydrocarbon-air equivalence ratios $\phi_{HC} = 2.0$ to 2.8, contrasting the effects of $H_2$ and $C_2H_6$.

The effect of lower intake temperatures on exhaust soot concentrations was studied by operating the engine at 350 °C in the intake, at similar mixture compositions as tested at higher intake temperatures. This comparison is shown in Figure 3-23. The decrease in intake temperature led to a reduction in the maximum equivalence ratio that could be achieved with reliable combustion. The results shown for lower intake temperatures are only for cases where the engine did not incur a significant number of misfire cycles. The reduction in temperature did not appear to reduce the amount of soot production. If the results at higher temperature are extrapolated to lower equivalence ratios, the amount of soot production should be similar to that at lower temperatures. This can be explained by the fact that lower intake temperatures lead to less oxidative environments for soot in the cylinder, while higher temperatures during the exhaust stroke would allow soot to be oxidized more completely before leaving with the exhaust gases. The results show that if lower temperatures are desired to reduce the heating capacity in the intake, there does not appear to be a significant effect on soot production ($\phi_{HC}$ < 2.4). However, higher temperatures are required to reach higher equivalence ratios.

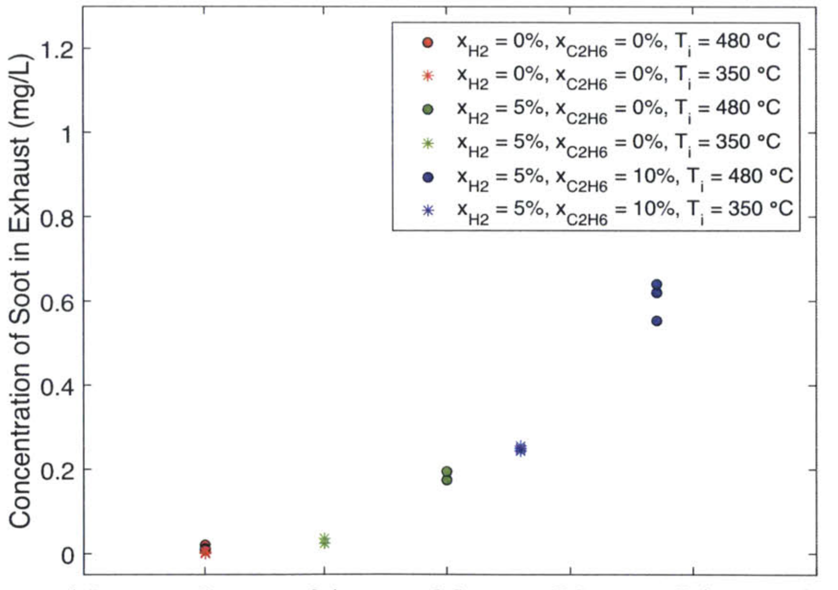

**Figure 3-23.** Soot concentration in exhaust gases, measured gravimetrically, at hydrocarbon-air equivalence ratios $\phi_{HC}$ = 2.0 to 2.4, at 350 °C and 480 °C respectively, contrasting the effects of $H_2$ and $C_2H_6$.

According to EPA Title 40: Protection of Environment PART 1039 Subpart B, which regulates particulate matter (PM) emissions from new and in-use nonroad compression-ignition engines, the maximum allowable PM emissions is 0.4 g /kWh [59], or 0.5 mg/L, for a 0.5 L, 19 kW diesel engine operating at 1000 rpm. The values obtained in experiment are up to 9 times higher than this standard at $\phi_{HC} \geq 2.2$. However, federal regulations are not fair metrics for evaluation for three reasons. First, the engine is intentionally run with low combustion efficiency and high equivalence ratio in order to obtain the desired chemical composition at exhaust. High soot production under these extreme conditions is not surprising. Second, regulations are with respect to tailpipe emissions, and therefore do not cite the intermediate values that occur in the exhaust manifold. Regulations are satisfied with the help of diesel particulate filters and catalytic converters, neither of which were used in these tests. Lastly, in practice, the engine will be in line with a synthesis reactor and its emissions will not be passed to the atmosphere. There will likely be a cleanup step to manage and remove any soot produced. In the future, liquid water injecting in the cylinder will be tested to determine its effect on soot formation at high equivalence ratios.

To better understand soot formation in the engine, a premixed rich flame was simulated using the USC Mech II chemistry model. Benzene – a precursor to soot – was used to qualitatively compare sooting trends as a function of fuel equivalence ratio. Flat, premixed laminar flame simulations were conducted for the conditions in Figure 16 for unburned gas temperatures of 750 K and at a pressure of 9 atm (an estimation of the physical state of the unburned fuel mixture at the moment of ignition). Peak benzene concentrations were used to infer the sooting propensity of fuel rich mixtures relative to $\phi_{HC} = 2$. The relative quantities of benzene formation for different hydrocarbon-air equivalence ratios are shown in Table 5. A qualitative trend can be seen for this laminar flame that also predicts the monotonic increase in soot production with increasing equivalence ratio. In reality, soot production was accelerated due to turbulence in the engine cylinder [60].

**Table 3-1.** The relative quantity of benzene that was computed at various hydrocarbon-air equivalence ratios ($\phi_{HC}$).

| $\phi_{HC}$ | **Relative Benzene Formation Normalized to $\phi_{HC} = 2.0$** |
|---|---|
| 2.00 | 1.00 |
| 2.20 | 1.71 |
| 2.37 | 2.00 |
| 2.40 | 2.24 |
| 2.58 | 2.38 |
| 2.80 | 2.58 |

## 3.7. Compression Ratio

The results shown so far from the spark-ignited engine were performed with the test cylinder's original compression ratio of 18.9:1. Results shown in this section demonstrate the engine's performance with a compression ratio of 13.8:1. The purpose of this reduction was to determine a reliable operating regime for a compression ratio more akin to one that would be tested in a larger demonstration engine. To avoid the hassle of retrofitting a diesel engine to perform spark-ignition, it was decided that a conventionally spark-ignited natural gas engine with a lower compression ratio would suffice in a demonstration plant. To prove that the results shown above were also possible at these compression ratios, an engine map was generated to test the engine's performance at different operating conditions.

Due to the lower compression ratio, the peak cylinder pressure in the motoring trace after installing the modified piston was ~ 20 bar, while that with the original piston was ~ 30 bar. If modeled as isentropic compression, this reduction in peak pressure is reasonable. Isentropic compression of the gases in the cylinder can be modeled by Eq. 45, which relates the initial (1) and final (2) volume ($V_i$) and pressure ($p_i$), the compression ratio $r_c = \frac{V_1}{V_2}$, and the ratio of specific heats $\gamma$.

$$\left(\frac{V_1}{V_2}\right)^{\gamma} = r_c = \frac{p_2}{p_1} \qquad (45)$$

In order to compare the relationship between two different cylinder geometries and compression ratios, the Eq. 45 can be re-written as Eq. 46, which compares the compression ratio $r_{c,i} = 18.9$ and $r_{c,f} = 13.8$. Since the initial pressure in both compression regimes is the same (atmospheric), the value of $p_1$ should cancel.

$$\left(\frac{r_{c,i}}{r_{c,f}}\right)^{\gamma} = \frac{p_{2,i}}{p_{2,f}} \qquad (46)$$

If the initial compression ratio of the cylinder was $r_{c,i} = 18.9$, and the final compression ratio was $r_{c,f} = 13.8$, and assuming a specific heat ratio $\gamma$ of between 1.3 and 1.4 ($\gamma_{CH_4} = 1.320$ at 20 °C, and $\gamma_{Dry\,Air} = 1.400$ at 20 °C), the value of $\frac{p_{2,i}}{p_{2,f}}$ should vary between 1.51 and 1.55. This means the peak pressure in the motoring trace for the spark-ignited engine should be ~ 1.5 times the peak for the catalytic engine, which corresponds with the peak pressure measurements of 30 bar / 20 bar = 1.5.

The engine was first tested with atmospheric exhaust pressure. This was performed across a range of intake pressures and equivalence ratios to determine where a stable operating point could be found. At low intake pressure ($p_i = 1.04$ and 1.20, Figures 3-24 and 3-25 respectively), the pressure and temperature (and therefore flame speed) at the time of sparking was too low to achieve stable combustion, as both figures 2demonstrate significant combustion variability and with peak pressures being very close to the motoring trace. Both tests were performed with an equivalence ratio $\phi_M = 2.0$ and 30°C BTDC spark timing. At an intake pressure $p_i = 1.5$ bar, peak pressures rose correspondingly with the intake pressure, though combustion variability did not improve despite the higher pressure and temperature at time of sparking, which would have increased sparking flame speed. This condition was observed for spark timing at 45°, 40° and 35° BTDC. Delayed spark timing reduced the amount of misfire. Misfire can be observed in Figure 3-26a,b as the histogram bar at ~ 28 bar.

$H_2$ and $C_2H_6$ ($x_{H_2} = 5\%$, $x_{C_2H_6} = 10\%$) were added to simulate $H_2$ recycle and $C_2H_6$ in natural gas at $p_i = 1.5$ bar and with $\phi_M = 2.0$ (Figure 3-27) and 2.6 (Figure 3-28) respectively. These two tests were performed with 30° BTDC spark timing. As was demonstrated in previous results, the addition of both compounds increased flame stability due to their high flame speeds and therefore reduced combustion variability. This demonstrated similar peak pressure performance to what was shown with a compression ratio of 18.9. At a higher compression ratio (Figure 3-9) with the same intake composition as that in Figure 3-28, the average peak cylinder pressure fell within the range of 40-50 bar in both cases. In terms of $H_2$ to CO ratio, this was approximately 2.0 in both cases as well. This demonstrated that a demonstration engine with a lower compression ratio of 13.8:1 could achieve similar conditions in the cylinder and in exhaust gas compositions as that with a higher compression ratio of 18.9:1.

A high exhaust back-pressure was enforced on the spark-ignited test cylinder to determine its effect on performance at a compression ratio of 13.8:1. A one-way ball valve was used to throttle the exhaust gases, and the high-pressure gas was forced to travel through a ¼" tube into the exhaust stack. The mass flow controller settings were not changed in any of these cases, and the pressure drop through the controlling valves were high enough in all cases to maintain the desired flow rates. Therefore, the mass flow through the engine would have been the same as without exhaust throttling. As a result of the constant mass flow rate, throttling the exhaust gases also led to an increase in intake pressure as the total flow resistance was increased. This required a larger gas potential (pressure) in the intake manifold to drive the same flow rate through the engine. This test was first performed for an equivalence ratio $\phi_M = 2.0$ ($x_{H_2} = 0\%$, $x_{C_2H_6} = 0\%$) at 35° BTDC spark timing and $p_i = 1.9$ bar and $p_{exh} = 3.0$ bar. This produced peak pressures of $\sim$ 70 bar (Figure 3-29). A second test was first performed for an equivalence ratio $\phi_M = 2.4$ ($x_{H_2} = 5\%$, $x_{C_2H_6} = 10\%$) at 35° BTDC spark timing and $p_i = 1.9$ bar and $p_{exh} = 3.0$ bar. This produced peak pressures of $\sim$ 85 bar (Figure 3-30). The higher peak pressures seen in this latter test were due to the presence of $H_2$ and $C_2H_6$, which increased the chemical energy of the charge. In both cases, combustion stability was significantly improved by exhaust throttling. This was because intake pressures were increased beyond the values tested in atmospheric exhaust tests. Therefore, the flame speed of the gas at the point of sparking for both of these conditions was improved.

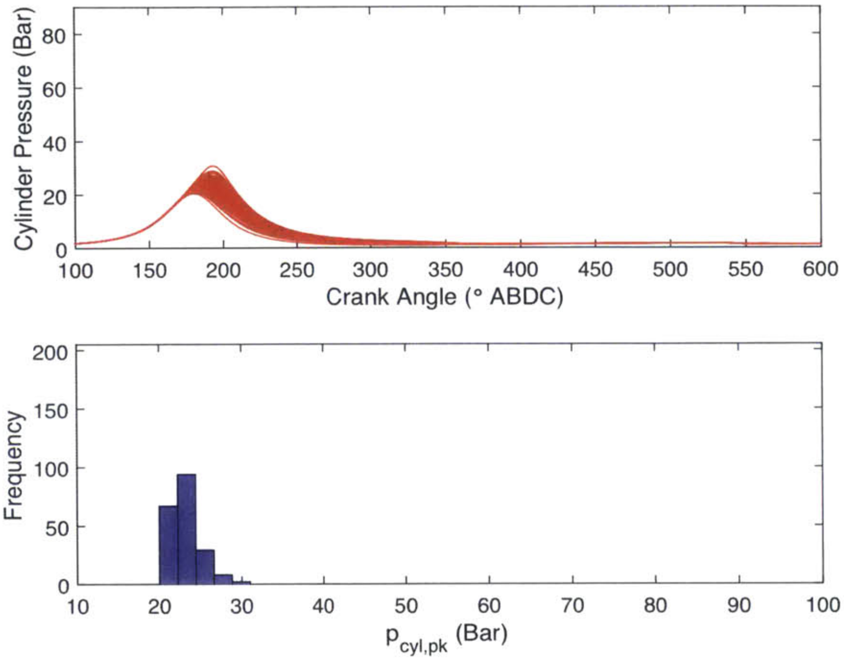

**Figure 3-24.** Cylinder pressure trace and peak pressure histogram of 200 consecutive engine cycles at $\phi_M = 2.0$, $x_{H_2} = 0\%$, $x_{C_2H_6} = 0\%$, $T_i = 394$ °C, $p_i = 1.04$ bar, 30° BTDC spark timing.

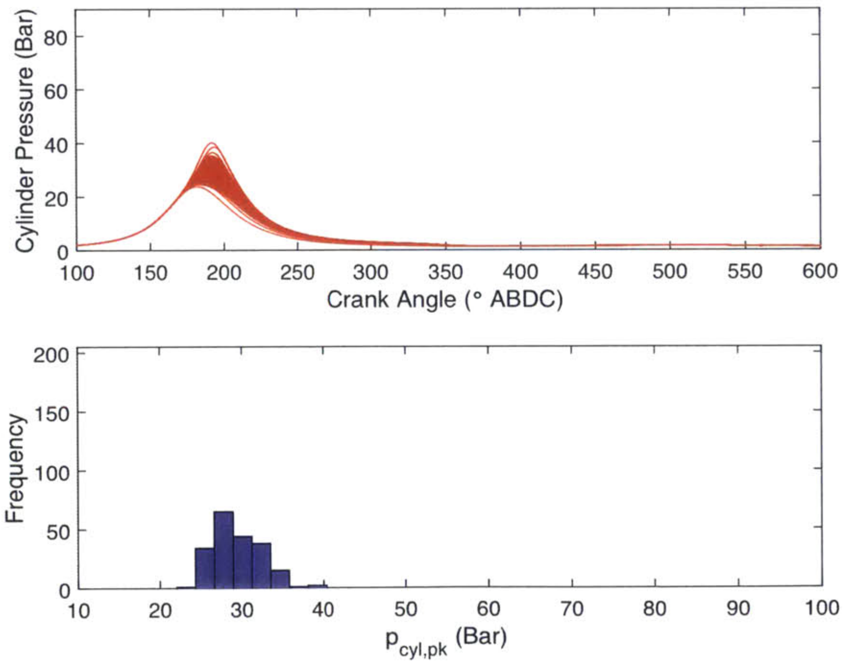

**Figure 3-25.** Cylinder pressure trace and peak pressure histogram of 200 consecutive engine cycles at $\phi_M = 2.0$, $x_{H_2} = 0\%$, $x_{C_2H_6} = 0\%$, $T_i = 424$ °C, $p_i = 1.20$ bar, 30° BTDC spark timing.

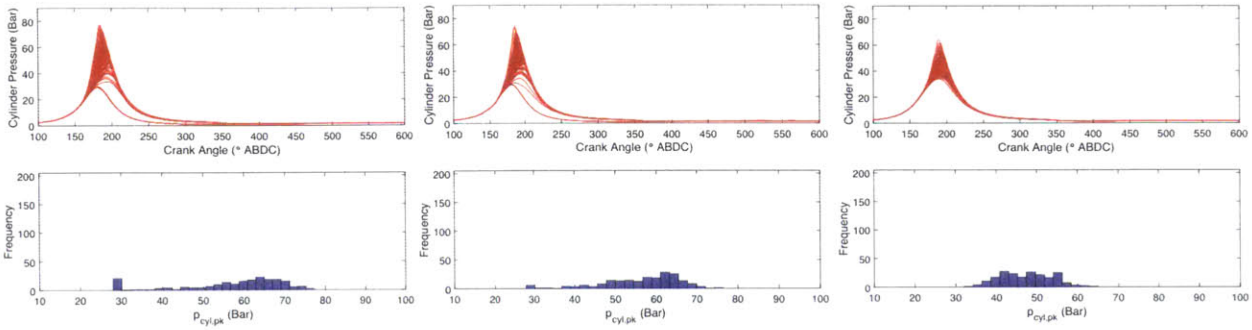

**(a)** **(b)** **(c)**

**Figure 3-26.** Cylinder pressure trace and peak pressure histogram of 200 consecutive engine cycles all at $\phi_M = 2.0$, $x_{H_2} = 0\%$, $x_{C_2H_6} = 0\%$ $T_i = 445$ °C, $p_i = 1.50$ bar, and (a) 45°, (b) 40°, (c) 35° BTDC spark timing.

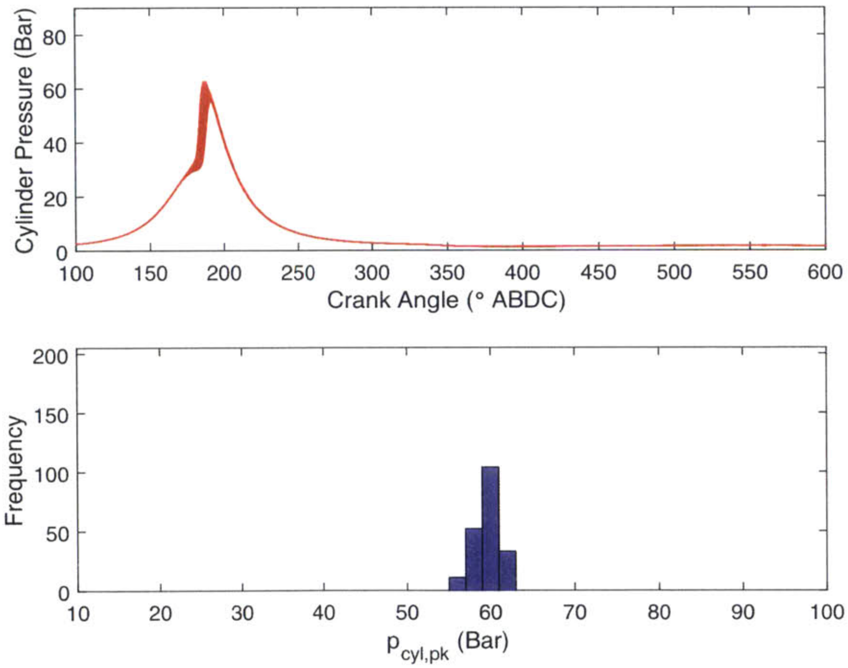

**Figure 3-27.** Cylinder pressure trace and peak pressure histogram of 200 consecutive engine cycles at $\phi_M = 2.0$, $x_{H_2} = 5\%$, $x_{C_2H_6} = 10\%$, $T_i = 470$ °C, $p_i = 1.50$ bar, and 30° BTDC spark timing.

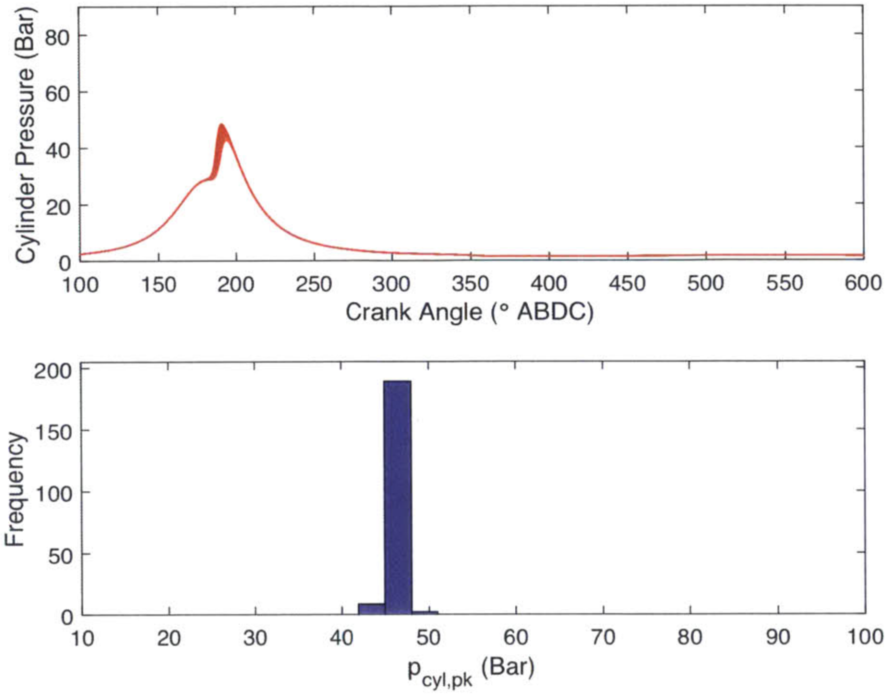

**Figure 3-28.** Cylinder pressure trace and peak pressure histogram of 200 consecutive engine cycles at $\phi_M = 2.6$, $x_{H_2} = 5\%$, $x_{C_2H_6} = 10\%$, $T_i = 490$ °C, $p_i = 1.50$ bar, and 30° BTDC spark timing.

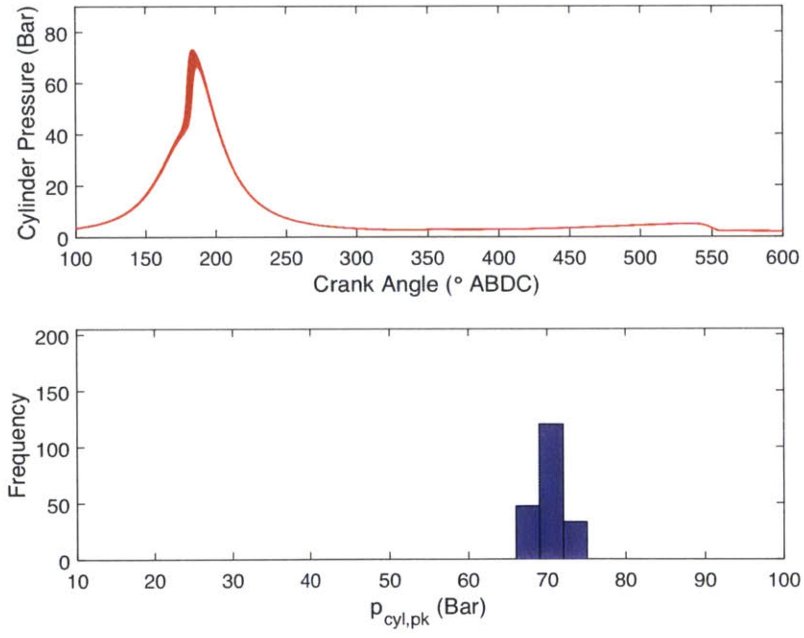

**Figure 3-29.** Cylinder pressure trace and peak pressure histogram of 200 consecutive engine cycles at $\phi_M = 2.0$, $x_{H_2} = 0\%$, $x_{C_2H_6} = 0\%$, $T_i = 430$ °C, $p_i = 1.90$ bar, $p_{exh} = 3.0$ bar and 35° BTDC spark timing.

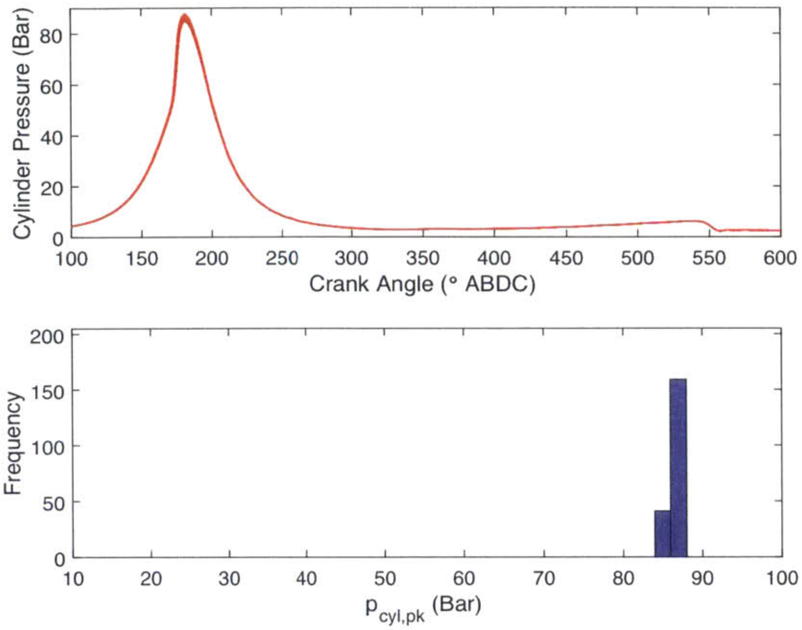

**Figure 3-30.** Cylinder pressure trace and peak pressure histogram of 200 consecutive engine cycles at $\phi_M = 2.4$, $x_{H_2} = 5\%$, $x_{C_2H_6} = 10\%$, $T_i = 430$ °C, $p_i = 1.90$ bar, $p_{exh} = 3.0$ bar and 35° BTDC spark timing.

# 4. Results & Discussion: Catalytic Partial Oxidation

The catalytic engine was operated with a constant value of $\phi_M = 4.0$. However, the values for $y_{DR}$ and $a_{CO_2}$ (these variables are described in section 2.1.2) were tested across a range. $y_{DR}$ was tested at 0.5, 1.0 and 1.5. $a_{CO_2}$ was tested at 1.0, 3.0 and 5.0. The intake temperature was increased to ~ 140 °C, at which point the catalyst achieved "light-off". This means that the catalyst active sites reached an average temperature that was high enough to promote catalytic methane partial oxidation. This released heat from the reaction, and improved the catalyst performance further. Therefore, there was a steep rise in exhaust temperature when light-off occurred (Figure 4-1). Subsequent to light-off, the exhaust temperature eventually reached steady-state (this is reached beyond what is shown in Figure 4-1). Steady-state conditions were always met when data was acquired.

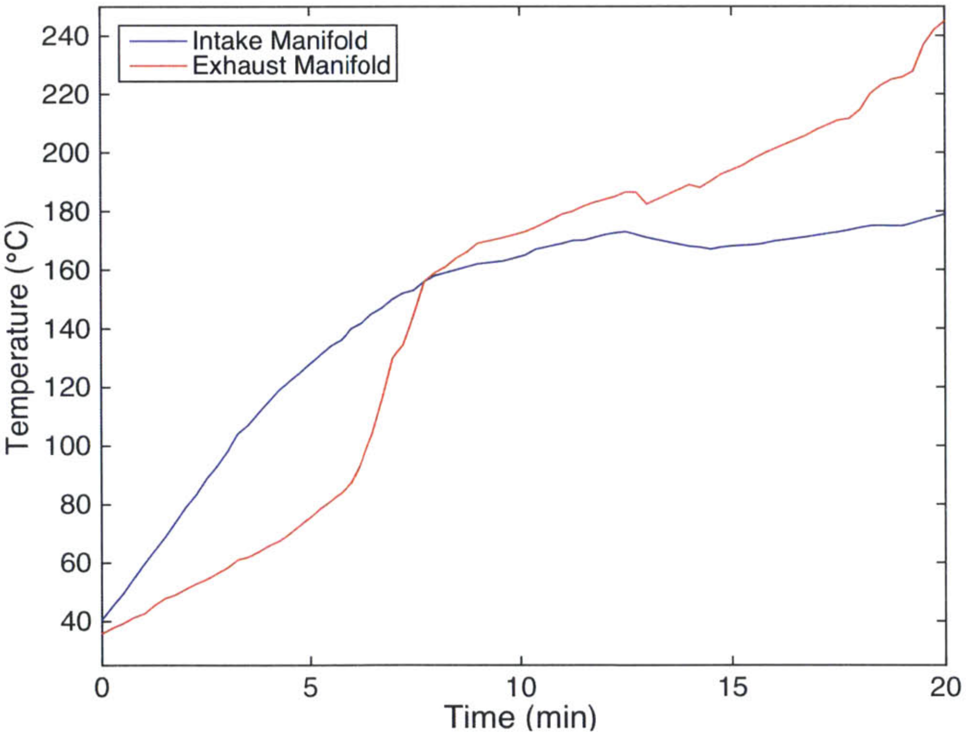

**Figure 4-1.** Intake and exhaust manifold temperatures as a function of time during "light-off" procedure. The intake composition was held constant with $\phi_M = 4.0$, $y_{DR} = 0.5$, and $a_{CO_2} = 3$.

## 4.1. Syngas Quality

The effects of $y_{DR}$ and $a_{CO_2}$ on syngas $H_2$ to CO ratio was negative. Excessive quantities of $CO_2$ led to a reduction in the $H_2$ to CO ratio of the exhaust syngas. This effect was especially pronounced for $y_{DR} = 1.5$ and $a_{CO_2} = 5.0$, where partial oxidation did not occur (Figure 4-2).

The quality of syngas that was produced from the engine had a maximum $H_2$ to CO ratio of 1.0 (Figure 4-2). This was one half of the ideal value of 2.0 that is possible with methane partial oxidation (POX). The ideal $H_2$ to CO ratio for methane dry reforming is 1.0. The intake mixtures that were reacted in the engine were a combination of both POX and dry reforming. Therefore, if both reactions proceeded to completion, depending on the relative stoichiometry of POX and dry reforming, the expected exhaust $H_2$ to CO ratio should have been between 1.0 and 2.0. These results show values that are lower than this, suggesting that there was a mechanism that was consuming $H_2$ in the process.

There are two likely ways for $H_2$ to be consumed that would have resulted in this reduction. First, $H_2$ may have reacted with $O_2$ to produce $H_2O$. Second, $H_2$ may have reacted with $CO_2$ in reverse water-gas shift to produce $H_2O$ and CO. Both would have led to a reduction in the $H_2$ to CO ratio. This is discussed in the following section.

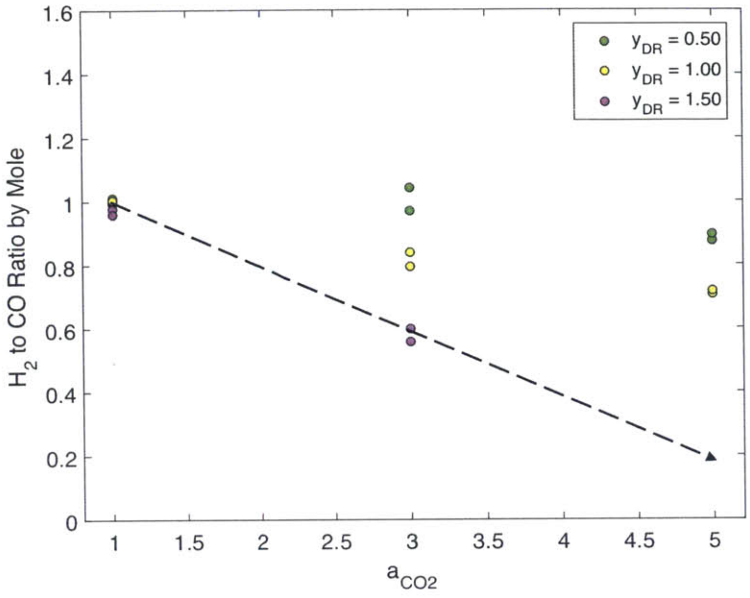

**Figure 4-2.** $H_2$ to CO ratio by mole in engine exhaust, for different partial oxidation mixtures ($\phi_M = 4.0$) with varying amounts of dry reforming ($y_{DR}$) and excess $CO_2$ ($a_{CO_2}$). Note that at $y_{DR} = 1.5$, $a_{CO_2} = 5.0$, a negligible amount of $H_2$ and CO were produced so the value of the $H_2$ to CO ratio is not defined.

## 4.2. Methane Conversion

The peak methane conversion was ~ 20% (Figure 4-3). The conversion was a strong function of $y_{DR}$, where larger values of $y_{DR}$ led to a reduction in conversion. It was also a strong function of $a_{CO_2}$, especially at high values of $y_{DR}$. The reduction in the methane conversion efficiency that was brought about by increasing the value of $a_{CO_2}$ was likely a result of the increase in diluent fraction in the mixture, and therefore an increase in quenching of the chemical reaction. The volume of the charge at TDC that was contained within the catalytic foam was calculated to be ~ 44%. Therefore, in the best conditions that were tested, ~ 45% of the methane that was within the vicinity of the catalyst was reacted (~ 20% overall). The catalytic foam had a diameter of 5 cm and height of 1.26 cm. Therefore, the total contained volume was 24.74 $cm^3$. Based on the Fecralloy® density of 7.22 $g/cm^3$ [61], the mass of the foam was calculated to be 9.05 g. The solid and bulk volumes of the foam were therefore 1.25 $cm^3$ and 23.49 $cm^3$ respectively. Based on the geometry of the cylinder, the bulk volume as a percentage of the clearance volume at TDC was found to be 44%. Therefore, if the only $CH_4$ that was able to react was in the vicinity of the catalytic foam, only 45% of this $CH_4$ actually reacted. This suggests that the $CH_4$ was mass transport limited, as a significant portion of the $CH_4$ was not close enough to the catalyst to react.

At the same time, the ratios of $CO_2$ in the exhaust gases to those in the intake were greater than 1. This is quantified by the $CO_2$ production efficiency in Figure 4-4. It is a ratio of the number of moles of $CO_2$ in the exhaust relative to the number of moles that were supplied in the intake, expressed as a percentage. All of this was performed by normalizing to the number of $N_2$ that went through the engine, which was held constant.

To diagnose these results, first, the difference between the number of moles of $CO_2$ in the exhaust and intake was determined. Then, the number of moles of $CH_4$ that was converted to $CO_2$ was calculated by subtracting the number of moles of leftover $CH_4$ and CO in the exhaust, from the number of moles of intake $CH_4$. So long as reasonable $CH_4$ conversion efficiencies were achieved, which is the case for the data shown here, the ratio between these two numbers would have demonstrated whether the intake $CO_2$ participated in any chemistry inside the cylinder. If this ratio were 1.0, then the intake $CO_2$ was inert. The values for this ratio were calculated to be between 0.35 and 1.0 for the data shown below. This showed that some intake $CO_2$ was consumed, most likely for both methane dry reforming and reverse water gas shift.

The conversion efficiency of $O_2$ was also calculated (Figure 4-5) to compare with that of $CH_4$. A 1:1 correspondence between these two conversion efficiencies would have suggested that the mass-transport limitations that are described above for $CH_4$ were also true for $O_2$. However, these values were approximately two times larger than those of $CH_4$. This suggests that additional $O_2$ was consumed, most likely in the reaction of $H_2$ or CO, as the autoignition of both (560 °C [62] and 630 °C [63]) were both within the range of the peak cylinder temperatures. These temperatures were modeled assuming isentropic compression and found to be in the vicinity of 1800 K at TDC. Future work will focus on consolidating a numerical model with these experimental results.

To demonstrate that bulk diffusion of gases from the clearance volume above the catalyst into the vicinity of the foam was unlikely, the timescale of bulk diffusion into the foam material was calculated to compare with the residence time of the gas in the TDC region. The binary diffusion coefficient for $CH_4$ in $N_2$ ($D_{CH_4-N_2}$) in the 10-30 bar and 500-3000 K range was calculated to be 1 – 4 $cm^2/s$. Based on the diffusion timescale ($\tau_D$) approximation $\tau_D = \frac{L^2}{2D_{ij}}$, where $L$ is the diffusion length scale and $D_{ij}$ is the binary diffusion coefficient between two species, and based on a diffusion length scale of ~ 0.5 cm at TDC, the value of $\tau_D$ can range from 62.5 to 250 ms. This is approximately one to two orders of magnitude larger than the time that the engine spent near TDC, which is on the order of 1 to 10 ms at an engine engine speed of 563 rpm. This suggests that mass-transport into the vicinity of the catalytic foam was unlikely. Therefore, all of the chemistry was occurring with reactants in the foam region.

In order to perform checks and balances on the different elements involved in the reaction, the exhaust products that were not accounted for in the GC were assumed to be water. The moles of H and O that were therefore unaccounted for from the intake were calculated. This was found to occur in a ratio of 2 to 1, which is consistent with $H_2O$.

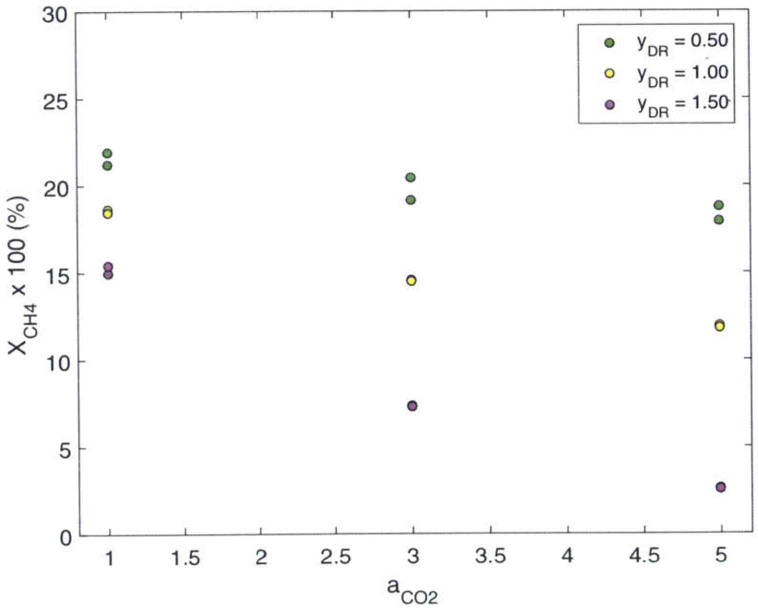

**Figure 4-3.** $CH_4$ conversion efficiencies ($X_{CH_4}$) in engine exhaust expressed as a percentage, for different partial oxidation mixtures ($\phi_M = 4.0$) with varying amounts of dry reforming ($y_{DR}$) and excess $CO_2$ ($a_{CO_2}$).

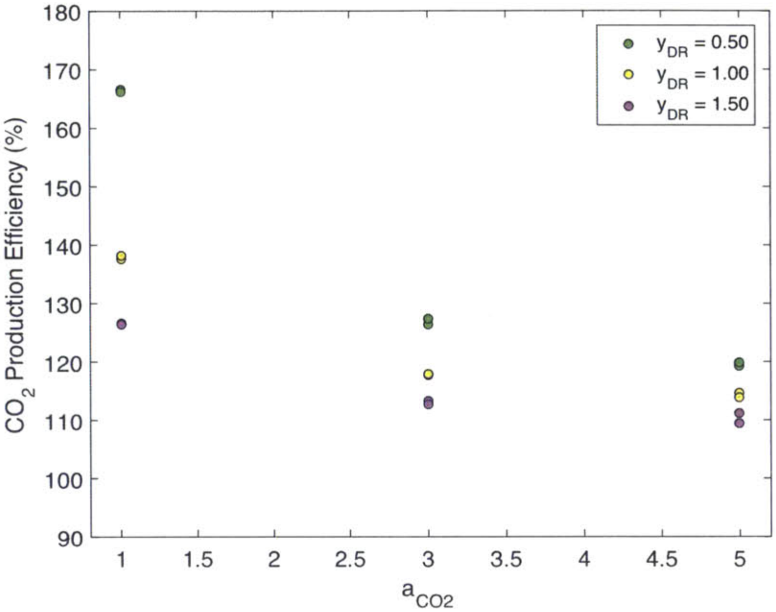

**Figure 4-4.** $CO_2$ production efficiencies ($CO_{2,Bal}$) in engine exhaust expressed as a percentage, for different partial oxidation mixtures ($\phi_M = 4.0$) with varying amounts of dry reforming ($y_{DR}$) and excess $CO_2$ ($a_{CO_2}$). This demonstrates the relative amount of $CO_2$ that was produced in the reaction between exhaust and intake. Values > 100% mean that there was net $CO_2$ production.

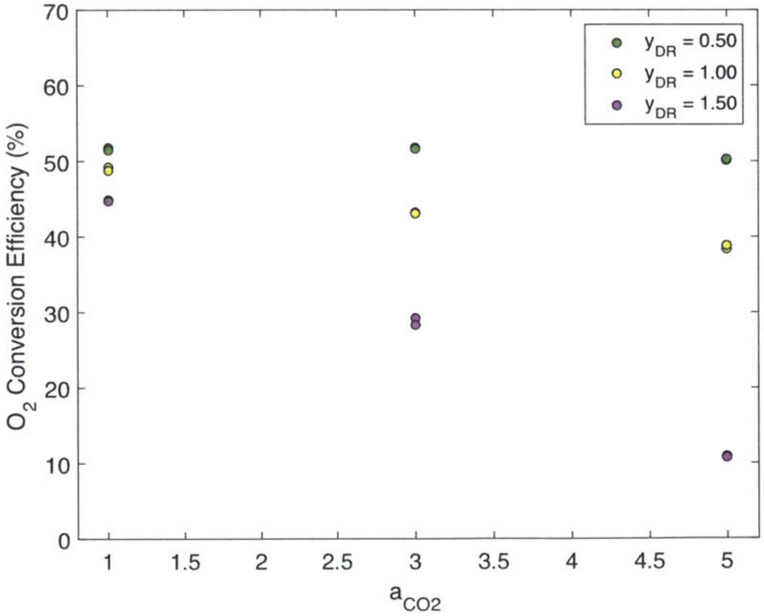

**Figure 4-5.** $O_2$ conversion efficiencies ($X_{O_2}$) in engine exhaust expressed as a percentage, for different partial oxidation mixtures ($\phi_M = 4.0$) with varying amounts of dry reforming ($y_{DR}$) and excess $CO_2$ ($a_{CO_2}$).

# 5. Conclusions

This thesis has demonstrated the reliable operating regimes of two engine reformers using atmospheric air for the production of syngas. Spark-ignition and catalytic routes for methane partial oxidation were both successfully tested in diesel engine cylinders. The following concluding observations were made:

*Spark-Ignited Partial Oxidation*:

- Methane partial oxidation with high (> 85%) conversion efficiencies of methane was shown to be possible in spark-ignited diesel cylinders with compression ratios of 18.9:1 and 13.8:1.
- Intake temperatures > 350 °C were shown to be sufficient to reach stable combustion with room air, at methane-air equivalence ratios $\phi_M$ up to 2.0.
- Spark timing at 30° BTDC provided significant improvements to combustion stability when compared to more advanced timing.
- Exhaust soot concentrations were excessive above a hydrocarbon-air equivalence ratio of 2.2 (> 0.18 mg/L). Lower intake temperatures did not serve to reduce the concentration of exhaust soot than at higher temperatures, as lower temperatures did not allow soot to be oxidized as effectively.
- A hydrocarbon-air equivalence ratio $\phi_{HC}$ of 2.2 with 5% $H_2$ recycle from downstream processes provided an acceptable balance of high $H_2$ to CO ratio (~ 1.8), high $CH_4$ conversion efficiency (~ 85%), and low exhaust soot concentration (~ 0.18 mg/L). At lower equivalence ratios than this, a dramatic reduction in $H_2$ to CO ratio was observed, which would have required significant water-gas shift to boost this ratio closer to 2.0. At equivalence ratios higher than this, a significant reduction in $CH_4$ conversion efficiency was observed, as well as large quantities of soot production (> 0.18 mg/L).
- In deploying this technology on a larger scale, a tradeoff will occur between high $H_2$ to CO ratio close to 2.0, and $CH_4$ conversion efficiency. The former is only possible at high (> 2.2) hydrocarbon-air equivalence ratios, while the latter tends to be reduced at these equivalence ratios.

- Similar engine performance was achievable at a lower compression ratio of 13.8:1 (as compared to 18.9:1) with the help of boosting intake absolute pressures to 1.5 bar, or throttling exhaust pressures to 3.0 bar (and hence intake pressures to close to 2.0 bar).

*Catalytic Partial Oxidation*:

- A compression ratio of 15.5:1 and ~ 150 °C intake temperatures were sufficient to trigger light-off for a Pd catalyst in an $Al_2O_3$ washcoat that was deposited on a Fecralloy metallic foam.
- Methane-air equivalence ratios $\phi_M = 4.0$ and varying amounts of methane dry reforming produced $H_2$ to CO ratios up to 1.0, $CH_4$ conversion efficiencies up to 20%, and $O_2$ conversion efficiencies up to 50%. A combination of $H_2$ oxidation and $CO_2$ reverse water-gas shift were attributed to the non-ideal $H_2$ to CO ratio, which is 2.0 in ideal partial oxidation stoichiometry.
- A net production of $CO_2$ was observed through the engine. This was attributed to $CH_4$ combustion occurring in the cylinder. Since bulk diffusion was found to have longer timescales than the residence time of the gases near TDC, the $CH_4$ combustion was likely a surface phenomenon occurring on the Pd active sites. The Pd catalyst is known to perform methane combustion and partial oxidation in sequence.
- Simultaneously performing $CO_2$ dry reforming is not an ideal strategy due to the preferential shift to CO production as a result of excess $CO_2$ via the reverse water-gas shift reaction.
- In future tests, $H_2O$ will be injected to perform methane steam reforming and to reduce soot formation by preferentially oxidizing CO, and $N_2$ will be added to serve as a diluent to buffer the heat release from methane partial oxidation.

# 6. Future Work

*Spark-Ignited Engine*:

The results presented here from the spark-ignited engine will be used to design a larger engine that will serve in a demonstration plant in North Carolina. This will be funded by an ARPA-e award of $3,872,297 from the OPEN 2012 program, which is titled "Compact, Inexpensive Micro-Reformers for Distributed GTL". This program will eventually lead to the construction of a pilot-scale plant that will serve as a prototype for the skid-mounted units that is the intended end design (Figure 6-1).

In future engine tests, a high power ignition system will be installed to improve the spark-ignition energy and therefore improve engine performance at highly fuel-rich regimes. Also, ethane-rich and pure ethane mixtures will be tested to simulate natural gas mixtures with extremely high concentrations of ethane, as well as to attempt ethane cracking in the cylinder. Finally, high concentrations of oxygen in the oxidizer will be tested to measure the improvement in engine performance, and to simulate the effect of adding an air separation unit (ASU) to the system to increasing methane processing throughout.

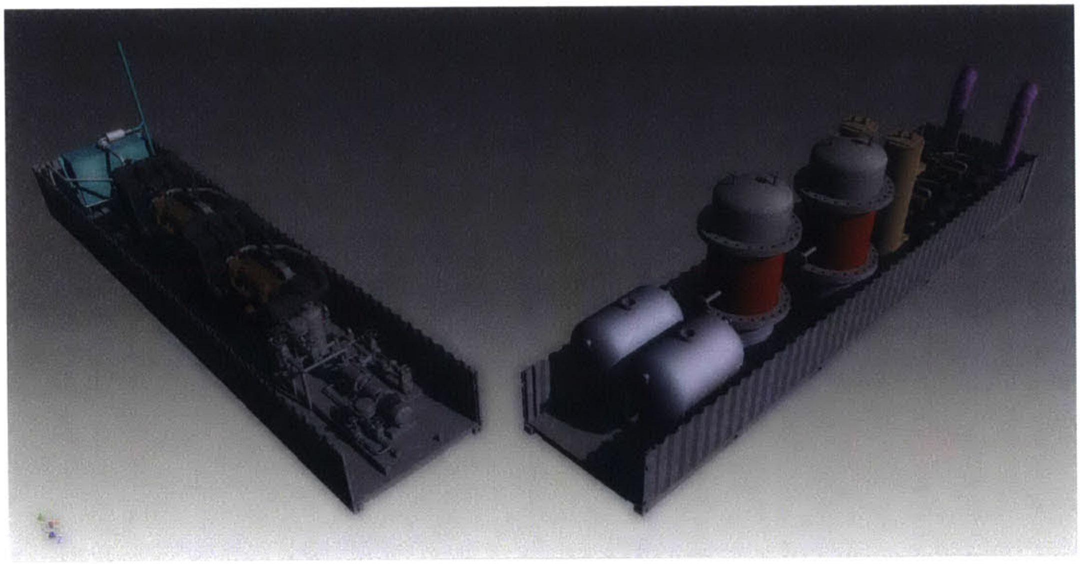

**Figure 6-1.** An artistic rendering of the skid-mounted system that can be used at remote, stranded gas sites to synthesize liquid fuels for quick and easy transportation.

*Catalytic Engine*:

The addition of $CO_2$ in the catalytic engine led to the promotion of the reverse water-gas shift reaction and the reduction in exhaust $H_2$ to CO ratio. Therefore, future tests will eliminate $CO_2$ entirely from the intake and will explore the effect of adding vaporized $H_2O$ and $N_2$. The addition of $H_2O$ should lead to some $CH_4$ steam reforming and potentially an increase in the $H_2$ to CO ratio, as the steam reforming products are $H_2$ and CO with a 3:1 ratio. Furthermore, $H_2O$ should reduce the amount of soot production. $N_2$ should serve as an inert diluent similar to $CO_2$, though without participating in the chemical reaction. Too much of either compound will cool the charge too much and prevent the catalyst from operating effectively, similar to the way too much $CO_2$ reduced $CH_4$ conversion.

# 7. References

[1] Heywood, J., 1988, Internal Combustion Engine Fundamentals, McGraw-Hill Education.

[2] Rostrup-Nielsen, J., and Christiansen, L. J., 2011, Concepts in Syngas Manufacture, World Scientific.

[3] Rostrup-Nielsen, J. R., Sehested, J., and Nørskov, J. K., 2002, "Hydrogen and synthesis gas by steam- and C02 reforming," B.-A. in Catalysis, ed., Academic Press, pp. 65–139.

[4] Enger, B. C., Lødeng, R., and Holmen, A., 2008, "A review of catalytic partial oxidation of methane to synthesis gas with emphasis on reaction mechanisms over transition metal catalysts," Appl. Catal. Gen., **346**(1), pp. 1–27.

[5] Hickman, D. A., and Schmidt, L. D., 1993, "Production of Syngas by Direct Catalytic Oxidation of Methane," Science, **259**(5093), pp. 343–346.

[6] Van Looij, F., Stobbe, E. R., and Geus, J. W., 1998, "Mechanism of the partial oxidation of methane to synthesis gas over Pd," Catal. Lett., **50**(1-2), pp. 59–67.

[7] Acocella, A., Lim, E., Cedrone, K., Bromberg, L., Seethamraju, S., Cohn, D., and Green, W., 2014, "System and Market Analysis of Methanol Production Using Compact Engine Reformers," ASME 2014 8th International Conference on Energy Sustainability collocated with the ASME 2014 12th International Conference on Fuel Cell Science, Engineering and Technology, American Society of Mechanical Engineers, pp. V002T03A005–V002T03A005.

[8] 1985, "3.5.4.1 Partial Oxidation of Oil and Gas Feedstocks," Ullmanns Encycl. Ind. Chem., **A2**, pp. 213–215.

[9] Vogel, W., 1963, "The Shell gasification process, a proven industrial tool for synthesis gas production from oil products," World Petroleum Congress.

[10] Rostrup-Nielsen, J. R., and Hansen, J. H. B., 1993, "CO2-Reforming of Methane over Transition Metals," J. Catal., **144**(1), pp. 38–49.

[11] Richardson, J. T., Garrait, M., and Hung, J.-K., 2003, "Carbon dioxide reforming with Rh and Pt–Re catalysts dispersed on ceramic foam supports," Appl. Catal. Gen., **255**(1), pp. 69–82.

[12] Attanasi, E. D., and Freeman, P. A., 2013, Role of stranded gas in increasing global gas supplies, US Department of the Interior, US Geological Survey.

[13] Khalilpour, R., and Karimi, I. A., 2012, "Evaluation of utilization alternatives for stranded natural gas," Energy, **40**(1), pp. 317–328.

[14] U.S. Energy Information Administration, "Proved Reserves of Natural Gas (Trillion Cubic Feet)."

[15] IHS Incorporated, 2007, International Petroleum Exploration and Production Database, IHS Incorporated, Englewood, CO.

[16] U.S. Energy Information Administration, 2014, Proved Nonproducing Reserves (Product: Associated Gas).

[17] U.S. Energy Information Administration, 2015, Natural Gas Gross Withdrawals and Production (Vented and Flared).

[18] U.S. Energy Information Administration, 2011, "Over one-third of natural gas produced in North Dakota is flared or otherwise not marketed."

[19] North Dakota Industrial Commission, Department of Mineral Resources, Oil and Gas Division, "Historic Monthly Gas Production and Sales Statistics."

[20] Sunil Bharati, and L. Sridharan, 2015, "Cairn India, Gurgaon, Haryana, India."
[21] Jaimin Shah, Ramesh Bhatia, and Gurpreet Chugh, 2015, "Jubilant Energy, ICF International, Noida, Uttar Pradesh, India."
[22] Sumit N. Jha, 2015, "GAIL India, Noida, Uttar Pradesh, India."
[23] "Assam Petrochemicals Limited."
[24] AutoNavi, and Google, "Assam, India."
[25] Anand Vatsa, 2014, .
[26] Fleisch, T. H., Basu, A., and Sills, R. A., 2012, "Introduction and advancement of a new clean global fuel: The status of DME developments in China and beyond," J. Nat. Gas Sci. Eng., **9**, pp. 94–107.
[27] Holmen, A., 2009, "Direct conversion of methane to fuels and chemicals," Catal. Today, **142**(1–2), pp. 2–8.
[28] Lunsford, J. H., 2000, "Catalytic conversion of methane to more useful chemicals and fuels: a challenge for the 21st century," Catal. Today, **63**(2–4), pp. 165–174.
[29] Royal Dutch Shell, Pearl GTL.
[30] Ron Sills, "The Dawn of DME as a Transportation Fuel in North America."
[31] U.S. Energy Information Administration, 2010, United States Total Distribution of Wells by Production Rate Bracket.
[32] "Production Units," Oberon Fuels.
[33] The Linde Group, 2007, "Additional Technologies."
[34] Gas Technologies LLC, "The GasTechno® Process."
[35] Malin, J. B., 1951, "Engine generation of synthesis gas."
[36] Otto, H., 1958, "Internal combustion engine for the production of synthesis gas."
[37] Oberdorfer, J. P. E., 1960, "Partial oxidation of methane in a motored engine."
[38] III, L. B., Green, W. H., Sappok, A., Cohn, D. R., and Jalan, A., 2014, "Engine Reformer Systems For Lower Cost, Smaller Scale Manufacturing Of Liquid Fuels."
[39] Ghazi A. Karim, I. W., 2008, "The production of hydrogen through the uncatalyzed partial oxidation of methane in an internal combustion engine," Int. J. Hydrog. Energy, (8), pp. 2105–2110.
[40] Karim, G. A., and Moore, N. P. W., 1990, The Production of Hydrogen by the Partial Oxidation of Methane in a Dual Fuel Engine, SAE International, Warrendale, PA.
[41] Karim, G. A., and Moore, N. P. W., 1990, Examination of Rich Mixture Operation of a Dual Fuel Engine, SAE International, Warrendale, PA.
[42] Hiratsuka, Y., 1963, "Production of synthesis gas by an internal combustion engine," World Petroleum Congress.
[43] Ghaffarpour, M., Lock, A., and Shojaeefard, M., 2004, Partial Oxidation of Natural Gas Using Internal Combustion Engines, SAE International, Warrendale, PA.
[44] McMillian, M. H., and Lawson, S. A., 2006, "Experimental and modeling study of hydrogen/syngas production and particulate emissions from a natural gas-fueled partial oxidation engine," Int. J. Hydrog. Energy, **31**(7), pp. 847–860.
[45] NGK Spark Plugs, "Racing Catalog."
[46] Kistler Group, "High-Temperature Pressure Sensor for Engine Measuring Technology."
[47] Khair, M. K., 1992, "Progress in Diesel Engine Emissions Control," J. Eng. Gas Turbines Power, **114**(3), pp. 568–577.
[48] Magdi K. Khair, and Hannu Jääskeläinen, "Combustion Systems."
[49] BEI Sensors, "H25 Incremental Optical Encoder."

[50] Sappok, A. G. (Alexander G., 2006, "Emissions and in-cylinder combustion characteristics of Fischer-Tropsch and conventional diesel fuels in a modern CI engine," Thesis, Massachusetts Institute of Technology.

[51] Automation Direct, "DURA PULSE AC Drive User Manual."

[52] Randolph, A. L., 1990, Methods of Processing Cylinder-Pressure Transducer Signals to Maximize Data Accuracy, SAE International, Warrendale, PA.

[53] Bromberg, L., 2005, "In-Cylinder Laminar Flame Propagation Speed: Effect of Hydrogen And Hydrogen Rich Gas Addition."

[54] Chaudhuri, S., Wu, F., and Law, C. K., 2013, "Scaling of turbulent flame speed for expanding flames with Markstein diffusion considerations," Phys. Rev. E Stat. Nonlin. Soft Matter Phys., **88**(3), p. 033005.

[55] Kochar, Y., Seitzman, J., Lieuwen, T., Metcalfe, W., Burke, S., Curran, H., Krejci, M., Lowry, W., Petersen, E., and Bourque, G., 2011, "Laminar Flame Speed Measurements and Modeling of Alkane Blends at Elevated Pressures With Various Diluents," pp. 129–140.

[56] Dugger, G. L., 1952, Effect of Initial Mixture Temperature on Flame Speed of Methane-air, Propane-air and Ethylene-air Mixtures, National Advisory Committee for Aeronautics.

[57] Lee, W., and Schaefer, H. J., 1983, Analysis of Local Pressures, Surface Temperatures and Engine Damages under Knock Conditions, SAE International, Warrendale, PA.

[58] Duggal, V. K., Priede, T., and Khan, I. M., 1978, A Study of Pollutant Formation within the Combustion Space of a Diesel Engine, SAE International, Warrendale, PA.

[59] e-CFR: Title 40: Protection of Environment PART 1039—CONTROL OF EMISSIONS FROM NEW AND IN-USE NONROAD COMPRESSION-IGNITION ENGINES Subpart B—Emission Standards and Related Requirements.

[60] Lignell, D. O., Chen, J. H., Smith, P. J., Lu, T., and Law, C. K., 2007, "The effect of flame structure on soot formation and transport in turbulent nonpremixed flames using direct numerical simulation," Combust. Flame, **151**(1–2), pp. 2–28.

[61] GoodFellow, "Fecralloy ® - Iron/Chromium ( Fe72.8/Cr22/Al 5/Y 0.1/Zr 0.1) Material Information."

[62] Air Liquide, "Gas Encyclopedia: Hydrogen."

[63] Air Liquide, "Gas Encyclopedia: Carbon Monoxide."

# Appendix A: Experimental Setup

A schematic describing the experimental setup is shown below.

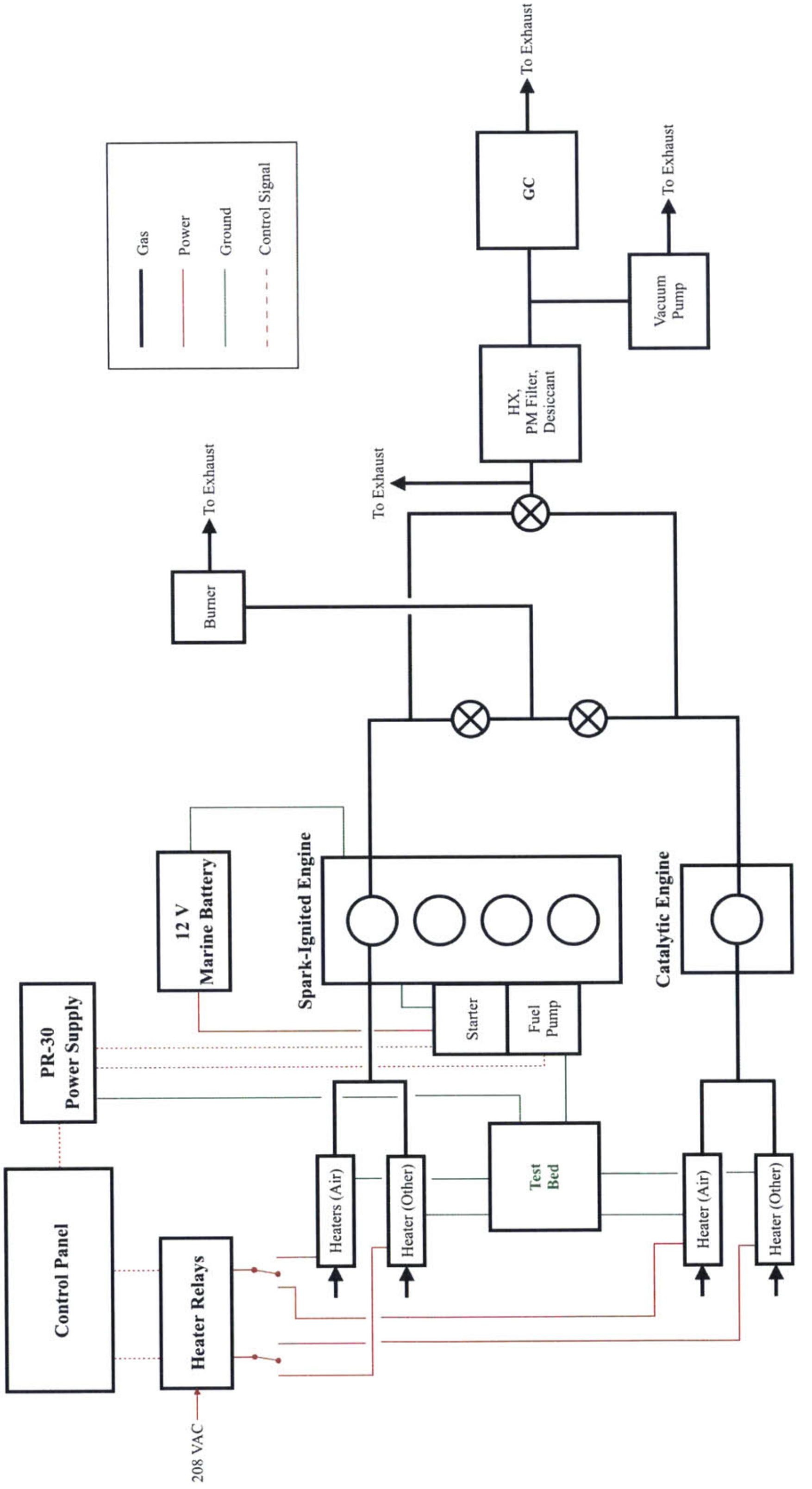

# Appendix B: Measurement and Data Acquisition System

Screenshots of the LabVIEW test VIs that were used to operate auxiliary hardware and capture data are displayed below.

### *Spark-Ignited Engine*

Main VI: Front Panel

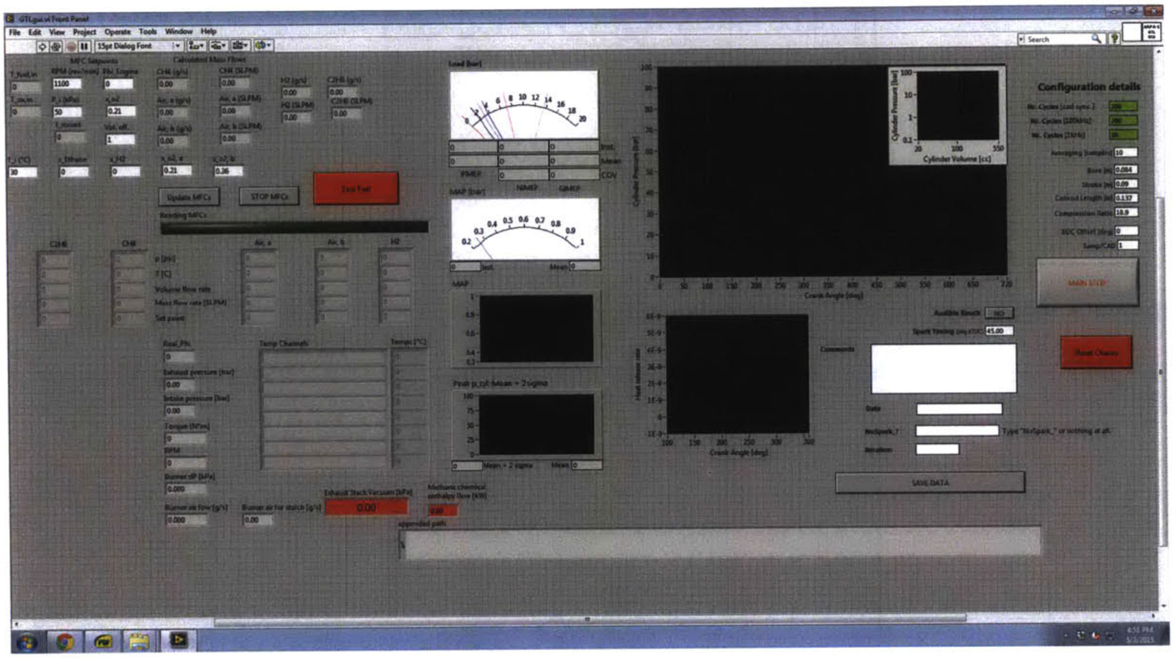

**Configuration details**

Averaging [samples] 10

Bore [m] 0.084

Stroke [m] 0.09

Conrod Length [m] 0.137

Compression Ratio 18.9

BDC Offset [deg] 0

Samp/CAD 1

Audible Knock NO

Spark Timing [deg bTDC] 45.00

Main VI: "Display" Data (Pressures)

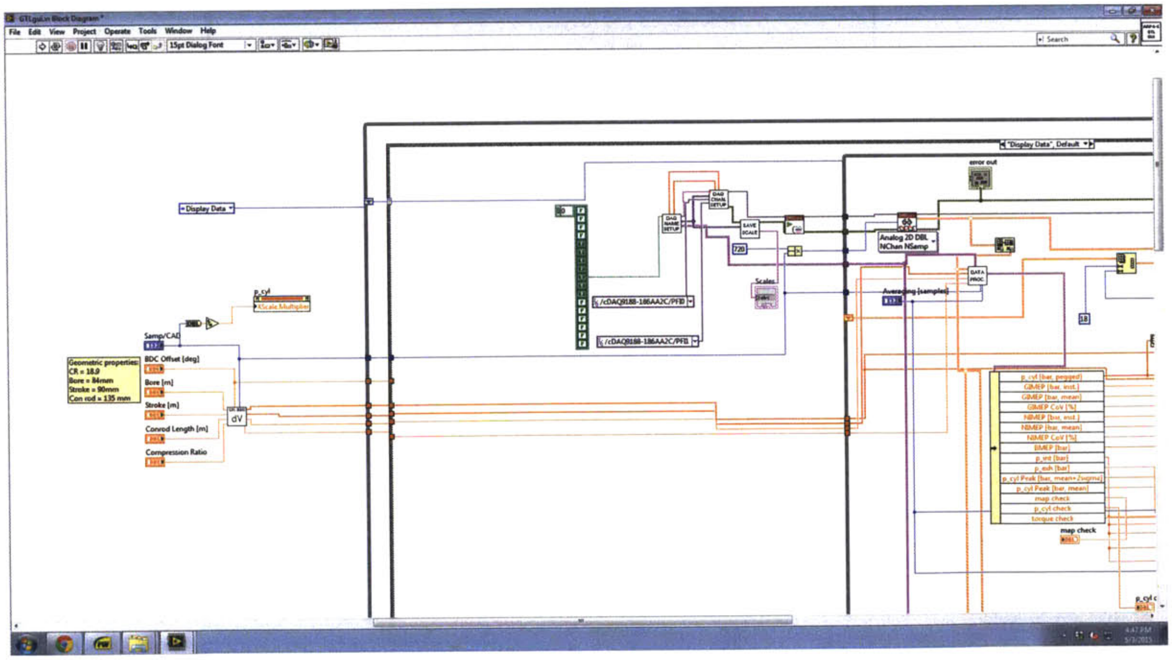

Geometric properties:
CR = 18.9
Bore = 84mm
Stroke = 90mm
Con rod = 135 mm

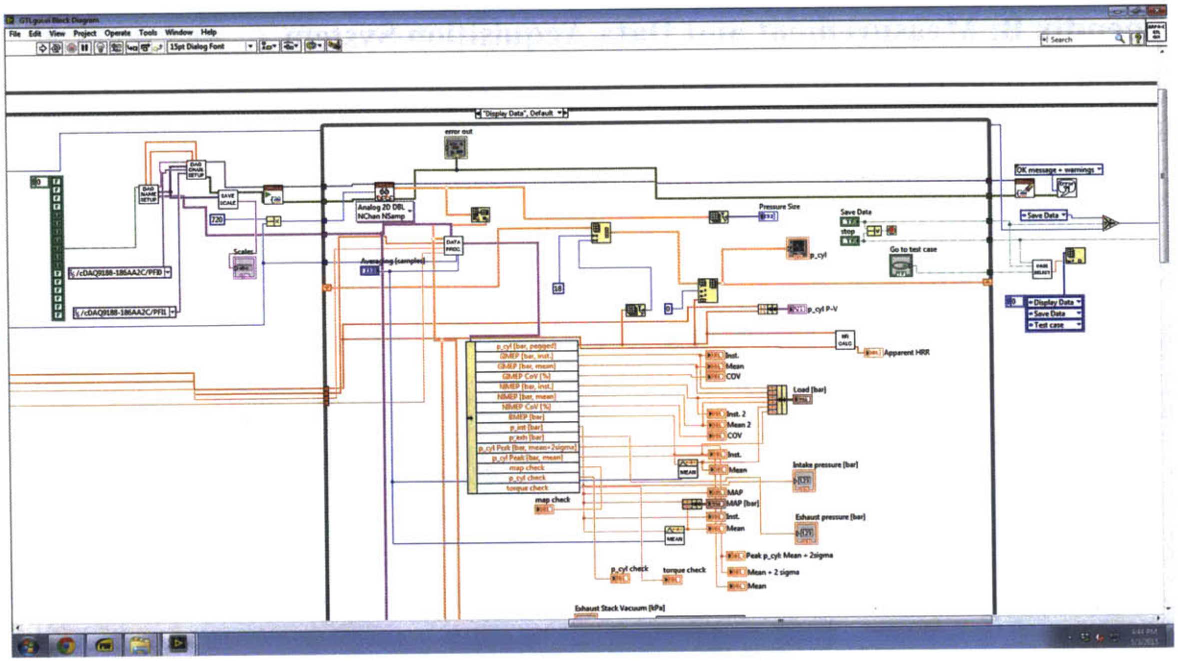
GTLgui.vi Block Diagram
File Edit View Project Operate Tools Window Help
15pt Dialog Font
"Display Data", Default
error out
DAQ CHAN SETUP
SAVE SCALE
720
Scales
Analog 2D DBL NChan NSamp
DATA PROC
Averaging (samples)
Pressure Size
Save Data
stop
Go to test case
p_cyl
p_cyl P-V
HR CALC
Apparent HRR
OK message + warnings
Save Data
Display Data
Save Data
Test case
p_cyl [bar, pegged]
GIMEP [bar, inst.]
GIMEP [bar, mean]
GIMEP CoV [%]
NIMEP [bar, inst.]
NIMEP [bar, mean]
NIMEP CoV [%]
BMEP [bar]
p_int [bar]
p_exh [bar]
p_cyl Peak [bar, mean+2sigma]
p_cyl Peak [bar, mean]
map check
p_cyl check
torque check
Inst.
Mean
COV
Load [bar]
Inst. 2
Mean 2
COV
Inst.
Mean
Intake pressure [bar]
MAP
MAP [bar]
Inst.
Mean
Exhaust pressure [bar]
map check
Peak p_cyl: Mean + 2sigma
Mean + 2 sigma
Mean
p_cyl check
torque check
Exhaust Stack Vacuum [kPa]

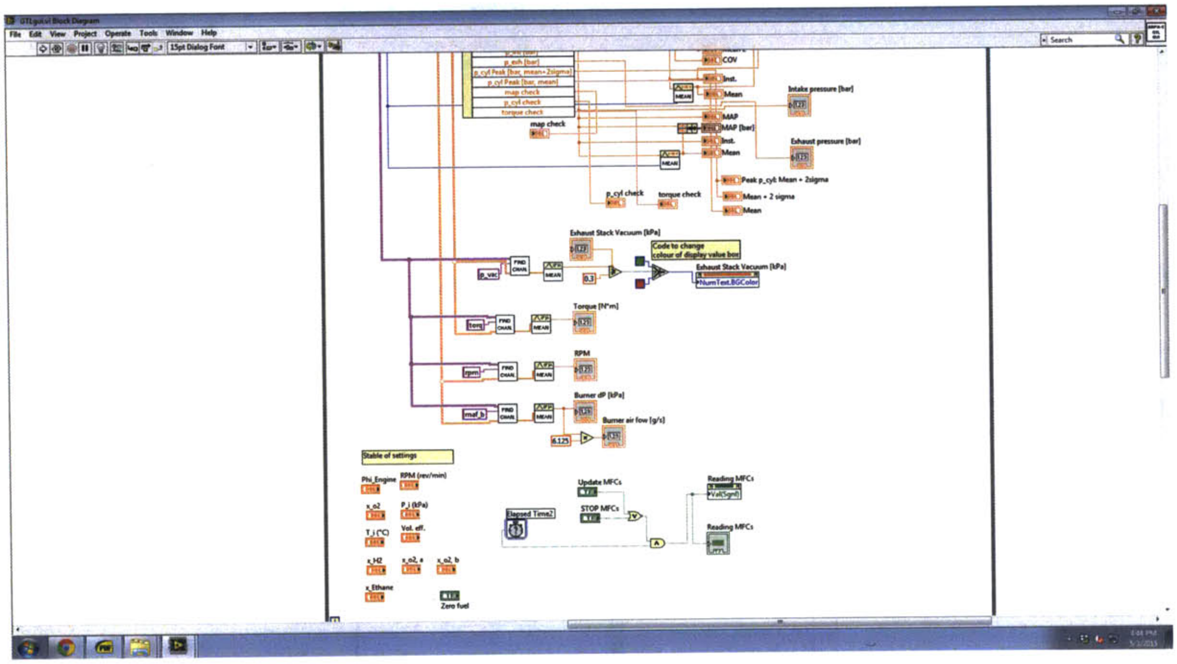
GTLgui.vi Block Diagram
File Edit View Project Operate Tools Window Help
15pt Dialog Font
p_exh [bar]
p_cyl Peak [bar, mean+2sigma]
p_cyl Peak [bar, mean]
map check
p_cyl check
torque check
COV
Inst.
Mean
Intake pressure [bar]
MAP
MAP [bar]
Inst.
Mean
Exhaust pressure [bar]
map check
Peak p_cyl: Mean + 2sigma
Mean + 2 sigma
Mean
p_cyl check
torque check
Exhaust Stack Vacuum [kPa]
p_vac
FIND CHAN
MEAN
0.3
Code to change colour of display value box
Exhaust Stack Vacuum [kPa]
NumText.BGColor
torq
Torque [N*m]
rpm
RPM
maf_b
Burner dP [kPa]
6.125
Burner air fow [g/s]
Stable of settings
Phi_Engine
RPM (rev/min)
x_o2
P_i (kPa)
T_i (°C)
Vol. eff.
x_H2
x_o2, a
x_o2, b
x_Ethane
Zero fuel
Elapsed Time2
Update MFCs
STOP MFCs
Reading MFCs
Val(Sgnl)
Reading MFCs

## Main VI: “Display” Data (Temperatures)

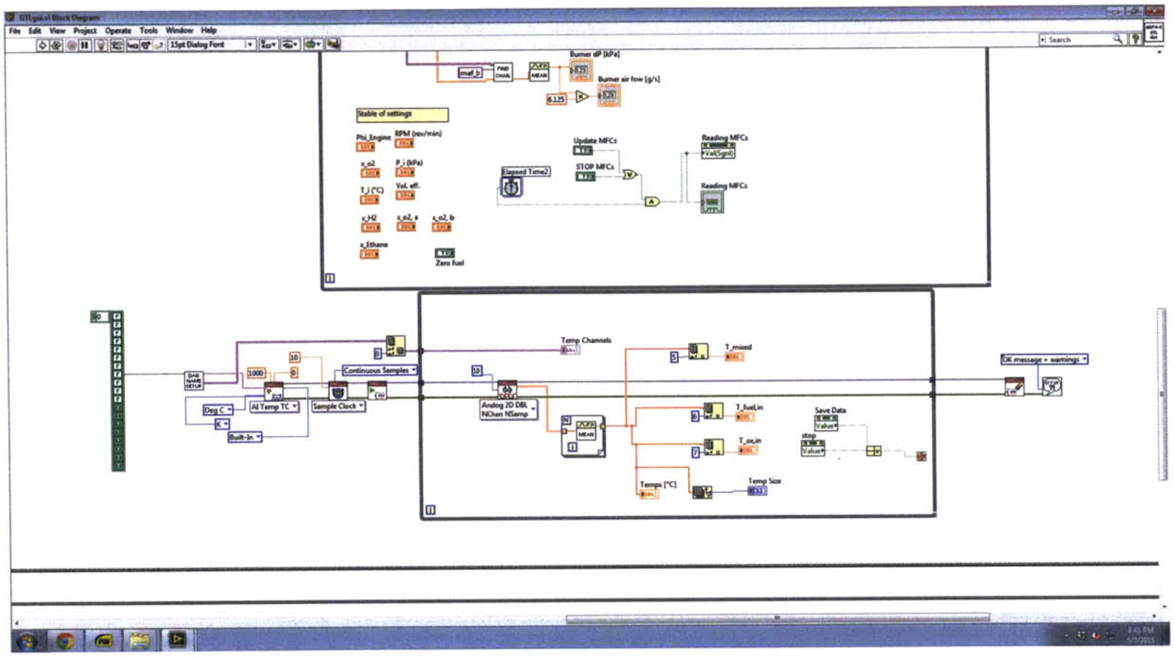

## Main VI: “Save” Data

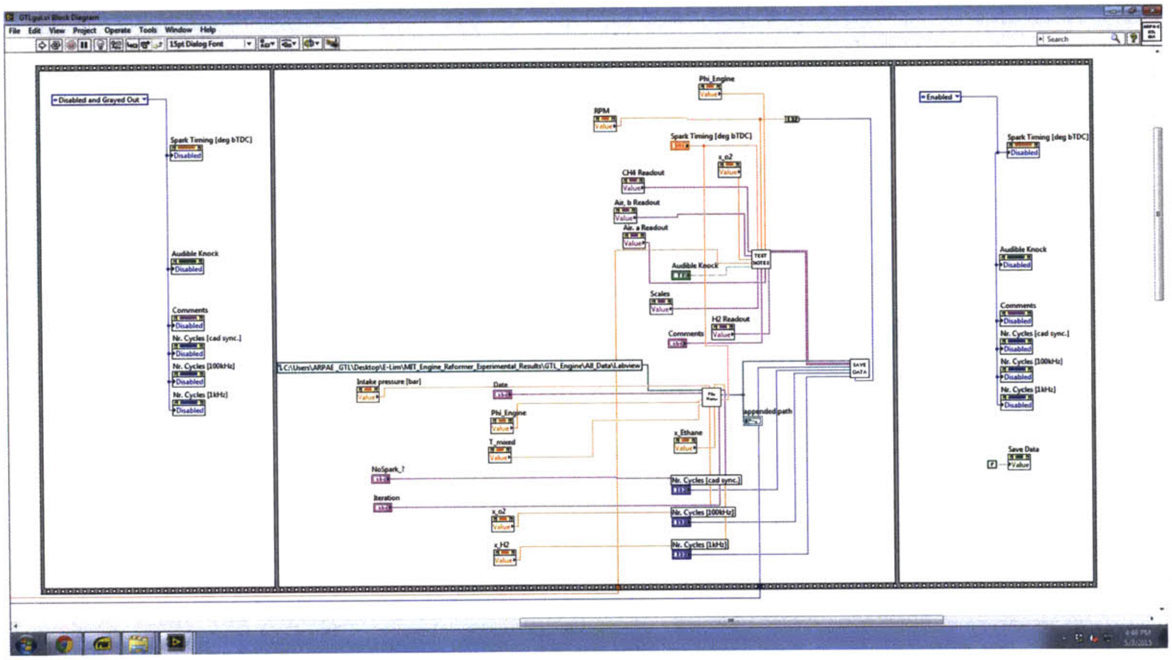

## Main VI: Write to MFCs

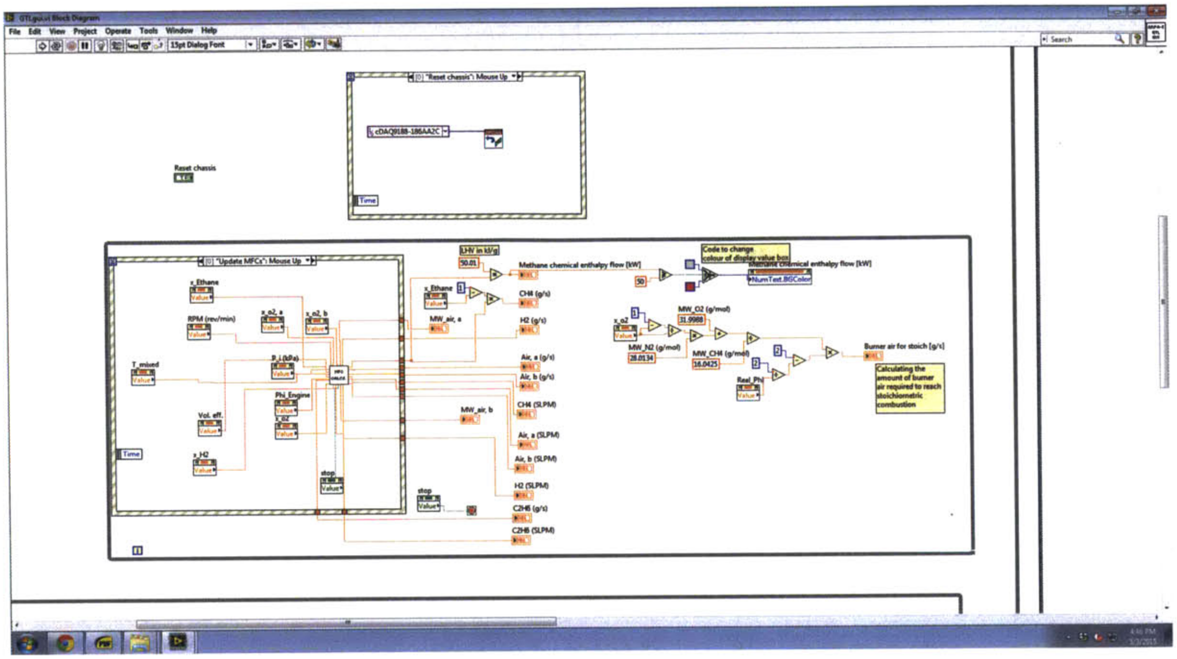

Code to change colour of display value box

Calculating the amount of burner air required to reach stoichiometric combustion

## Main VI: Read from MFCs

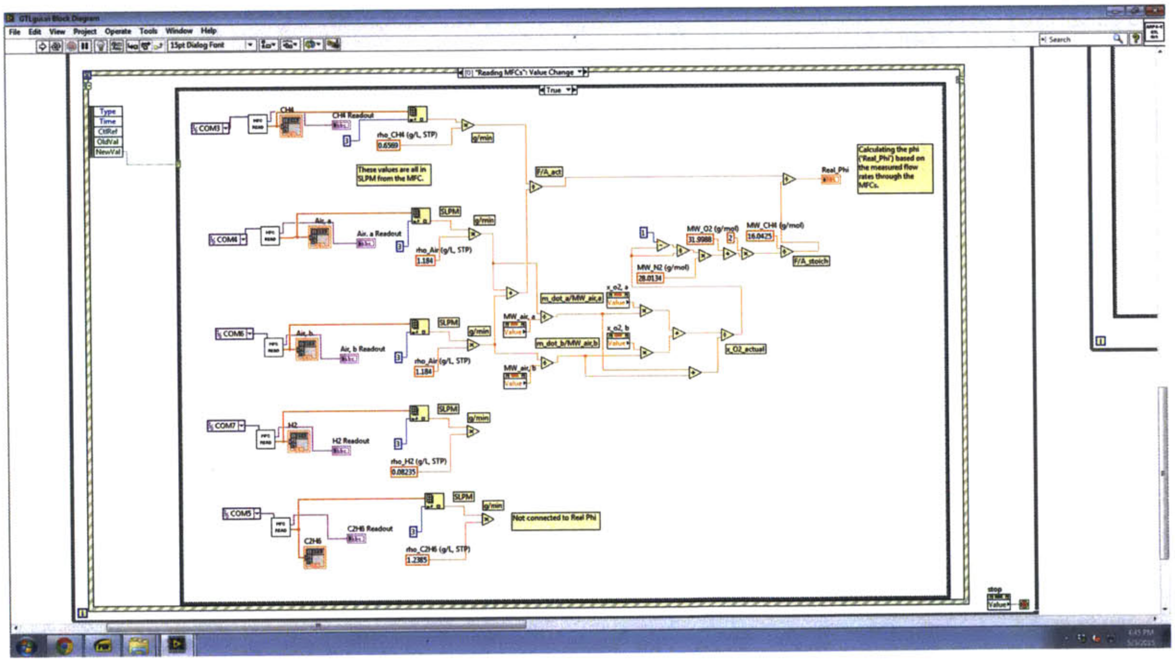

These values are all in SLPM from the MFC.

Calculating the phi ('Real_Phi') based on the measured flow rates through the MFCs.

Not connected to Real Phi

# Sub VI: Write to MFCs

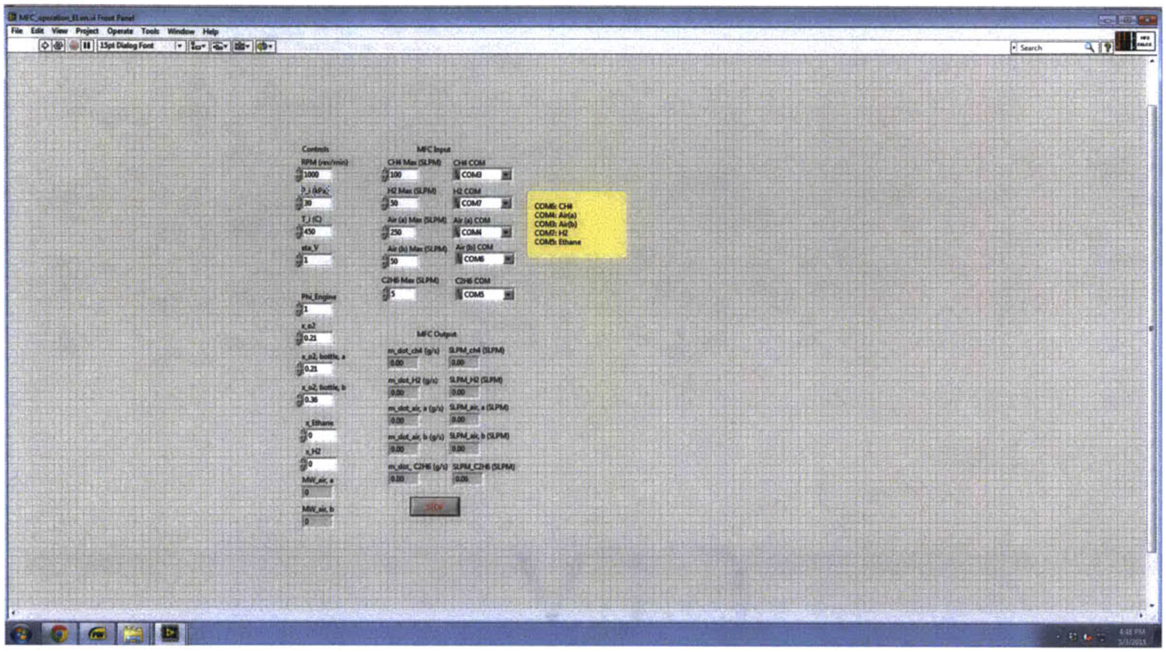

Controls

RPM (rev/min): 1000
P_i (kPa): 30
T_i (C): 450
eta_V: 1
Phi_Engine: 1
x_o2: 0.21
x_o2, bottle, a: 0.21
x_o2, bottle, b: 0.36
x_Ethane: 0
x_H2: 0
MW_air, a: 0
MW_air, b: 0

MFC Input

CH4 Max (SLPM): 100
CH4 COM: COM3
H2 Max (SLPM): 50
H2 COM: COM7
Air (a) Max (SLPM): 250
Air (a) COM: COM4
Air (b) Max (SLPM): 50
Air (b) COM: COM6
C2H6 Max (SLPM): 5
C2H6 COM: COM5

COM6: CH4
COM4: Air(a)
COM3: Air(b)
COM7: H2
COM5: Ethane

MFC Output

m_dot_ch4 (g/s): 0.00
SLPM_ch4 (SLPM): 0.00
m_dot_H2 (g/s): 0.00
SLPM_H2 (SLPM): 0.00
m_dot_air, a (g/s): 0.00
SLPM_air, a (SLPM): 0.00
m_dot_air, b (g/s): 0.00
SLPM_air, b (SLPM): 0.00
m_dot_ C2H6 (g/s): 0.00
SLPM_C2H6 (SLPM): 0.00

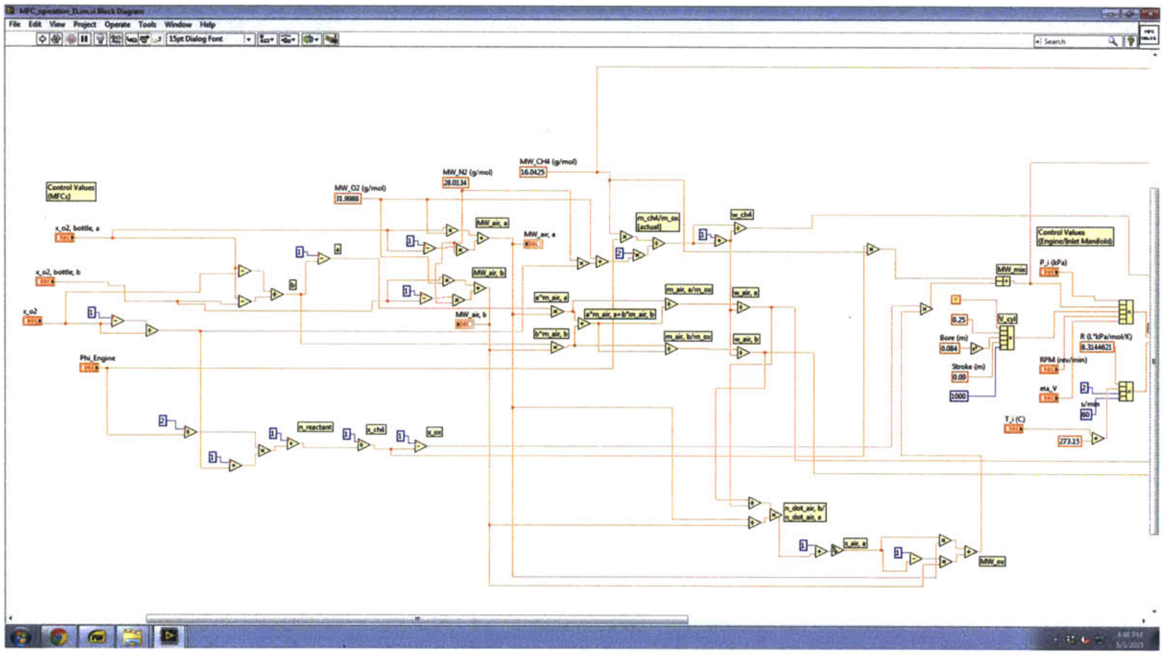

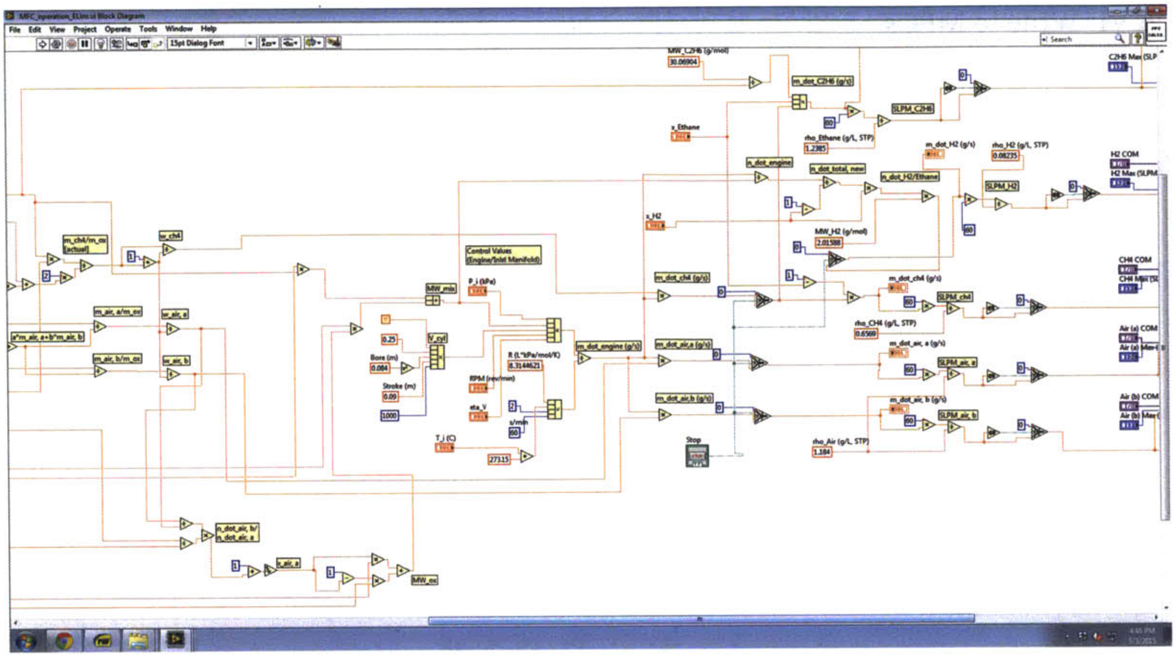
MFC_operation_ELim.vi Block Diagram
File Edit View Project Operate Tools Window Help
15pt Dialog Font
MW_C2H6 (g/mol)
30.06904
m_dot_C2H6 (g/s)
SLPM_C2H6
x_Ethane
rho_Ethane (g/L, STP)
1.2385
n_dot_engine
n_dot_total, new
n_dot_H2/Ethane
m_dot_H2 (g/s)
rho_H2 (g/L, STP)
0.08235
SLPM_H2
x_H2
MW_H2 (g/mol)
2.01588
m_ch4/m_ox (actual)
w_ch4
Control Values (Engine/Inlet Manifold)
MW_mix
P_i (kPa)
m_air, a/m_ox
w_air, a
a*m_air, a+b*m_air, b
m_air, b/m_ox
w_air, b
Bore (m)
0.084
0.25
Stroke (m)
0.09
1000
V_cyl
R (L*kPa/mol/K)
8.3144621
RPM (rev/min)
eta_V
s/min
60
T_i (C)
273.15
m_dot_engine (g/s)
m_dot_ch4 (g/s)
m_dot_air, a (g/s)
m_dot_air, b (g/s)
rho_CH4 (g/L, STP)
0.6569
SLPM_ch4
SLPM_air, a
SLPM_air, b
rho_Air (g/L, STP)
1.184
Stop
n_dot_air, b/n_dot_air, a
x_air, a
MW_ox
C2H6 Max (SLP
H2 COM
H2 Max (SLPM
CH4 COM
CH4 Max (SL
Air (a) COM
Air (a) Max
Air (b) COM
Air (b) Max
Search

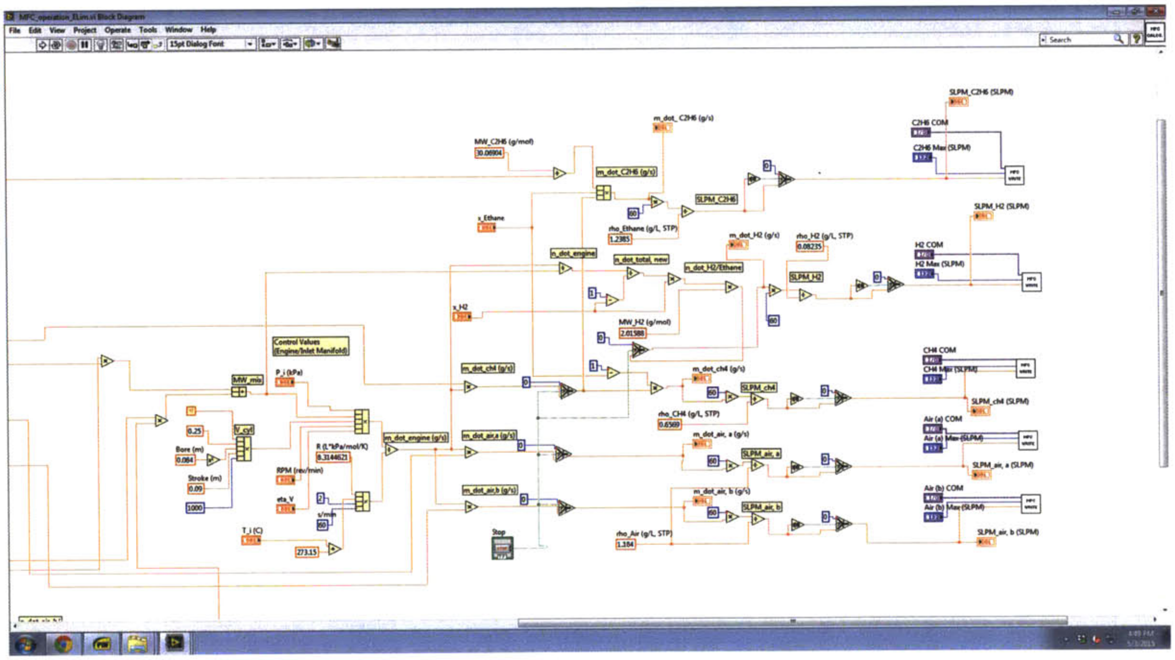
MFC_operation_ELim.vi Block Diagram
File Edit View Project Operate Tools Window Help
15pt Dialog Font
m_dot_ C2H6 (g/s)
MW_C2H6 (g/mol)
30.06904
m_dot_C2H6 (g/s)
SLPM_C2H6
x_Ethane
rho_Ethane (g/L, STP)
1.2385
SLPM_C2H6 (SLPM)
C2H6 COM
C2H6 Max (SLPM)
m_dot_H2 (g/s)
rho_H2 (g/L, STP)
0.08235
n_dot_engine
n_dot_total, new
n_dot_H2/Ethane
SLPM_H2
SLPM_H2 (SLPM)
H2 COM
H2 Max (SLPM)
x_H2
MW_H2 (g/mol)
2.01588
Control Values (Engine/Inlet Manifold)
MW_mix
P_i (kPa)
0.25
Bore (m)
0.084
Stroke (m)
0.09
1000
V_cyl
R (L*kPa/mol/K)
8.3144621
RPM (rev/min)
eta_V
s/min
60
T_i (C)
273.15
m_dot_engine (g/s)
m_dot_ch4 (g/s)
m_dot_air,a (g/s)
m_dot_air,b (g/s)
m_dot_ch4 (g/s)
rho_CH4 (g/L, STP)
0.6569
SLPM_ch4
SLPM_ch4 (SLPM)
CH4 COM
CH4 Max (SLPM)
m_dot_air, a (g/s)
SLPM_air, a
SLPM_air, a (SLPM)
Air (a) COM
Air (a) Max (SLPM)
m_dot_air, b (g/s)
SLPM_air, b
SLPM_air, b (SLPM)
Air (b) COM
Air (b) Max (SLPM)
rho_Air (g/L, STP)
1.184
Stop
n_dot_air, b/
Search

# Sub VI: Read from MFCs

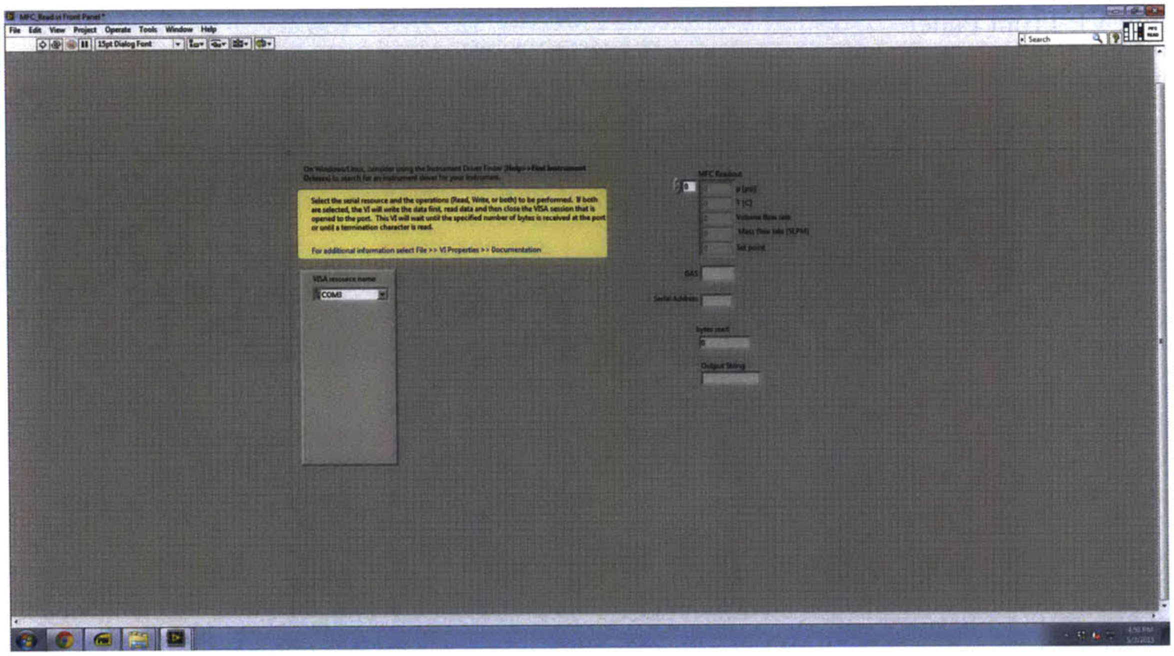

On Windows/Linux, consider using the Instrument Driver Finder (Help>>Find Instrument Drivers) to search for an instrument driver for your instrument.

Select the serial resource and the operations (Read, Write, or both) to be performed. If both are selected, the VI will write the data first, read data and then close the VISA session that is opened to the port. This VI will wait until the specified number of bytes is received at the port or until a termination character is read.

For additional information select File >> VI Properties >> Documentation

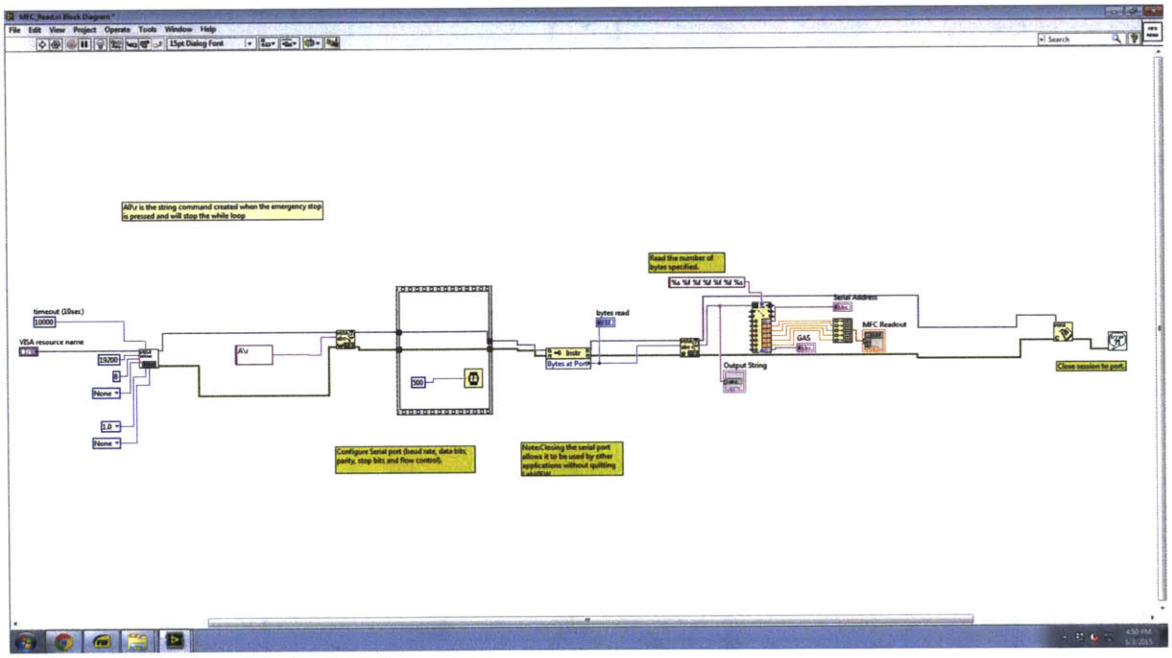

A0\r is the string command created when the emergency stop is pressed and will stop the while loop

Configure Serial port (baud rate, data bits, parity, stop bits and flow control).

Note:Closing the serial port allows it to be used by other applications without quitting LabVIEW

Read the number of bytes specified.

Close session to port.

## *Catalytic Engine*

### Main VI: Front Panel

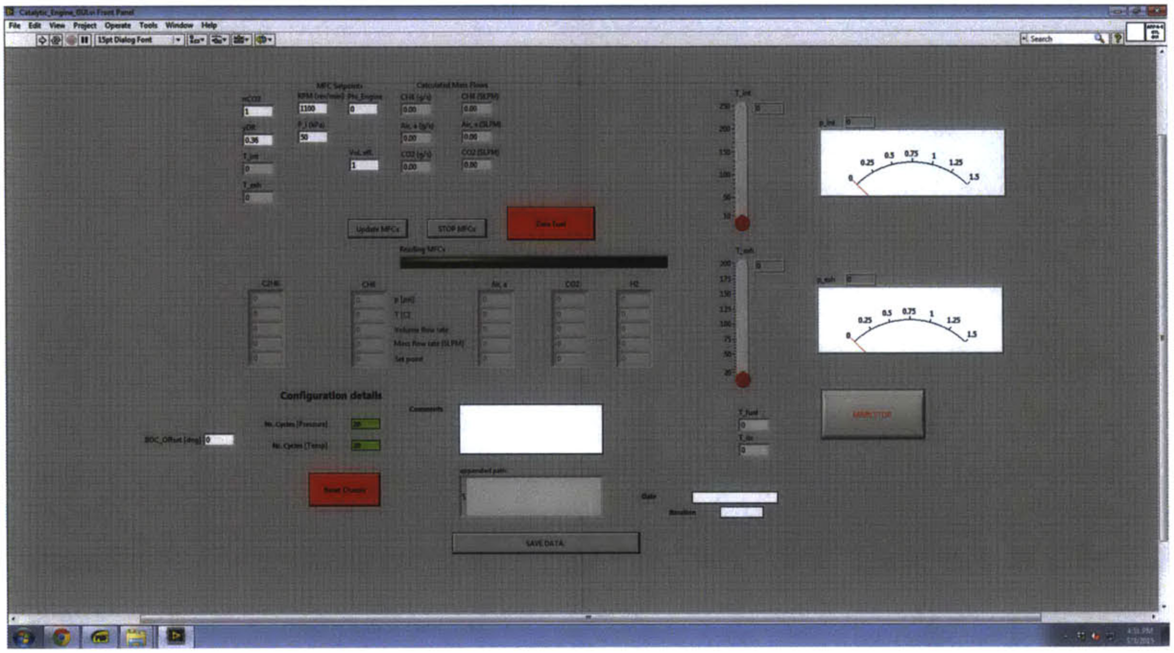

### Main VI: "Display" Data (Pressures)

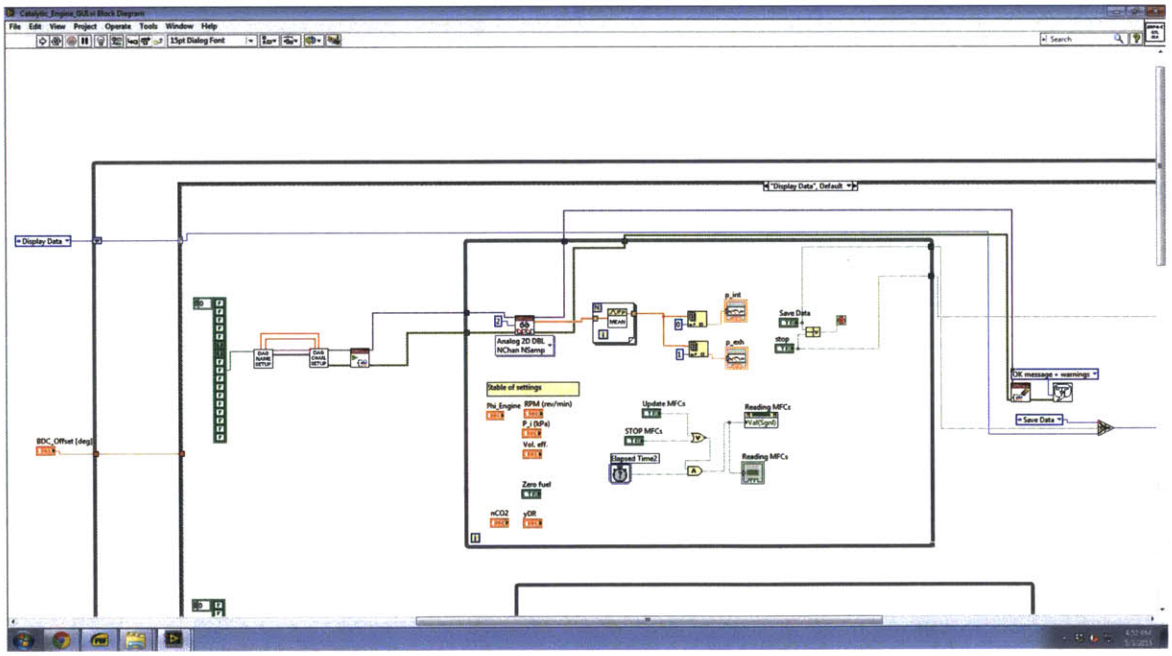

## Main VI: "Display" Data (Temperatures)

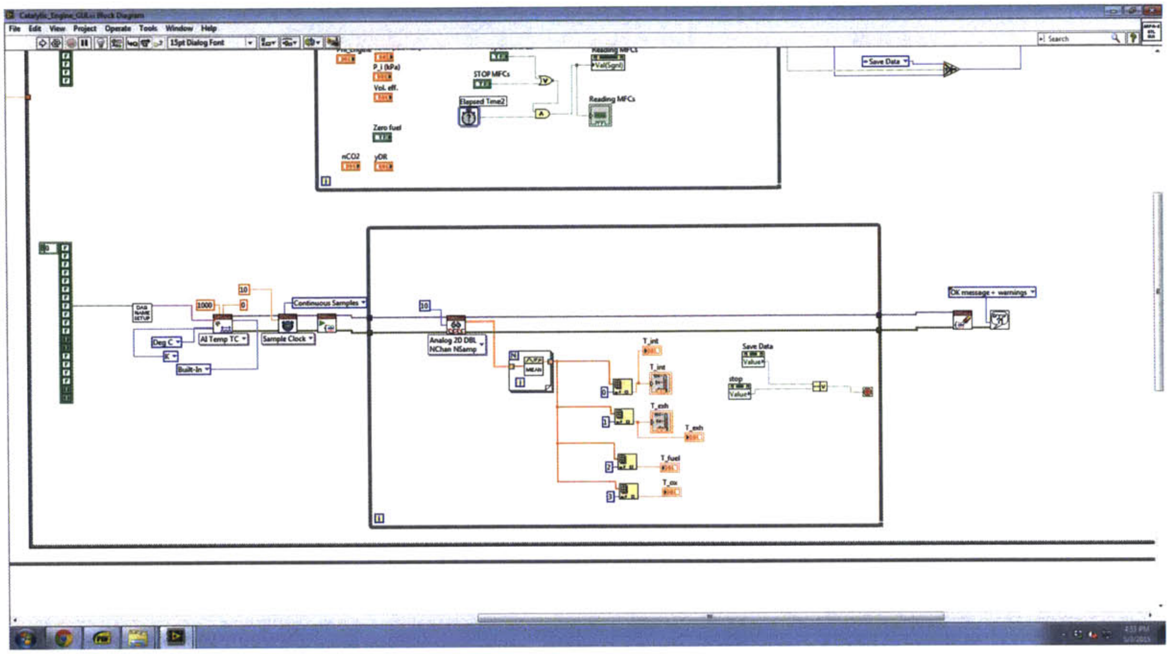

## Main VI: "Save" Data

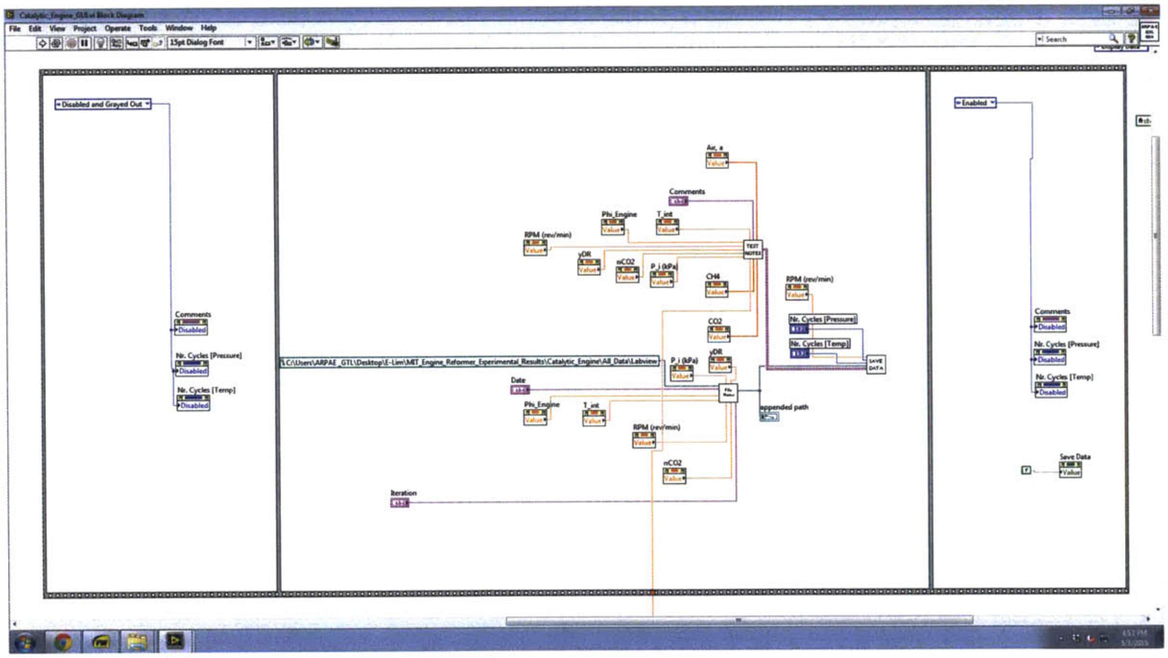

## Main VI: Write to MFCs

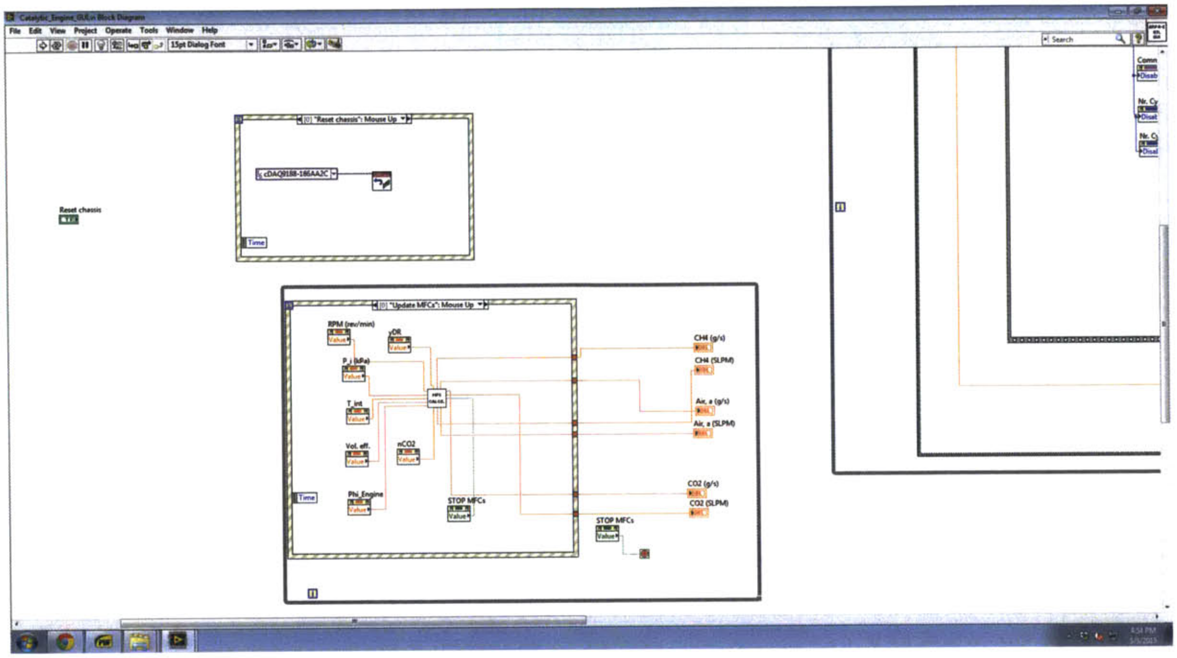

## Main VI: Read from MFCs

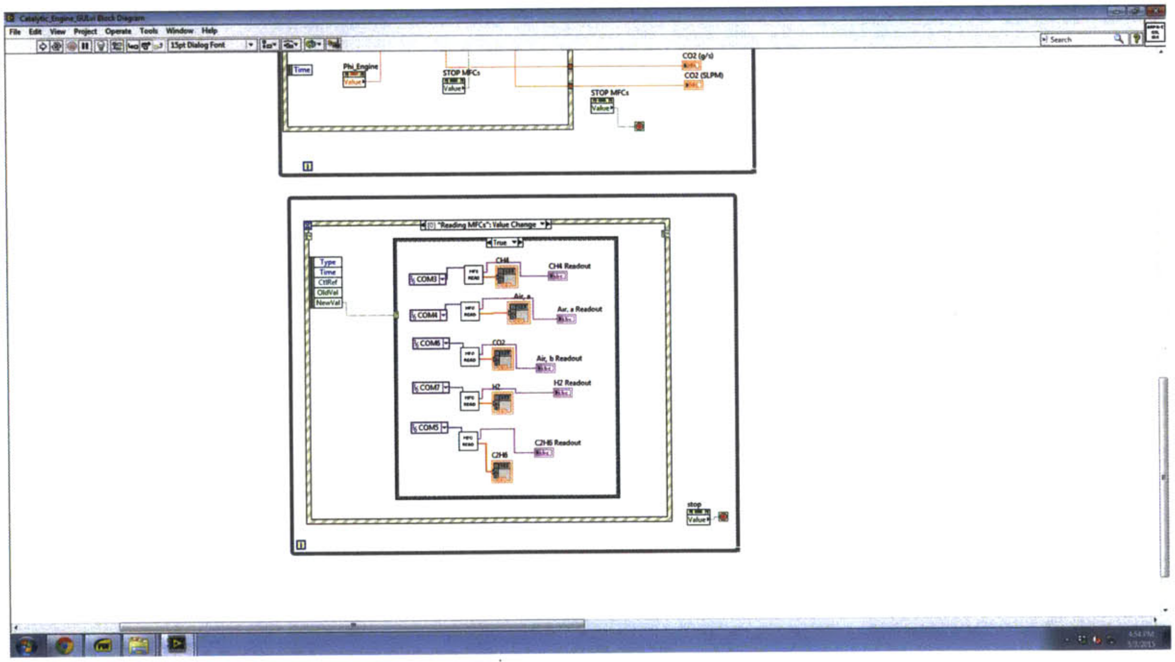

# Sub VI: Write to MFCs

Controls

RPM (rev/min): 1000

P_i (kPa): 30

T_i (C): 450

eta_V: 1

Phi_Engine: 1

y_DR: 1

n_CO2: 1

MFC Input

CH4 Max (SLPM): 100

CH4 COM: COM3

Air (a) Max (SLPM): 250

Air (a) COM: COM4

CO2 Max (SLPM): 50

CO2 COM: COM6

COM6: CH4
COM4: Air(a)
COM3: Air(b)
COM7: H2
COM5: Ethane

MFC Output

m_dot_ch4 (g/s): 0.00

SLPM_ch4 (SLPM): 0.00

m_dot_air, a (g/s): 0.00

SLPM_air, a (SLPM): 0.00

m_dot_co2 (g/s): 0.00

SLPM_co2 (SLPM): 0.00

result: 0

x/y: 0

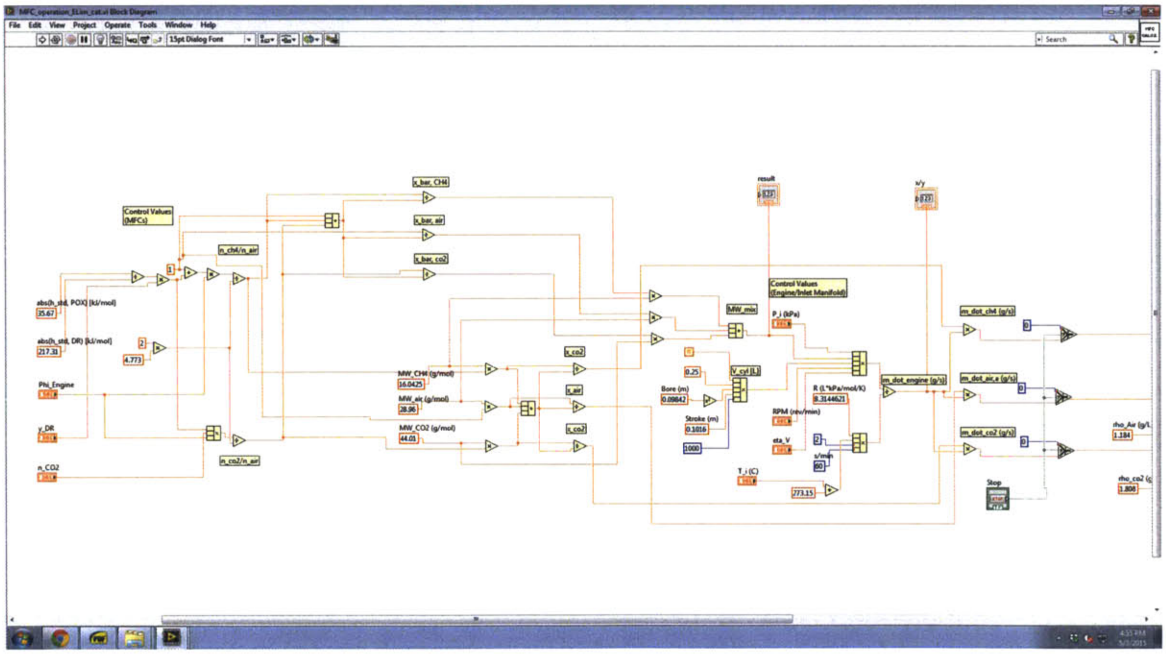

abs(h_std, POX) [kJ/mol]: 35.67

abs(h_std, DR) [kJ/mol]: 217.31

Phi_Engine

y_DR

n_CO2

MW_CH4 (g/mol): 16.0425

MW_air (g/mol): 28.96

MW_CO2 (g/mol): 44.01

Bore (m): 0.09842

Stroke (m): 0.1016

P_i (kPa)

RPM (rev/min)

eta_V

T_i (C)

R (L*kPa/mol/K): 8.3144621

rho_Air (g/L: 1.184

rho_co2 (g: 1.808

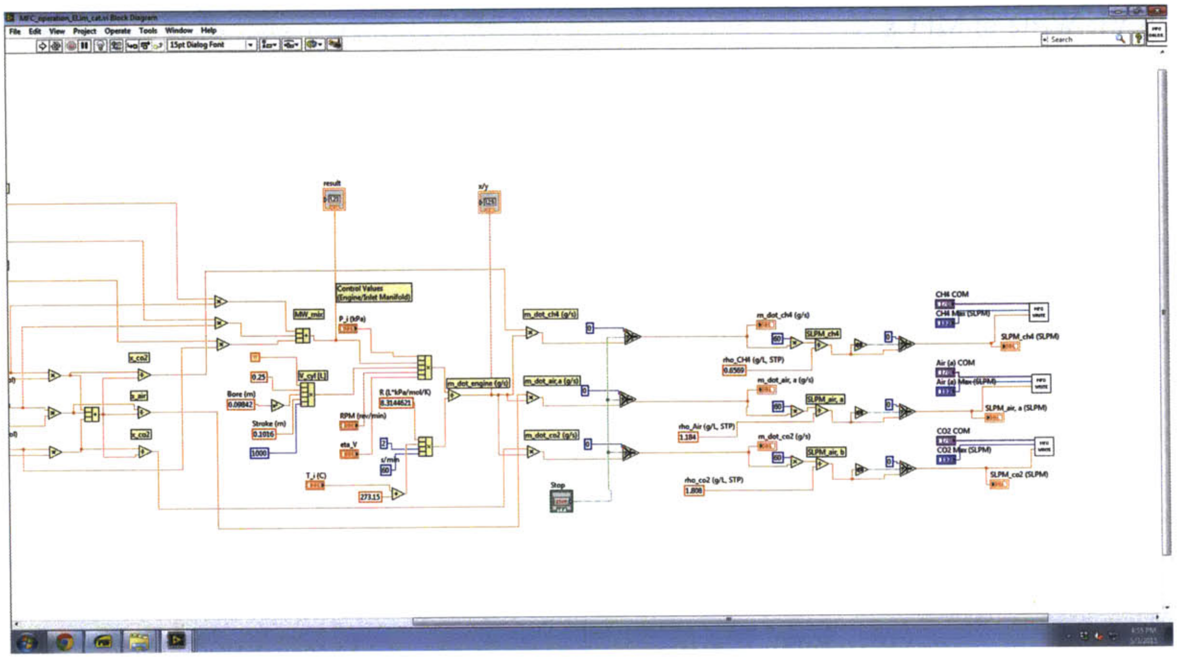
MFC_operation_El_in_cat.vi Block Diagram
File
Edit
View
Project
Operate
Tools
Window
Help
15pt Dialog Font
Search
result
x/y
Control Values
(Engine/Inlet Manifold)
MW_mix
P_i (kPa)
x_co2
x_air
x_co2
0.25
V_cyl (L)
Bore (m)
0.09842
Stroke (m)
0.1016
1000
R (L*kPa/mol/K)
8.3144621
RPM (rev/min)
eta_V
2
s/min
60
T_i (C)
273.15
m_dot_engine (g/s)
m_dot_ch4 (g/s)
m_dot_air,a (g/s)
m_dot_co2 (g/s)
0
Stop
m_dot_ch4 (g/s)
60
SLPM_ch4
rho_CH4 (g/L, STP)
0.6569
m_dot_air, a (g/s)
SLPM_air, a
rho_Air (g/L, STP)
1.184
m_dot_co2 (g/s)
SLPM_air, b
rho_co2 (g/L, STP)
1.808
CH4 COM
CH4 Max (SLPM)
SLPM_ch4 (SLPM)
Air (a) COM
Air (a) Max (SLPM)
SLPM_air, a (SLPM)
CO2 COM
CO2 Max (SLPM)
SLPM_co2 (SLPM)
MFC WRITE

## Appendix C: Data Analysis Code

The MATLAB programs that were used to analyze test data are displayed below. Programs that were similar for both engines are only displayed once, and all plotting functions are not shown for brevity.

```
function labview_plotmaker()

    clear all; close all; format short e; clc;

    % Geometric Quantities
    rc = 18.9;
    B = 0.084; % [m]
    S = 0.090; % [m]
    l = 0.135; % [m]
    Vd = (B^2)*pi*0.25*S; % [m^3]
    halfVd = Vd/2; % [m^3]
    R = 2*l/S;
    Vc = Vd/(rc-1); % [m^3]
    Vmax = Vd + Vc; % [m^3]

    samppercad = 1;
    CAD = 720;
    NumOfCycles = 200;
    RPM = 1100;

    manuscript = 'E:\Thesis\Manuscript_Plots\';

    MODE = 1;
    % 1: Processing data from Labview files. All pressure trace data is
    % plotted this way.
    % 2: Processing data and plotting from Parameters .txt files. All
    % "macro" data is plotted this way.

    switch MODE
        case 1

%              test_type = '1-Temperature';
%              test_type = '2-Edge';
%              test_type = '3-Phi';
%              test_type = '4-Spark';
%              test_type = '5-Soot';
%              test_type = '6-H2';
%              test_type = '7-Ethane';
%              test_type = '8-Knock';
%              test_type = '9-Calibrations';
%              test_type = '10-P_cyl_Compare';
            test_type = '11-New_Piston';
%              test_type = '12-Low_Temperature';

            mac_windows = 'w';

            if mac_windows == 'm'
                location = ['/Volumes/USB DISK/Thesis/Plots/' test_type
'/Labview/'];
                locationsave = ['/Volumes/USB DISK/Thesis/Plots/'
test_type '/Plots/'];
```

```
                location_matlab = '/Volumes/USB
DISK/Thesis/MATLAB_Scripts';
            elseif mac_windows == 'w'
                location = ['E:\Thesis\Plots\' test_type '\Labview\'];
                locationsave = ['E:\Thesis\Plots\' test_type
'\Plots\'];
                location_matlab = 'E:\Thesis\MATLAB_Scripts';
            else
            warning('What OS are you on?');
            end

            addpath(location); addpath(locationsave);
addpath(genpath(location_matlab));

            samples = dir(location);

            for i=1:length(samples)-2

                sample = sal_datapoint(samples(i+2,1).name);
                sample_names(i,1) = { samples(i+2,1).name };
                file(i,1) = sample_names(i,1);

                phi(i,1) = str2num([file{i,1}(4) '.' file{i,1}(6)]);
                temp(i,1) = str2num(file{i,1}(8:10));
                pres(i,1) = str2num([file{i,1}(13) '.'
file{i,1}(15:16)]);
                xh2(i,1) = str2num(file{i,1}(27:28));
                xc2h6(i,1) = str2num(file{i,1}(35:36));
                spark(i,1) = str2num(file{i,1}(42:43));
                datename(i,1) = { file{i,1}(45:53) };

                phi_orig(i,1) = phi(i,1);

                % Actual phi w.r.t. all hydrocarbons.
                if xc2h6(i,1) > 0
                    phi(i,1) = (phi(i,1)/2) * (2*(1-xc2h6(i,1)/100) +
(7/2)*(xc2h6(i,1)/100));
                end

                BDC_Offset(i,1) = {sample.notes.BDC_offset.value};
                p_int = sample.dset(1, 1).chan(1, 2).data; % [bar] CAD
intake pressure data for NumOfCycles cycles
                p_cyl = sample.dset(1, 1).chan(1, 1).data; % [bar] CAD
cylinder pressure data for NumOfCycles cycles

                p_cyl_length =max(size(p_cyl));

                CA_deg = linspace(0,719,p_cyl_length);
                CAD_ca50 = linspace(-180,539,p_cyl_length);

                CA = (CA_deg'-180)*pi/180;
                Vcyl = Vc*(1+(R+1-cos(CA)-sqrt(R^2-(sin(CA).^2)))*(rc-
1)/2); % [m^3]
                iter = Vcyl(1,1);

                for j = 1:p_cyl_length
                    dV(j,1) = Vcyl(j,1)-iter;
```

```
                    iter =Vcyl(j,1);
                end

                dV(1,1)=Vcyl(1,1)-Vcyl(end,1); % [m^3]

                BDC_Extra_Offset = 1;

                offset = round(abs(BDC_Offset{i,1} +
BDC_Extra_Offset)*p_cyl_length/720);
                MAP = [p_int((offset+1):end,:); p_int(1:offset,:)];
                p_cyl = [p_cyl((offset+1):end,:); p_cyl(1:offset,:)];
                b = samppercad*5;
                c = b*2;
                d = [MAP(end-(b-1):end,:); MAP(1:end-(b),:)];
                e = sum(d(1:c,1:end))/c;
                f = [p_cyl(end-(b-1):end,:); p_cyl(1:end-(b),:)];
                g = sum(f(1:c,1:end))/c;

                for k=1:NumOfCycles
                    pegged(:,k) = (e(1,k)+(p_cyl(1:end,k)-g(1,k)));
                    h = dV.* pegged(:,k);
                    NIMEP(k) = (sum(h)./Vd)*10^2; % [kPa]
                    GIMEP(k) =
(sum(h(1:round(p_cyl_length/2)))./Vd)*10^2; % [kPa]
                end

                Pressure(i,:,:) = pegged; % [Bar]

                Intake_Pres(i,:,:) = p_int;
                Intake_Pres_mean(i,1) = mean(p_int(:)); % [Bar]

                Exh_Pres(i,:,:) = sample.dset(1, 1).chan(1, 3).data;
                Exh_Pres_mean(i,1) = mean(sample.dset(1, 1).chan(1,
3).data(:)); % [Bar]

                Exh_Temp(i,:,:) = sample.dset(1, 3).chan(1, 2).data;
                Exh_Tempi =
reshape(Exh_Temp(i,:,:),100,NumOfCycles/10);
                Exh_Temp_mean(i,1) = mean(Exh_Tempi(:)); % [C]

                Pmaxes_mean(i,1) = mean( max(pegged) ); % [Bar]
                Pmaxes_std(i,1) = std( max(pegged) ); % [Bar]

                NIMEP_mean(i,1) = mean(NIMEP); % [kPa]

                NIMEP_std(i,1) = std(NIMEP); % [kPa]

                GIMEP_mean(i,1) = mean(GIMEP); % [kPa]

                GIMEP_std(i,1) = std(GIMEP); % [kPa]

                COV(i,1) = (NIMEP_std(i,1)/NIMEP_mean(i,1)) * 100; %
[%] for NIMEP

                Torque_Indicated_mean(i,1) =
mean(NIMEP*10^3*Vd/(4*pi)); % [N-m]
```

```
                Power_Net_mean(i,1) =
2*pi*(RPM/60)*Torque_Indicated_mean(i,1) / 10^3; % [kW]

                Power_Gross_mean(i,1) = GIMEP_mean(i,1)*Vd*(RPM/60/2);
% [kW]

                fprintf([samples(i+2,1).name '\r']);

            end

            Parameters =
table(datename,phi,phi_orig,temp,pres,xh2,xc2h6,spark,...
                BDC_Offset,...
                Intake_Pres_mean,Exh_Pres_mean,...
                Exh_Temp_mean,...
                Pmaxes_mean,Pmaxes_std,...
                NIMEP_mean,NIMEP_std,...
                GIMEP_mean,GIMEP_std,...
                COV,...
                Torque_Indicated_mean,...
                Power_Net_mean,Power_Gross_mean,...
                'RowNames',sample_names)

            % Sort by Exhaust Pressure!
            [sorted,index] =
sortrows(Parameters,{'Exh_Pres_mean'},{'ascend'});
            [a b c] = size(Pressure);
            for i = 1:a
               j = index(i);
               PressurE(i,:,:) =  Pressure(j,:,:);
            end
            sorted
            writetable(sorted,[locationsave 'Parameters_' test_type
'.txt'],'WriteRowNames', true);

plot_labview(sorted,PressurE,test_type,locationsave,NumOfCycles,manuscr
ipt);

        case 2

            yvar = {'Exh_Temp_mean', 'Pmaxes_mean', 'NIMEP_mean',
'COV'};

            savelocs = {'E:\Thesis\Plots\1-Temperature\Plots\',...
                        'E:\Thesis\Plots\3-Phi\Plots\',...
                        'E:\Thesis\Plots\4-Spark\Plots\',...
                        'E:\Thesis\Plots\6-H2\Plots\',...
                        'E:\Thesis\Plots\7-Ethane\Plots\',...
                        'E:\Thesis\Plots\Combo\',...
                        'E:\Thesis\Plots\11-New_Piston\Plots\',...
                        'E:\Thesis\Plots\12-Low_Temperature\Plots\'};
            parafiles = {'Parameters_1-Temperature.txt',...
                        'Parameters_3-Phi.txt',...
                        'Parameters_4-Spark.txt',...
                        'Parameters_6-H2.txt',...
                        'Parameters_7-Ethane.txt'...
                        'Parameters_11-New_Piston.txt',...
                        'Parameters_12-Low_Temperature.txt'};
```

```
            parameters_temp = readtable([savelocs{1} parafiles{1}]);
            parameters_phi = readtable([savelocs{2} parafiles{2}]);
            parameters_spark = readtable([savelocs{3} parafiles{3}]);
            parameters_h2 = readtable([savelocs{4} parafiles{4}]);
            parameters_c2h6 = readtable([savelocs{5} parafiles{5}]);
            parameters_newpiston = readtable([savelocs{7}
            parafiles{6}]);
            parameters_lowtemp = readtable([savelocs{8} parafiles{7}]);


plot_parameters(parameters_temp,parameters_phi,parameters_spark,paramet
ers_h2,parameters_c2h6,...

parameters_newpiston,parameters_lowtemp,yvar,savelocs,manuscript);

    end


end


function gc_plotmaker()

    clear all; close all; clc;

    MODE = 2;

    yvar = { 'H2_CO', 'H2MF', 'O2MF', 'N2MF', 'CH4MF', 'COMF', 'CO2MF',
'C2H6MF', 'CarbBal', 'CH4Conv', 'C2H6Conv', 'V_dot_ch4_std_proc' };
    manuscript = 'E:\Thesis\Manuscript_Plots\';
    N = 1100; % rev/min
    B = 0.084; S = 0.090; Vd = pi*B^2*S*1000/4; % L

    switch MODE
        case 1

%              datename = '4-22-2015';

%              test_type = '1-Temperature';
%              test_type = '3-Phi';
%              test_type = '4-Spark';
%              test_type = '6-H2';
            test_type = '7-Ethane';
%              test_type = '11-New_Piston';

            mac_windows = 'w';

            if mac_windows == 'm'
                location = ['/Volumes/USB DISK/CJCE_Paper/Plots/'
test_type '/GC/'];
                ConstantsLocation = '/Volumes/USB
DISK/CJCE_Paper/Calibration/Constants/';
                locationsave = ['/Volumes/USB DISK/CJCE_Paper/Plots/'
test_type '/Plots/'];
            elseif mac_windows == 'w'
                location = ['E:\Thesis\Plots\' test_type '\GC\'];
```

```
                ConstantsLocation = 'E:\Thesis\Calibration\Constants\';
                locationsave = ['E:\Thesis\Plots\' test_type
'\Plots\'];
            else
                warning('What OS are you on?');
            end

            addpath(location);

            filenames = dir(location);
            numFiles = length(filenames)-2;

            for i=1:numFiles

                close all;

                file{i,1}=filenames(i+2,1).name;
                phi(i,1) = str2num([file{i,1}(4) '.' file{i,1}(6)]);
                temp(i,1) = str2num(file{i,1}(8:10));
                pres(i,1) = str2num([file{i,1}(13) '.'
file{i,1}(15:16)]);
                xh2(i,1) = str2num(file{i,1}(27:28));
                xc2h6(i,1) = str2num(file{i,1}(35:36));
                spark(i,1) = str2num(file{i,1}(42:43));

                phi_orig(i,1) = phi(i,1);

                % Actual phi w.r.t. all hydrocarbons.
                if xc2h6(i,1) > 0
                   phi(i,1) = (phi(i,1)/2) * (2*(1-xc2h6(i,1)/100) +
(7/2)*(xc2h6(i,1)/100));
                end

                datename = file{i,1}(45:53);
                fprintf([file{i,1} '\r']);
                A=importdata(file{i,1},'\t',14);

                f=100;
                mult=1e-5;

                t_MS5A=0:(1/f):150;
                MS5A=mult*A.data(1:15001);

                if(min(MS5A)<-20)
                    MS5A=MS5A;
                end

                t_PPU=0:(1/f):150;
                PPU=mult*A.data(15002:end);

                if(min(PPU)<-20)
                    PPU=-PPU;
                end

                clear A;

                areasMS5A(i,1:5) = int_and_plot(t_MS5A, MS5A,'MS5A');
```

```
                areasPPU(i,1:2) = int_and_plot(t_PPU,PPU,'PPU');

                H2area(i,1) = areasMS5A(i,1);
                O2area(i,1) = areasMS5A(i,2);
                N2area(i,1) = areasMS5A(i,3);
                CH4area(i,1) = areasMS5A(i,4);
                COarea(i,1) = areasMS5A(i,5);
                CO2area(i,1) = areasPPU(i,1);
                C2H6area(i,1) = areasPPU(i,2);

                constants_table = readtable([ConstantsLocation
'Calibration_Constants_' datename '.txt']);
                H2Cal = constants_table{1,2};
                O2Cal = constants_table{2,2};
                N2Cal = constants_table{3,2};
                CH4Cal = constants_table{4,2};
                COCal = constants_table{5,2};
                CO2Cal = constants_table{6,2};
                C2H6Cal = constants_table{7,2};

                H2MF(i,1) =  H2area(i,1) * H2Cal;
                O2MF(i,1) = O2area(i,1) * O2Cal;
                N2MF(i,1) = N2area(i,1) * N2Cal;
                CH4MF(i,1) = CH4area(i,1) * CH4Cal;
                COMF(i,1) = COarea(i,1) * COCal;
                CO2MF(i,1) = CO2area(i,1) * CO2Cal;
                C2H6MF(i,1) = C2H6area(i,1) * C2H6Cal;

                CandNMFs(i,:) = [COMF(i,1)  CO2MF(i,1) CH4MF(i,1)
C2H6MF(i,1) N2MF(i,1)];
                [CarbBal(i,1) CH4Conv(i,1) C2H6Conv(i,1)] =
elemental(phi_orig(i,1),xh2(i,1)/100,xc2h6(i,1)/100,CandNMFs(i,:));

                H2_CO(i,1) = H2MF(i,1) ./ COMF(i,1);

                V_dot_ch4_std_proc(i,1) =
flows(xc2h6(i,1)/100,xh2(i,1)/100,phi_orig(i,1),...
                    N,Vd,pres(i,1),temp(i,1)+273.15,CH4Conv(i,1));

                total(i,1) =
H2MF(i,1)+O2MF(i,1)+N2MF(i,1)+CH4MF(i,1)+COMF(i,1)+CO2MF(i,1)+C2H6MF(i,
1);

            end

            gc_datapoints =
table(phi,phi_orig,temp,pres,xh2,xc2h6,spark,...
                H2MF,O2MF,N2MF,CH4MF,COMF,CO2MF,C2H6MF,...

H2_CO,total,CarbBal,CH4Conv,C2H6Conv,V_dot_ch4_std_proc,'RowNames',
file)
            writetable(gc_datapoints,[locationsave 'GC_Data_' test_type
'.txt'],'WriteRowNames', true);

        case 2

            savelocs = {'E:\Thesis\Plots\1-Temperature\Plots\',...
                        'E:\Thesis\Plots\3-Phi\Plots\',...
```

```
                        'E:\Thesis\Plots\4-Spark\Plots\',...
                        'E:\Thesis\Plots\6-H2\Plots\',...
                        'E:\Thesis\Plots\7-Ethane\Plots\',...
                        'E:\Thesis\Plots\11-New_Piston\Plots\'};
            parafiles = {'GC_Data_1-Temperature.txt',...
                        'GC_Data_3-Phi.txt',...
                        'GC_Data_4-Spark.txt',...
                        'GC_Data_6-H2.txt',...
                        'GC_Data_7-Ethane.txt',...
                        'GC_Data_Atmospheric_Exhaust_11-
New_Piston.txt',...
                        'GC_Data_High_Exhaust_11-New_Piston.txt'};

            parameters_temp = readtable([savelocs{1} parafiles{1}]);
            parameters_phi = readtable([savelocs{2} parafiles{2}]);
            parameters_spark = readtable([savelocs{3} parafiles{3}]);
            parameters_h2 = readtable([savelocs{4} parafiles{4}]);
            parameters_c2h6 = readtable([savelocs{5} parafiles{5}]);
            parameters_newpiston_atm = readtable([savelocs{6}
parafiles{6}]);
            parameters_newpiston_high = readtable([savelocs{6}
parafiles{7}]);

            plot_gc(parameters_temp,parameters_phi,parameters_spark,...

parameters_h2,parameters_c2h6,parameters_newpiston_atm,...
                parameters_newpiston_high,yvar,savelocs,manuscript);

    end



end


function areas=int_and_plot(XDATA,YDATA,NAME)

    column = NAME;

    switch column
        case 'MS5A'
            bounds = {'avg' 140 145; 'H2' 24 30; 'O2' 34 40; 'N2' 50
60; 'CH4' 67 86; 'CO' 116 140};
        case 'PPU'
            bounds = {'avg' 140 145; 'CO2' 56 66; 'C2H6' 70 84};
    end

    plot_it(XDATA,YDATA,NAME,[]);

    [n_peaks,cols] = size(bounds);
    n_peaks = n_peaks-1;

    BL_st=find(XDATA>bounds{1,2},1,'first');
    BL_end=find(XDATA>bounds{1,3},1,'first');
    BL=mean(YDATA(BL_st:BL_end));

    areas=zeros(1,n_peaks);
```

```
    for i=1:n_peaks;

        i_st=find(XDATA>bounds{i+1,2},1,'first');
        i_end=find(XDATA>bounds{i+1,3},1,'first');

        y_bound = max(YDATA)-min(YDATA);
        factor=0.1;

        axis_bounds = [XDATA(i_st)-2 XDATA(i_end)+2 BL-factor*y_bound
BL+factor*y_bound];
        axis(axis_bounds);

        areas(1,i) = fill_it(XDATA,YDATA,i_st,i_end,BL);

    end

    close all;

end

function h = plot_it(x,y,column,axis_bound)

    figure();
    plot(x,y);
    xlabel('time [s]');
    ylabel('sensor output [mV]');
    title(column)
    hold on;

    axis(axis_bound);

end

function area = fill_it(x,y,ist,iend,base)

    x1=x(ist:iend);
    x2=x1;
    y1=y(ist:iend);
    y2=base+0*y1;

    X = [x1 fliplr(x2)];
    Y = [y1;fliplr(y2)];
    fill(X,Y,'r');
    area = trapz(x(ist:iend),y(ist:iend)-base);

end

function [CARBBAL CH4CONV C2H6CONV] = elemental(PHI, XH2, XC2H6,
EXHCOMPO)

    COMF_EXH = EXHCOMPO(1);
    CO2MF_EXH = EXHCOMPO(2);
    CH4MF_EXH = EXHCOMPO(3);
    C2H6MF_EXH = EXHCOMPO(4);
    N2MF_EXH = EXHCOMPO(5);
```

```
    DENOM = (1 + (2/PHI)*(4.773)) * (1 + XH2/(1-XH2));

    CH4MF_IN = (1-XC2H6)/DENOM;
    N2MF_IN = (2*3.773/PHI)/DENOM;
    C2H6MF_IN = XC2H6/DENOM;

    CARBBAL = ((2*C2H6MF_EXH + COMF_EXH + CO2MF_EXH +
CH4MF_EXH)*(N2MF_IN)) / ((CH4MF_IN + 2*C2H6MF_IN)*(N2MF_EXH));
    CH4CONV = 1 - ((CH4MF_EXH)/(CH4MF_IN)) * ((N2MF_IN)/(N2MF_EXH));
    C2H6CONV = 1 - ((C2H6MF_EXH)/(C2H6MF_IN)) * ((N2MF_IN)/(N2MF_EXH));

end


function [CARBBAL CH4CONV CO2_EXHVINT N2MF_IN CH4MF_IN] =
elemental(PHI, yDR, aCO2, EXHCOMPO)

    h_abs_std_POX = 35.56;
    h_abs_std_DR = 247.31;

    CH4MF_EXH = EXHCOMPO(1);
    COMF_EXH = EXHCOMPO(2);
    CO2MF_EXH = EXHCOMPO(3);
    N2MF_EXH = EXHCOMPO(4);

    DENOM = 1 + (2/PHI)*(4.773) + yDR*(h_abs_std_POX/h_abs_std_DR)*(1 +
aCO2);

    CH4MF_IN = (1+yDR*(h_abs_std_POX/h_abs_std_DR))/DENOM;
    CO2MF_IN = (yDR*(h_abs_std_POX/h_abs_std_DR)*(aCO2))/DENOM;
    N2MF_IN = ((2/PHI)*(3.773))/DENOM;

    CARBBAL = ((COMF_EXH + CO2MF_EXH + CH4MF_EXH)*(N2MF_IN)) /
((CH4MF_IN + CO2MF_IN)*(N2MF_EXH));
    CH4CONV = 1 - ((CH4MF_EXH)/(CH4MF_IN)) * ((N2MF_IN)/(N2MF_EXH));
    CO2_EXHVINT = ((CO2MF_EXH)/(CO2MF_IN)) * ((N2MF_IN)/(N2MF_EXH));

end


function V_dot_ch4_std_proc =
flows(x_c2h6,x_h2,phi,N,Vd,p_i,T_i,eta_ch4)

    T_std = 298.15; % K
    p_std = 1.01325; % bar

    V_dot_ch4_std = ( N .* Vd .* T_std .* p_i .* (1-x_c2h6) * 0.0353 *
60 ) ./ ...
        ( 2 .* T_i .* p_std .* (1+2.*4.773./phi) .* (1+x_h2./(1-x_h2))
); % scfh

    V_dot_ch4_std_proc = V_dot_ch4_std .* eta_ch4;

end
```

```
function
[n_dry_N,n_dry_error,c_error,o_error,h_error,n_error,h2o_ratio,a_h2o_me
an,a_h2o_error,co2_production_frac,X_o2] =
catal_stoich(phi,y_dr,a_co2,mfs)

    h_abs_std_POX = 35.56;
    h_abs_std_DR = 247.31;
    H = h_abs_std_POX/h_abs_std_DR;

    % Standard enthalpies of formation (kJ/mol, or MJ/kmol)
    h_std_co2 = -393.52;
    h_std_h2og = -241.83;
    h_std_co = -110.54;
    h_std_ch4 = -74.87;
    h_std_c2h6 = -83.7;

    h2mf = mfs(1);
    o2mf = mfs(2);
    n2mf = mfs(3);
    ch4mf = mfs(4);
    comf = mfs(5);
    co2mf = mfs(6);
    c2h6mf = mfs(7);

    % All molar expressions are relative.
    denom = 1 + (2/phi)*(4.773) + y_dr*(H)*(1 + a_co2);
    n2in = ((2/phi)*3.773)/denom;
    ch4in = (1+y_dr*H)/denom;
    co2in = (y_dr*H*a_co2)/denom;
    o2in = (2/phi)/denom;
    c_in = 1+y_dr*H*(1+a_co2);
    o_in = (2/phi)*2+y_dr*H*2*a_co2;
    h_in = 4+y_dr*H*4;
    n_in = (2/phi)*2*3.773;

    X_o2 = 1-(o2mf/o2in)*(n2in/n2mf);

    n_dry_C = c_in/(ch4mf+co2mf+comf+2*c2h6mf);
    n_dry_N = n_in/(2*n2mf);

    n_dry_error = abs(n_dry_C-n_dry_N)/n_dry_N;

    c_out = n_dry_N*(ch4mf+co2mf+comf+2*c2h6mf);
    o_out_dry = n_dry_N*(2*co2mf+comf+2*o2mf);
    h_out_dry = n_dry_N*(4*ch4mf+2*h2mf+6*c2h6mf);
    n_out = n_dry_N*(2*n2mf);

    H_h2o = h_in - h_out_dry;
    O_h2o = o_in - o_out_dry;
    H_extra = (H_h2o - 2*O_h2o)/2;
    H_mf_new = (n_dry_N*h2mf + H_extra)/(n_dry_N+H_extra);

    h2o_ratio = H_h2o/O_h2o;

    c_error = abs(c_in-c_out)/c_out;
    o_error = abs(o_in-(o_out_dry+O_h2o))/(o_out_dry+O_h2o);
    h_error = abs(h_in-(h_out_dry+H_h2o))/(h_out_dry+H_h2o);
    n_error = abs(n_in-n_out)/n_out;
```

```
    a_h2o_H = 0.5*H_h2o;
    a_h2o_O = O_h2o;

    a_h2o_mean = mean([a_h2o_H a_h2o_O]);
    a_h2o_error = abs(a_h2o_H-a_h2o_O)/a_h2o_O;

    co2_production_frac = (co2mf/n2mf-co2in/n2in)/(ch4in/n2in-
(ch4mf+comf)/n2mf);

end
```